Infrared Antennas and Resonant Structures

Infrared Antennas and Resonant Structures

Javier Alda and **Glenn Boreman**

SPIE PRESS
Bellingham, Washington USA

Library of Congress Cataloging-in-Publication Data

Names: Alda, Javier, 1962- author. | Boreman, G. D. (Glenn D.), author.
Title: Infrared antennas and resonant structures / Javier Alda and Glenn Boreman.
Description: Bellingham, Washington, USA : SPIE Press, [2017] | Includes bibliographical references and index.
Identifiers: LCCN 2017025139 | ISBN 9781510613584 (softcover ; alk. paper) | ISBN 1510613587 (softcover ; alk. paper) | ISBN 9781510613591 (PDF) | ISBN 1510613595 (PDF) | ISBN 9781510613607 (ePub) | ISBN 1510613609 (ePub) | ISBN 9781510613614 (Kindle/Mobi) | ISBN 1510613617 (Kindle/Mobi)
Subjects: LCSH: Optical antennas. | Infrared detectors. | Electromagnetism.
Classification: LCC TK8360.O65 A43 2017 | DDC 621.36/2–dc23 LC record available at https://lccn.loc.gov/2017025139

Published by

SPIE
P.O. Box 10
Bellingham, Washington 98227-0010 USA
Phone: +1 360.676.3290
Fax: +1 360.647.1445
Email: books@spie.org
Web: http://spie.org

Printed in the United States of America.
First Printing.
For updates to this book, visit http://spie.org and type “PM281” in the search field.

Contents

Preface

It was May 1996 when we were walking in Alcobendas, Madrid, to find a place to enjoy a coffee. Once we got updated on personal matters, we were ready to jump into the scientific and technical issues that always light a spark with us. The topic that day was the capability of very tiny pieces of metal, deposited on a dielectric substrate, to resonate at optical frequency in the manner of the old-fashioned antenna. A research stay at the ETHZ in Switzerland showed that, besides the exotic application of optical frequency multiplication for time standard measurements, antennas could move upward in the frequency domain and get into the optical regime with awesome capabilities yet to be explored.

This was probably the first conversation on optical antennas that we had. Since that walk, significant advances have been made in this field, and in some of them, the efforts made at the Infrared System Lab of CREOL (University of Central Florida), at the Applied Optics Complutense Group (Universidad Complutense de Madrid), and at the Physics and Optical Science Department (University of North Carolina at Charlotte) have contributed to a better understanding and application of this area.

Optical antennas, infrared antennas, antenna-coupled detectors, plasmonic antennas, nano-antennas, resonant optics, meta-surfaces... are all different names representing the same idea: how the electromagnetic interaction of light and a wise combination of material and geometry may provide new elements and devices that did not previously exist. However, naming the devices we were studying was not our main concern, nor was the visibility of our findings. The Infrared System lab has been primarily devoted to complying with the sponsors' requirements and supporting the students graduating from the lab. These 20 years of activity in this field have been mainly focused on the practical application of antenna-coupled devices and resonant structures.

At times we have been tempted to present this topic as a mere translation of the radiofrequency and microwave antenna principles to optical frequencies. Although optical antennas inherited some basic ideas from their lower-frequency counterparts, there are couple of very substantial differences. First of all, materials, especially metals, that behave as ideal conductors in the radiofrequency regime become dispersive at optical frequency. Charge carriers

are not able to follow the incident electric field, and new phenomena, sometimes degrading device performance, are at play. Secondly, the size of the elements able to resonate at optical bands is in the range of tens and hundreds of nanometers. We are then in the nanoworld with all that goes with it. Meso-optics and nano-photonics are the two areas that aid in understanding this technology, where the systems are moving closer and closer to the quantum realm. Besides, fabrication technologies in the nanoscale are complex, hard to master, and extremely expensive. Therefore, computational electromagnetism plays a decisive role in sorting out the best possible design that finally goes to the nanofabrication lab. These labs mainly involve electron-beam lithography, focused ion beam, and all of the auxiliary techniques for the precise deposition of materials. These techniques, although well established and capable, produce geometries departing from the specification to some extent, with the result of a loss of performance. The fabricated devices are tested using dedicated characterization setups, and the measured discrepancies require further refinement of the models and simulations.

The purpose of this book is to document the advances in technology achieved by our research groups over the period of approximately 1995–2016 in the area of infrared antennas and frequency-selective surfaces. Our approach was primarily experimental and consisted of three main thrusts: design, fabrication, and testing. The goal was always to have operational devices to measure, and the comparison between the designed-for and measured performance "closed the loop," giving additional insight and guidance for device optimization. This volume summarizes a large part of our activity in antenna-coupled detectors, optical antennas, and resonant structures, including frequency-selective surfaces, resonant polarization elements, and reflectarrays. Our main goal is to show the reader the practical issues related to the design, modeling, fabrication, and testing of these devices.

Our over-riding principle was to implement and demonstrate radio-frequency technology at infrared frequencies, using electron-beam lithography. Translation of longer-wavelength designs to infrared by wavelength-ratio scaling of dimensions provides a starting point, but modifications are needed because of the non-ideal properties of the metals in the infrared, and because of the effect of the substrate refractive index.

The two main types of devices were antenna-coupled sensors that had an electrical connection for signal readout, and frequency-selective surfaces that were purely passive devices without electrical connection. Owing to the practical difficulties of establishing connections between the antenna structure and the sensor, the passive devices were always easier to work with. We did not pursue antenna-coupled emitters, so antenna-coupled devices were always seen from a sensor perspective. We were not typically concerned with field enhancement for its own sake, but rather for the response of the sensor.

The authors want to recognize those persons who over the years have contributed to making possible the type of applied research that is described here: Mohamed Abdel-Rahman, Jeffrey Bean, Christos Christodoulou, Iulian Codreanu, Kevin Coffey, Alexander Cuadrado, Jeffrey D'Archangel, Aristide Dogariu, Mahmoud Elshorbagy, José Miguel Ezquerro, Louis Florence, William Folks, Bill Franklin, Chi Fu, Christophe Fumeaux, James Ginn, José Antonio Gómez-Pedrero, Francisco Javier González, Michael Gritz, Robert Hudgins, Edward Kinzel, Fritz Kneubühl, Dale Kotter, Peter Krenz, Brian Lail, Nuria Llombart, José Manuel López-Alonso, Donald Malocha, Tasneem Mandviwala, Juan Carlos Martínez-Antón, Christopher Middlebrook, Charles Middleton, Brian Monacelli, Camilo Moreno, Daniel Mullaly, Ben Munk, Robert Olmon, Robert Peale, Wolfgang Porod, James Potter, Menelaos Poutous, Irina Puscasu, Markus Raschke, José María Rico-García, Jason Schaefer, William Schaich, David Shelton, Manuel Silva-López, Brian Slovick, Jeff Tharp, Eric Tucker, Sam Walsworth, Arthur Weeks, Scott Williams, and Guy Zummo.

Finally, it is joy to also recognize the unconditional support and encouragement that we have received at home from Paz, Irene, Maggie, and Eddie. Their contributions to the work presented here were indispensable.

Javier Alda
Glenn Boreman
July 2017

Chapter 1
Introduction

When dealing with light and optics, it is commonplace to constrain our understanding to the visible range of the electromagnetic spectrum, i.e., the narrow interval where the human eye is able to respond. However, this anthropomorphic definition of optics is too narrow. On both sides of the visible spectrum, we find spectral ranges full of interest that also allow an analysis quite similar to that given in the visible spectrum. In the high-energy, high-frequency side, we find that ultraviolet radiation, X-rays, and γ-rays are of use in astronomy, medicine, and technology because of their capability to trigger chemical reactions and generate ionized matter. On the low-frequency, low-energy side, we have witnessed the development of radiofrequency applications in telecom, radar, and microwaves. But, when reaching those portions of the spectrum closer to the visible, the use of millimeter waves, terahertz, and infrared radiation has produced a variety of devices and technologies that have strongly expanded the capabilities to sense nature in a different way. In the infrared, image-forming systems have advanced in accuracy, time response, and analysis capabilities through improved algorithms and by using hyperspectral techniques and sensor fusion. Beyond thermography, infrared image technology already distinguishes chemical compounds, and takes full advantage of the detection of the polarization of light.

Optical antennas, infrared antennas, antenna-coupled devices, rectennas, plasmonic antennas, nano-antennas, resonant elements, frequency-selective surfaces, metasurfaces, metamaterials, etc. — all of these names have been used over the last decades to refer to the analysis and study of the interaction of light, or more generally, electromagnetic radiation, with metallic and dielectric structures having dimensions below, or well below, the wavelength of operation [Fumeaux *et al.*, 1998] [Crozier *et al.*, 2003] [Maier *et al.*, 2003] [Alda *et al.*, 2005] [Muhlschelegel *et al.*, 2005] [Alda *et al.*, 2006b] [Engheta, 2007] [Boreman, 2008] [Bharadwaj *et al.*, 2009] [Novotny & van Hulst, 2011] [Knight *et al.*, 2011] [Berkovitch *et al.*, 2012] [Novotny & Hecht, 2012] [Alù & Engheta, 2013] [Agio & Alù, 2013] [Abadal *et al.*, 2013] [Moddel & Grover, 2013] [Yu & Capasso, 2014] [Zhao *et al.*, 2014] [Chen *et al.*, 2016]. These

different names and publications refer to different applications requiring auxiliary elements and subsystems, but all of them share the same foundations when describing their interaction with light. As a matter of fact, this area started drawing increased interest when the possibility of manipulating radiation at the nanoscale was demonstrated using antenna devices. The new elements were usually the natural and miniaturized counterparts of designs that were already proven at radiofrequencies and in the microwave range. However, as the knowledge and understanding of the basic mechanism at work in the optical range improved, the design of new applications ensued, and elements and applications that were optical in nature were proposed.

In this book we have summarized more than two decades of research in this aspect of nanophotonics, even though at the time of our entering in this field, nanophotonics was not fully defined and was lacking some of the elements that now are clearly established. The primary reason to move into the optical antenna arena was the expectation to develop a new kind of detector in the infrared that could improve on the limited technologies that were available back in the 1990s. Thus, we were able to witness and participate in this quest from its inception.

In order to better organize the material in this book, we have divided our analysis into two main types of devices. The first type, which we call infrared or optical antennas, corresponds to those elements that provide an electric signal that is read by external electronics. These devices can be seen as antenna-coupled devices, and besides the resonant elements necessary to collect electromagnetic radiation, they also contain a transducer element that generates a current, a voltage, or a change in some characteristics in the electric circuit that is external to the infrared antenna device. The second type of device, which we call resonant structures, includes those elements that modify some parameters of the incoming radiation: phase, spectral distribution, polarization state, etc. These changes can be observed in the transmitted or reflected radiation. These elements can be considered as passive because they do not provide an electric signal and are not coupled to transducers. However, in some applications involving phase transitions in the subsystems of the devices, some signal inducing those phase transitions can be used.

The benefit of the antenna-coupling structure is its spatially compact sensor and a large collection area [Boreman, 1996]. It should be noted that, in the quest for ever-smaller pixel sizes, antenna-coupled sensors provide a platform for denser focal plane arrays as compared to immersion-lens-coupled sensors, which are constrained by the diffraction limit of the radiation impinging on the structure. For a nominally half-wave antenna, the pixel dimension can be distinctly sub-wavelength in spatial dimension. This makes optical antennas the smallest possible detector, being a small fraction of the detected wavelength [Tang *et al.*, 2008]. The main idea from a signal-to-noise ratio perspective is that smaller sensors generate less noise than do larger

sensors. Using antenna coupling disconnects the usual dependence of sensor area and collection area. The normal assumption is that noise-equivalent power (NEP) is proportional to the square root of the sensor area. The definition of specific detectivity, $D^* = \frac{\sqrt{A}\sqrt{\Delta f}}{\mathrm{NEP}}$, is such that if NEP is held to a smaller value by a small sensor area, D^* can be referenced to a larger collection (pixel) area, potentially yielding an increased D^*. Over time, we have seen that some of the expectations in terms of performance of optical antennas have not yet been fully realized, but, at the same time, new designs in geometry and material combinations have made possible some other advances. The tiny dimensions of an optical antenna reduces its capability to collect large amounts of energy. Furthermore, impedance mismatches — between free-space, the antenna, and the load in charge of transferring the signal and power to the external circuit — also limit the performance of these devices. One might wonder how an element made of metal, that in its macroscopic form reflects a very large portion of the electromagnetic radiation in the visible and the infrared (the reflectance values are usually well above 90%), can be tailored to couple the incoming energy towards a load. The solution for this issue is not easy and, as we will see, requires a good understanding of the material characteristics and how they can work to improve efficiency and provide useful devices.

Additionally in the infrared (IR), antenna coupling provides an inherent control of spectral response, polarization response, and angular response that is not directly available in classical IR sensors [Schaefer, 1999]. The time response of infrared antennas is limited by the transduction mechanism. When rectification is used, the response is in the range of femtoseconds, allowing a very fast response. The fabrication of optical antennas allows integration with other auxiliary elements of conventional optical systems, diffractive optics, waveguides, and control and acquisition electronics. Additionally, some infrared-antenna-coupled sensors can work at room temperature without the need of sophisticated cooling subsystems that are required in some infrared detection technologies. Beyond the still-to-be-realized gains in responsivity and detectivity, infrared antennas are desirable in some specific applications where their selective capabilities, small footprint, and room-temperature operation are of importance in imaging applications [González *et al.*, 2006] [González *et al.*, 2005].

Since long ago, optical instrumentation has been based on the use of lenses and mirrors. When diffractive elements became available, optical design could merge them with classical refracting or reflecting optics. This fact opened the way to diffractive optics that incorporate Fresnel zone plates, holographic optical elements, etc. When considering the interaction of light with sub-wavelength resonant structures, it is also possible to modify the spectral content (frequency-selective surfaces), the polarization state (polarizers and

retarders), as well as the phase front of light beams (reflectarrays). These resonant structures take full advantage of electromagnetism; because their mechanism is based on electromagnetic resonances at optical frequencies, they can be considered as new additions to the optical tool kit in the form of devices that can be grouped under the category of resonant optics. Another field of application of resonant structures controls and tailors the near field around them [Crozier *et al.*, 2003]. In this case, the strong field-enhancement near these devices can be used to boost the emission from a diode laser [Cubukcu *et al.*, 2006], or trigger a spectral response (Raman spectroscopy, fluorescence, etc.) that lowers the limit of detection in some cases [Izquierdo-Lorenzo *et al.*, 2012]. Also, these capabilities can be used to generate optical trapping and confinement.

As shown in this book, the analysis of infrared antennas and resonant structures combines an understanding of the basic interaction between light and matter with the capability to generate devices and elements to detect and control optical radiation in the infrared. Therefore, we are delighted to show how the research in this area is full of challenges and rewards for everyone entering or working in the field.

1.1 Historical Background

Since ancient times, the word "antenna" has been related to the protuberances that insects have developed to sense their surroundings using mechanical, thermal, and olfactory terminations. The first appearance of this term defining these apparatus was perhaps given as a translation of Aristotle from the word "keraiai" into the Latin "antenna" by Theodorus Gaza in 1476 [Aristotle, 4th century BC]. When electromagnetism began its journey in modern science and technology, Hertz demonstrated the emission and reception of electromagnetic waves through air using a spark generator and a metal ring that acted as emitter and detector antennas. This happened in 1887, and in 1895 Marconi rediscovered the findings of Hertz and began to use the word antenna to refer to the metallic structures used to generate and receive electromagnetic waves, which we now know as radio waves. Since then, electromagnetism and electronics have adopted the term antenna for the part of a circuit that interfaces between the freely propagating wavefront that moves through the space and the electronic circuit that performs the generation or detection functions.

Antenna theory has become one of the most interesting parts of electromagnetism because it has combined geometries that are able to harness charge carrier oscillations to produce the desired patterns of radiating fields in a variety of angular, spectral, and polarization combinations. The quest for higher frequencies in the emission and reception of electromagnetic waves has been boosted by bandwidth hunger and by the need to sense objects and

elements beyond the visible range. Telecommunication and radar have provided solutions that have become more optical as they have approached and surpassed the terahertz band. Nowadays antennas are pervasive and ubiquitous in daily-use technologies. From the most common case of radio stations to the implementation of radiofrequency identification (RFID) tags in products, credit cards, and documents, antennas are part of the technology that we use every day. As a very common example, any current smartphone contains a plethora of antennas specialized for dedicated tasks and bands: Wi-Fi, GPS, near-field communication, radio stations, and of course telecom bands (3G, 4G and beyond). An adequate design of these antennas is key to improving performance, avoiding mutual interference between bands, and obtaining a longer battery life. These designs are much more sophisticated than the simple dipole antennas used in the first radio stations at the end of 19^{th} century, and they are flat and printed on flexible substrates. At the same time, microwave, millimeter band, and terahertz devices have demonstrated a very good adaptation to the new requirements of modern security, surveillance, and remote sensing applications.

These advances in antenna design and understanding have been made during the 20^{th} century when electronics have been driving most of the cutting-edge advances in technology. In the last quarter of the previous century, we saw how new fabrication tools opened the way to the manufacturing of tiny structures already in the nanoscale. Then, the unstoppable push towards higher and higher frequencies in antenna design reached the optical domain, first in the infrared and finally in the visible range. When this happened about 30 years ago, it was common for optical antennas to be considered as any element able to capture optical radiation, and by extension to radioelectric astronomy, an optical telescope was also considered as an optical antenna. However, actual optical antennas, seen as the natural extension of their lower-frequency counterparts, were already on the scene for some exotic applications and ideas. It is interesting to point out that a leap forward in the development of optical antennas was made when nanoscale resolution fabrication was available in the form of electron-beam lithography. Designs capable of being printed as flat metal geometries were made to work and began to produce the first results for the reception of light waves. However, much earlier than these nanofabrication tools were commonly applied, some other technologies had already gained their place as photodetectors. Among them are those based on the photoelectric effect, which became fully developed with the use of semiconductor materials. Over the decades, semiconductor detectors, based on the development of the semiconductor industry, were refined to improve their performance in terms of spectral response, cut-off frequency, responsivity, and size. Thermal detectors, either thermoelectric or bolometric, were also used when semiconductor elements were not applicable for a given case. In the 1980s and 1990s infrared

detectors were facing some issues related to their performance in terms of cooling requirements and signal processing [Dereniak & Boreman, 1996]. This is when infrared antennas offered an innovative option that could use the intrinsic beneficial features of microwave and radioelectric design. At this time optical antennas were seen as a possible option with good added value in terms of selectivity in polarization, spectral response, short time response, and directivity. Unfortunately, the one drawback of these devices, their low responsivity, reduced their ability to challenge the already well-established technologies. Some decades after those first steps, the response of optical antennas has improved in terms of better impedance matching and improved transducers. However, response is still an important issue that will deserve significant attention in the years to come. The delay in the dissemination of this detection technology is mainly due to the behavior of metals at optical frequencies. The characteristics of a perfect conductor are lost in the infrared, and electromagnetic radiation thus penetrates the antenna structure, producing dispersive effects that change differently for each metal. Thus, optical antenna design differs from radioelectric antenna design. In optics, it is not only the geometry that is important; also, the shape and dimension of the resonant structure must be combined with a proper choice of metal to fabricate the structure without neglecting the effect of the surroundings of the antenna. Moreover, the coupling of the antenna with the transducer and the transducer efficiency become key factors in the development of a good optical antenna device [Boreman, 1996]. Up to now, we have described optical antennas as light detectors that use the currents generated in metallic resonant structures to produce a signal in the read-out external electronics. In addition, optical antennas have been proposed as energy harvesters when coupled to high-frequency rectifiers, mimicking the good results obtained in the radioelectric and microwave bands, and adapting the designs and constituent parts to the optical regime [Moddel & Grover, 2013]. Also, when thinking of optical antennas as emitters, optical antennas excited by optical radiation have made possible their use in nanoprobing devices that sense molecules in the near field with nanoscale resolution. Thus, optical antennas are at the core of a wide array of nanophotonic applications and devices [Novotny & Hecht, 2012] [Agio & Alù, 2013].

Radar and microwave techniques have also been beneficial for extending the use of metallic resonant structures to the optical regime. Frequency-selective surfaces, wire grids and retarders based on resonant elements, and reflectarrays were part of the technology commonly used in defense and security applications. Those advances pioneered the field of metasurface band-gap structures and photonic crystals. As has happened with the optical antenna designs that inherited the good results already proved in the microwave band, these passive resonant elements used designs that modified, using the current generated in the metallic shapes written on typically flat

surfaces, the spectrum, the polarization, and the phase of the incoming wavefront. We may say that, as occurred with the use of diffraction and interference in optical design, these additions to the optical tool kit paved the way to a new realm that can be called resonant optics [Puscasu, 2001] [Tharp, 2007] [Ginn, 2009] [Yu & Capasso, 2014] [Yu *et al.*, 2013]. With resonant elements being considered for enhancing near-field phenomena and promoting easier excitation of transitions, Raman spectroscopy, associated with near-field measurement techniques, makes possible important advances in the detection and analysis of molecular and biomedical substances. Finally, many of the results in nanophotonics have used resonant elements in the form of nano-antennas to reveal phenomena or modify the electric field distribution of light waves propagating at the nanoscale.

1.2 Organization of the Text

Before delving into the actual findings described in the book, we provide a short introduction to the basics of electromagnetism applicable to the interaction of light with metallic structures having a size comparable to the wavelength. The special behavior of metals deserves attention, to which Chapter 2 is devoted. The next three chapters are organized according to the manner in which we have made our contributions to this area. Chapter 3 explains how to model, design, and validate the proposed geometries through simulation. Chapter 4 describes techniques used for fabricating the most promising device designs. The fabricated devices are then tested and characterized to assess their actual performance and support the expected characteristics previously modeled or numerically evaluated. A variety of characterization techniques are described in Chapter 5. Chapters 6 and 7 describe the two main types of devices that we have developed: those producing an electric signal (antenna-coupled devices) and those changing the parameters of the light incident on the resonant elements (resonant optics). Finally, we close the book (Chapter 8) with a description of actual and future challenges that are currently being addressed or that will be met in new lines of research and future devices.

Upon completion of the book, the reader will know how optical antennas and resonant structures work, what their limitations and special characteristics are, and how the current technology and state of the art has provided some interesting devices that are applicable to a variety of fields in optics and photonics.

Chapter 2
Some Basic Electromagnetism

Classical electromagnetism and photonics share a common foundation. Light propagation and interaction, even at the nanoscale, is driven by Maxwell's equations and macroscopic parameterization of materials through their optical and electromagnetic properties [Jackson, 1998]. These equations relate the spatial and temporal variations of the displacement electric field, $\vec{D}$, and electric field, $\vec{E}$, with the magnetic field, $\vec{H}$, and magnetic induction, $\vec{B}$. Maxwell's four equations in their macroscopic form are given as

$$\nabla \cdot \vec{D} = \rho \text{ (Gauss' electric law)}, \tag{2.1}$$

$$\nabla \cdot \vec{B} = 0 \text{ (Gauss' magnetic law)}, \tag{2.2}$$

$$\nabla \times \vec{E} = -\frac{\partial \vec{B}}{\partial t} \text{ (Faraday's law)}, \tag{2.3}$$

$$\nabla \times \vec{H} = \frac{\partial \vec{D}}{\partial t} + \vec{j} \text{ (Ampere–Maxwell law)}, \tag{2.4}$$

where the electric charge, ρ, and current, $\vec{j}$, refer only to free unbound charges and currents. If it is necessary to move to the microscopic description of electromagnetic interactions, these equations still apply just by considering both bound and free charges and currents. The optical constants of the materials appear when considering the linear relations between fields:

$$\vec{D} = \epsilon_0 \vec{E} + \vec{P}, \tag{2.5}$$

$$\vec{H} = \frac{1}{\mu_0} \vec{B} - \vec{M}, \tag{2.6}$$

where ϵ_0 and μ_0 are the dielectric permittivity and magnetic permeability of vacuum, respectively. The effect of the material is described by the polarization, $\vec{P} = \chi_e \epsilon_0 \vec{E}$, and the magnetization, $\vec{M} = \chi_m \vec{H}$.

Maxwell's equations are the cornerstone of electromagnetism. This well-deserved recognition is based on the multiple consequences derived from them. One of the most relevant in optics is the existence of electromagnetic waves describing light. The wave equations for the electric and magnetic fields, $\vec{E}$ and $\vec{H}$, can be written as

$$\frac{1}{c^2}\frac{\partial^2 \vec{E}}{\partial t^2} - \nabla^2 \vec{E} = \mu_0 \frac{\partial}{\partial t}\left(\vec{j} + \frac{\partial \vec{P}}{\partial t} + \nabla \vec{M}\right) + \nabla(\nabla \cdot \vec{P}) - \frac{1}{\epsilon_0}\nabla \rho, \tag{2.7}$$

$$\frac{1}{c^2}\frac{\partial^2 \vec{H}}{\partial t^2} - \nabla^2 \vec{H} = \nabla \times \vec{j} + \nabla \frac{\partial \vec{P}}{\partial t} - \frac{1}{c^2}\frac{\partial^2 \vec{M}}{\partial t^2} + \nabla(\nabla \cdot \vec{M}), \tag{2.8}$$

which become the homogeneous wave equation when in vacuum ($\vec{P} = \vec{M} = \vec{j} = 0$, and $\rho = 0$). These wave equations are obtained by applying the rotational operator, $\nabla\times$, to Faraday's law and the Ampere–Maxwell law [Eqs. (2.3) and (2.4)], and using the relation between differential operators, $\nabla \times \nabla = \nabla \cdot \nabla - \nabla^2$. After that, Eqs. (2.1) and (2.2) are used to replace the divergence of the electric and magnetic fields, respectively, and finish the derivation of the wave equations.

From an engineering point of view, a favorable energy budget is one of the main design concerns. In the case of antenna theory and optical antennas, it is always important to know how much energy is radiated or received, and how this energy can be transduced towards the signal acquisition electronics. Maxwell's equations also deal with this problem and offer quite a simple solution. By manipulating Eqs. (2.1) to (2.4), it is possible to arrive at an expression known as the Poynting theorem, where the power delivered and transported by an electromagnetic wave is sectioned into meaningful parts. This relation describes what happens to the energy carried by an electromagnetic wave when this energy is evaluated over a given closed volume, v, limited by a surface, s:

$$\int_s (\vec{E} \times \vec{H}) ds = -\int_v \left(\vec{H}\frac{\partial \vec{B}}{\partial t} + \vec{E}\frac{\partial \vec{D}}{\partial t}\right) dv - \int_v \vec{j} \cdot \vec{E} dv. \tag{2.9}$$

The left hand side of this equation is the flux of a vector describing the power leaving the volume, v, through the surface, s. This is the Poynting vector, defined as $\vec{S} = \vec{E} \times \vec{H}$. On the right hand side we have two contributions. The first one corresponds to the electric and magnetic energy temporal variations within the volume, and the second one describes the dissipation loss in the form of Joule

heating. This last term can also be written using the relation between the current and the electric field, Ohm's law,

$$\vec{j} = \sigma \vec{E}. \tag{2.10}$$

This equation, along with the relation between the electric field, $\vec{E}$, and the displacement field, $\vec{D}$, [Eq. (2.5)], and the magnetic field and the magnetic induction field [Eq. (2.6)], are also known as constitutive relations. Then, when using Ohm's law in the description of the dissipated power, we find that

$$P_{\text{Joule}} = \int_v \sigma |\vec{E}|^2 dv. \tag{2.11}$$

Joule dissipation is of great importance when considering bolometric or thermoelectric transduction mechanisms because thermal dissipation produces temperature gradients and changes that are sensed using this transduction mechanism.

In optics it is quite convenient to work with monochromatic waves. The electric field temporal evolution is written as the following complex number: $\vec{E} = \vec{E}_0(x, y, z) \exp(-i\omega t)$, where $\vec{E}_0(x, y, z)$ represents the spatial distribution of the field at $t = 0$, and ω is the frequency of its temporal evolution. In this case, Maxwell's equations and the wave equations become simpler:

$$\nabla \cdot \vec{D}(x, y, z) = \rho(x, y, z), \tag{2.12}$$

$$\nabla \cdot \vec{B}(x, y, z) = 0, \tag{2.13}$$

$$\nabla \times \vec{E}(x, y, z) = i\omega \vec{B}(x, y, z), \tag{2.14}$$

$$\nabla \times \vec{H}(x, y, z) = -i\omega \vec{D}(x, y, z) + \vec{j}(x, y, z). \tag{2.15}$$

This complex representation is quite convenient when working with optical fields, but we should keep in mind that the actual value of the electric field is a real number that is expressed as $\text{Re}[\vec{E}_0 \exp(i\omega t)]$. A harmonic, or monochromatic, description of optical fields is always possible because any analytic signal [Mandel & Wolf, 1995] can be expanded as a collection of monochromatic plane waves using a Fourier representation.

2.1 The Drude–Lorentz Model

When considering the optical properties of materials, it is commonplace to use the Drude model as the applicable framework for describing light–matter interaction within the electromagnetic formalism.

The electrons of the atoms of a given material are primarily responsible for the optical properties of solids. These electrons are bound to their atoms by restoring forces that can be modeled as a damped harmonic oscillator. When light is incident on the material, the oscillator becomes forced. This physical situation is usually called the Drude–Lorentz model.

In one dimension, the equation of motion of these electrons is given as the forced and damped oscillator differential equation:

$$m\frac{d^2x}{dt^2} + m\gamma\frac{dx}{dt} + m\omega_0^2 = -eE, \tag{2.16}$$

where m is the mass of the charge carrier, γ is the damping constant of the oscillator, ω_0 is the natural oscillation frequency, e is the electron charge, and E is the electric field that forces the oscillator (for simplicity we are modeling a 1D case, and therefore the electric field can be considered as scalar). This field is assumed to be harmonic, having an angular frequency, ω, $E = E_0 e^{-i\omega t}$. The solution of this equation has the following general form:

$$x(t) = \frac{-eE_0/m}{\omega_0^2 - \omega^2 - i\gamma\omega}\exp[-i(\omega t - \phi)], \tag{2.17}$$

where ϕ is the phase shift between excitation and oscillation. The displacement of the charges produces a microscopic dipole, $p = -ex$, and a polarization due to the electric field as $P_{\text{resonance}} = Np$, where N is the number of charge carriers per unit of volume.

We have previously seen that the displacement field, $\vec{D}$, the electric field, $\vec{E}$, and the polarization, $\vec{P}$, are connected through Eq. (2.5). The polarization vector can be expressed as two contributions: one due to the intrinsic polarization of the material where the electric susceptibility, χ_e, is considered, and another one excited by the field-generated dipoles that are described as damped forced oscillators. Then, the displacement vector is given as

$$\vec{D} = \epsilon_0\left[1 + \chi_e + \left(\frac{Ne^2}{\epsilon_0 m}\right)\frac{1}{\omega_0^2 - \omega^2 - i\gamma\omega}\right]\vec{E}, \tag{2.18}$$

where the term inside the square brackets can be identified as the relative dielectric permittivity that is now a complex number because of the damping mechanism. This parameter is given as

$$\epsilon_r = 1 + \chi_e + \left(\frac{Ne^2}{\epsilon_0 m}\right)\frac{1}{\omega_0^2 - \omega^2 - i\gamma\omega}, \tag{2.19}$$

which can be split into the real and imaginary parts, $\epsilon_r = \epsilon_r' + i\epsilon_r''$:

$$\epsilon_r' = 1 + \chi_e + \left(\frac{Ne^2}{\epsilon_0 m}\right) \frac{\omega_0^2 - \omega^2}{(\omega_0^2 - \omega^2)^2 + (\gamma\omega)^2}, \tag{2.20}$$

$$\epsilon_r'' = \left(\frac{Ne^2}{\epsilon_0 m}\right) \frac{\gamma\omega}{(\omega_0^2 - \omega^2)^2 + (\gamma\omega)^2}. \tag{2.21}$$

The previous equations can be simplified depending on the relative importance of the natural frequency of oscillation, ω_0, the frequency of the incident field, ω, and the value of the damping factor, γ. The limits for low frequency and high frequency are

$$\epsilon_r(\omega = 0) = 1 + \chi_e + \frac{Ne^2}{\epsilon_0 m \omega_0^2}, \tag{2.22}$$

$$\epsilon_r(\omega = \infty) = 1 + \chi_e. \tag{2.23}$$

In a material with a collection of binding processes, each process adds its term to the dielectric constant, which now becomes

$$\epsilon_r = 1 + \chi_e + \sum_{j=1}^{M} f_j \left(\frac{Ne^2}{\epsilon_0 m}\right) \frac{1}{\omega_j^2 - \omega^2 - i\gamma_j\omega}, \tag{2.24}$$

where f_j describes the importance of the j^{th} resonance.

The previous reasoning shows how a simple physical model is able to describe the interaction of electrons and external electromagnetic fields. We should remind the reader here that most materials have a very weak response to magnetic fields. Therefore, when describing the interaction of light and matter, most of the phenomena can be modeled in terms of the response of the material to the electric field. This approach already provides an accurate description of the electric permittivity, which is closely linked to the optical properties of materials parameterized by the index of refraction.

2.1.1 Metals

Metals are characterized by the presence of free charge carriers in the form of an electron gas [Sondheimer, 1952] [Chambers, 1990]. The electrons belonging to this electron gas can be considered as free charges and therefore are exposed to the influence of electric fields that move them accordingly. In this case, the free carrier movement can be described by the forced and damped oscillator without a restoring force:

$$m\frac{d^2x}{dt^2} + m\gamma\frac{dx}{dt} = -eE_0 \exp(-i\omega t), \tag{2.25}$$

where the main difference between this equation and Eq. (2.16) is the absence of the natural frequency that was given by the restoring force experienced by

the bound electron. Now, electrons are free, and there is no restoring force. The solution to this equation is quite similar to the one obtained previously [Eq. (2.17)]:

$$x(t) = \frac{eE(t)/m}{\omega^2 + i\gamma\omega}. \tag{2.26}$$

Then, by applying a similar derivation that only takes into account the polarization due to the free carriers, we may write the relative permittivity as

$$\epsilon_r = 1 - \left(\frac{Ne^2}{\epsilon_0 m}\right)\frac{1}{\omega^2 + i\gamma\omega}. \tag{2.27}$$

Then, after defining the plasma frequency, ω_p, as

$$\omega_p = \sqrt{\frac{Ne^2}{\epsilon_0 m}}, \tag{2.28}$$

we may rewrite the dielectric permittivity as

$$\epsilon_r = 1 - \frac{\omega_p^2}{\omega^2 + i\gamma\omega}. \tag{2.29}$$

If the damping constant is negligible compared with the frequency ($\gamma \ll \omega$), the dielectric constant is real. This case will be treated when analyzing plasmons in section 2.1.5.

2.1.2 Relation between the index of refraction and the electric permittivity

There exists an intrinsic relation between the index of refraction, n, and the relative electric permittivity, ϵ_r. Following the notation and sign convention of [Fox, 2010], we may write the complex index of refraction as

$$\tilde{n} = n + i\kappa, \tag{2.30}$$

where the real part, n, describes the phase propagation of the electromagnetic wave, and κ accounts for the attenuation of the field when traveling through the material [Monacelli *et al.*, 2005]. The index of the medium can be related to the dielectric constant for non-magnetic materials as follows:

$$n = \sqrt{\epsilon}. \tag{2.31}$$

This relation is obtained when calculating the velocity of propagation of an electromagnetic wave in terms of the dielectric permittivity and the magnetic susceptibility. For non-magnetic materials, the relative magnetic susceptibility

is $\mu_r = 1$. From the previous relation, we may conclude that the electric permittivity has to be complex as well. Therefore, we may define

$$\tilde{\epsilon}_r = \epsilon_r' + i\epsilon_r''. \tag{2.32}$$

Using this definition and Eq. (2.31), we find that

$$\epsilon_r' = n^2 - \kappa^2, \tag{2.33}$$

$$\epsilon_r'' = 2n\kappa, \tag{2.34}$$

and

$$n = \frac{1}{\sqrt{2}}\sqrt{\epsilon_r' + \sqrt{\epsilon_r'^2 + \epsilon_r''^2}}, \tag{2.35}$$

$$\kappa = \frac{1}{\sqrt{2}}\sqrt{-\epsilon_r' + \sqrt{\epsilon_r'^2 + \epsilon_r''^2}}. \tag{2.36}$$

When the material is weakly absorbing ($\kappa \ll n$), some approximations can be made to produce a simpler version of the previous relations. In that case,

$$n = \sqrt{\epsilon_r'}, \tag{2.37}$$

$$\kappa = \frac{\epsilon_r''}{2n}. \tag{2.38}$$

This means that the index is mainly related to the real part of the permittivity, and the absorption is mainly related to its imaginary part.

2.1.3 Conductivity

Conductivity becomes a basic parameter in the understanding of the interaction of metals and optical radiation. The well-known Ohm's law relates the electric field and the current density vector through conductivity. Additionally, the temporal response is of great importance when considering the anomalous skin effect that corresponds with some deviations of the Drude model [Shelton *et al.*, 2008b]. Within the Drude–Lorentz model it is possible to write the differential equation (2.25) in terms of the velocity of the charge carriers, v. Now, this differential equation becomes linear:

$$m\frac{dv}{dt} + m\gamma v = -eE, \tag{2.39}$$

and its solution produces the following function for $v(t)$:

$$v(t) = \frac{-e\tau}{m} \times \frac{1}{1 - i\omega\tau} E(t), \tag{2.40}$$

where $\tau = \gamma^{-1}$. This τ can be seen as the momentum scattering time constant. By definition, the electric current density is given as $j = -Nev$. Also, from Ohm's law, there is a linear relation between the electric field and the electric current density, $j = \sigma E$, where σ denotes the electric conductivity. Then, by using these previous relations, we find conductivity as the following complex quantity:

$$\sigma(\omega) = \frac{\sigma_0}{1 - i\omega\tau}, \tag{2.41}$$

where $\sigma_0 = \frac{Ne^2\tau}{m}$, with the conductivity at $\omega = 0$, is the DC electric conductivity.

When comparing the dielectric constant, ϵ_r [Eq. (2.27)], and conductivity, σ [Eq. (2.41)], we may write the following relation:

$$\epsilon_r(\omega) = 1 + \frac{i\sigma(\omega)}{\epsilon_0\omega}. \tag{2.42}$$

Therefore, the complex values of the electric permittivity can be used to obtain the value of the complex AC conductivity. If we consider that $\sigma = \sigma' + i\sigma''$, we may relate both the real and imaginary parts of the dielectric permittivity [Eqs. (2.33) and (2.34)] to the real and imaginary parts of the conductivity:

$$\sigma' = \epsilon_r''\epsilon_0\omega = 2nk\epsilon_0\omega, \tag{2.43}$$

$$\sigma'' = (1 - \epsilon_r')\epsilon_0\omega = (1 + k^2 - n^2)\epsilon_0\omega, \tag{2.44}$$

which can also be written as

$$\sigma = i\omega\epsilon_0[1 - (n + i\kappa)^2]. \tag{2.45}$$

When considering the meaning of a complex conductivity, it is worthwhile to consider the relation between the electric field, E, and the current density, j, given by Ohm's law [Eq. (2.10)]. In this case, a complex conductivity can be seen as a phase shift between the incident electric field and the induced current. As far as the current density describes the movement of electrons, this phase shift can be seen as reflecting the fact that the electrons cannot be fully in sync with the electric field that drives their movement.

2.1.4 Skin depth and impedances

When an electromagnetic wave at optical frequencies interacts with a metallic structure, the wave penetrates the material, and the associated electric vector for normal incidence conditions can be described as

$$E(z) = E_0 \exp(i\gamma z), \tag{2.46}$$

where z is the coordinate along the direction of propagation perpendicular to the interface, and γ is the propagation constant within the metal. This constant can be written in terms of the complex index of refraction [Eq. (2.30)] as

$$\gamma = \frac{\omega(n + i\kappa)}{c}, \tag{2.47}$$

where c is the speed of light in vacuum. When the metal is shaped as a dipole antenna and the electric field of the incoming wavefront is aligned along the dipole length, incremental currents are induced at the dipole location. The complete analysis should take into account the vector character of the electric field, $\vec{E}$, and the induced current densities, $\vec{j}$, but the previously described conditions allow a simpler description of the physical mechanism. These field-induced incremental current densities sum up to produce a current, I, that is given as

$$I = w \int_0^t j(z)dz, \tag{2.48}$$

where w and t are the width and thickness of the dipole, respectively. In this equation, the current density, j, is related to the electric field given in Eq. (2.46), E, by Ohm's law [Eq. (2.10)]. After some algebra, the intensity is written as

$$I = w\sigma\delta_{\text{skin}}E_0[1 - \exp(-t/\delta_{\text{skin}})], \tag{2.49}$$

where the attenuation along the direction of the propagation within the metal defines the skin depth of the material:

$$\delta_{\text{skin}} = \frac{c}{\omega\kappa}. \tag{2.50}$$

Therefore, skin depth, δ_{skin}, characterizes the region within the metal where the incoming wavefront is propagating and interacting with the material before dissipating all of its energy. This value can be used to properly establish the thickness of the resonant structures deposited on a substrate. Thicknesses above 3 or 4 times the skin depth already block further propagation into the metal. By using the optical constants of materials obtained from [Palik, 1997] and from *in situ* spectroscopic ellipsometry measurements, it is possible to evaluate the skin depth as a function of the wavelength for a variety of metals [Eq. (2.50)] [Cuadrado *et al.*, 2013a]. Some results are shown in Fig. 2.1.

On the other hand, the same electromagnetic wave that excites currents along the dipole length also establishes a voltage on the dipole, given as

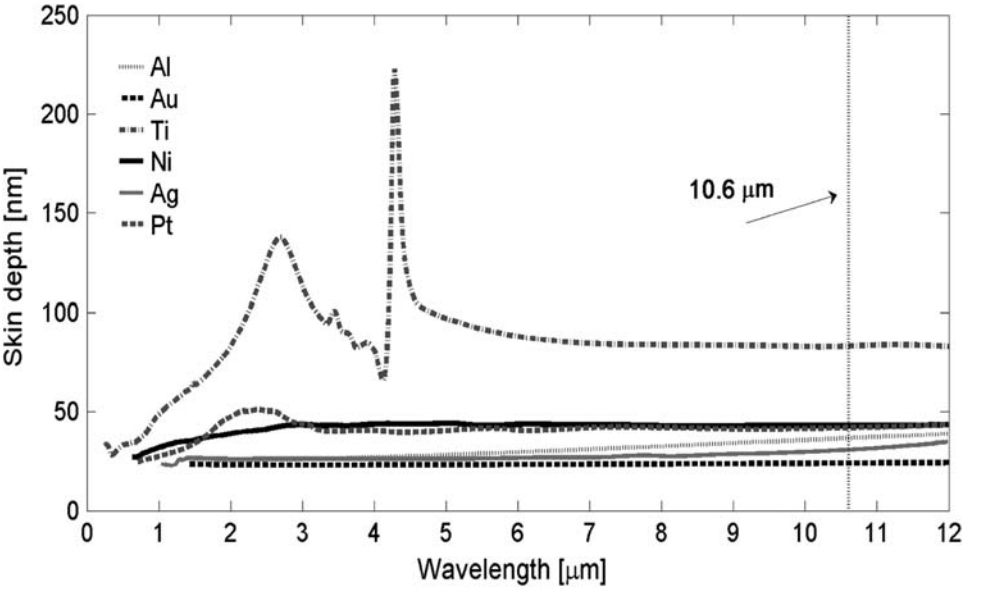

Figure 2.1 Spectral variations of the skin depth for various metals typically used in the fabrication of optical antennas and resonant structures in the infrared. The vertical line at $\lambda = 10.6\,\mu$m marks the usual wavelength emitted by a CO_2 laser. This type of laser is the most common light source for characterizing and testing these devices (adapted from [Cuadrado *et al.*, 2013a] and reproduced with permission of SPIE).

$$V = E_0 l, \tag{2.51}$$

where l is the length of the dipole. By using Eqs. (2.49) and (2.51), it is possible to define the following impedance [Ginn *et al.*, 2009]:

$$Z_{\text{dipole film}} = \frac{V}{I} = \frac{l}{w\omega\epsilon_0\delta_{\text{skin}}[1-\exp(-t/\delta_{\text{skin}})][2n\kappa + i(\kappa^2 - n^2 + 1)]}, \tag{2.52}$$

where w and t are the width and thickness of the dipole, respectively. In this equation we have made use of the relation between conductivity and index of refraction [Eq. (2.45)]. This impedance can be rewritten in terms of the electric relative permittivity, $\epsilon_r = \epsilon_r' + i\epsilon_r''$, applied to the typical case in the infrared, where $\epsilon_r' \ll -1$. The result can be given in terms of the real and imaginary parts of the impedance, $Z = R + iX$:

$$R_{\text{dipole film}} \simeq \frac{l}{w\omega\epsilon_0\delta_{\text{skin}}} \times \frac{\epsilon_r''}{\epsilon_r'^2 + \epsilon_r''^2}, \tag{2.53}$$

$$X_{\text{dipole film}} \simeq \frac{l}{w\omega\epsilon_0\delta_{\text{skin}}} \times \frac{\epsilon_r'}{\epsilon_r'^2 + \epsilon_r''^2}, \tag{2.54}$$

which provides a primarily capacitive response due to the typical large negative value of ϵ_r' for metals in the infrared.

2.1.5 Plasmons

When analyzing the dependence of the dielectric permittivity for metals as a function of the frequency [Eq. (2.29)], for the case of a weak damping factor (the term in the denominator becomes real and equal to ω^2), this permittivity approaches zero when $\omega = \omega_p$. In order to determine what is happening at the plasma frequency, we may imagine the metal as a crystalline lattice of positive ions immersed in an electron gas. If the whole electronic cloud moves in one direction, the positive ions of the lattice will create a force opposed to the movement direction of the electrons. This force will move the electrons backwards. The continuous movement of the electrons under a harmonic excitation can be seen as an oscillation of the electron gas with respect to the fixed lattice of positive ions.

This oscillation is bounded by the surface of the metal. Then, when the electron gas reaches the surface, it creates a negative-charge region that is compensated by a positive-charge region in the opposite direction and also located at the surface of the metal. The equation governing this movement for a unit volume of the electron gas is

$$\frac{d^2u}{dt^2} + \left(\frac{Ne^2}{\epsilon_o m}\right)u = 0, \tag{2.55}$$

where u is the net displacement of the electron cloud center of mass with respect to the ion lattice, and N is the density of electrons per unit of volume. The angular frequency of this movement is $\omega_{\text{plasmon}} = \sqrt{\frac{Ne^2}{\epsilon_0 m}}$. The quantized oscillation of the electron gas at the surface of a metal is called a plasmon. Plasmons can be observed by Raman spectroscopy, and they can also be excited by an appropriate light wave.

Free electrons can also promote the creation of charge oscillations at the surface of metals. These oscillations are denoted as surface plasmon resonances, whose existence critically depends on the matching of the wave vectors, $\vec{k}$, on both sides of the metal–dielectric interface where the plasmon is created. The strong dependence of this resonance on angle and wavelength makes possible its use in a wide range of plasmonic sensors.

2.2 Impedance Matching

The interaction of electromagnetic waves propagating through different material media and structures can be modeled using a common tool and concept in electrical engineering: impedance and impedance-matching conditions.

In the optical regime, impedance definitions and matching require some adaptation to the case of dispersive and attenuating materials [Alù & Engheta, 2008] [Cuadrado *et al.*, 2016] [Xu *et al.*, 2016], including the presence of parasitic loads around the detecting elements [Engheta *et al.*, 2005] [Cuadrado *et al.*, 2015c] [Greffet *et al.*, 2010] [Huang *et al.*, 2009].

For the propagation of electromagnetic waves, materials can be characterized by an intrinsic impedance. This is denoted as wave impedance and is defined by

$$Z = \sqrt{\frac{\mu_0 \mu_r}{\epsilon_0 \epsilon_r}} = \mu_0 \mu_r \frac{c}{n}, \tag{2.56}$$

where μ_0 and ϵ_0 are the magnetic permeability and dielectric permittivity of vacuum, respectively, and μ_r and ϵ_r are the relative magnetic permeability and dielectric pemittivity of the medium, respectively; c and n are the speed of light in vacuum and the index of refraction of the material, respectively. For vacuum, the result is known as the vacuum impedance value, $Z_0 = 377\ \Omega$. This value is sometimes used to define normalized load impedances as $z = Z/Z_0$.

The definition of wave impedance in Eq. (2.56) coincides with the ratio of the electric field, E, to the magnetic field, H. If ϵ_r and n can be complex when describing lossy materials and metals, then Z is a complex impedance that can take a capacitive or inductive character. In general, the complex impedance is given as a real resistive part and an imaginary reactive impedance: $Z = R + iX$.

When coupling radiation to an antenna-coupled detector, the propagating wave interacts with the antenna that is loaded with the transducer element [Olmon & Raschke, 2012]. The optimum transfer of power between the propagating wave and the antenna load depends on adequate impedance matching along the system. This condition occurs when the impedances are related to each other as complex conjugates. The impedances involved here are the load impedance, $Z_l = R_l + X_l$, and the input impedance of the antenna, $Z_a = R_a + X_a$, where the resistive part, R_a, is sometimes split as a radiation resistance contribution (responsible for the scattered radiation) plus a dissipative resistance (responsible for the heating loss at the antenna). When matching these impedances, the reactive power stored at the LC circuit cancels because the circuit becomes purely resistive ($X_a = -X_l$), and both the load and the antenna equally share the available power [Balanis, 2005]. This impedance matching can also be described as an equivalent circuit model. However, resonant elements, such as meander lines, frequency-selective surfaces, and reflectarrays, are not coupled to any load for transduction. Then, the impedance problem is primarily related to the description of wave propagation using impedance matching with the surrounding media.

When moving through an interface between two materials, impedance mismatch explains how electromagnetic fields are reflected and/or transmitted by the interface. The reflection coefficient of this interface is given as

$$r = \frac{Z_2 - Z_1}{Z_2 + Z_1}, \tag{2.57}$$

which, in circuit theory, is typically denoted as Γ. This equation is equivalent to the Fresnel reflection coefficient in optics that is written in terms of the index of refraction of the materials forming the interface. Associated with this reflection, a transmission can be given as

$$t = 1 + r. \tag{2.58}$$

The sign in this equation depends on the sign convention for defining a positive reflection coefficient across the surface. In this case, a positive sign means that the reflected and transmitted electric and magnetic fields are parallel to the incident fields.

2.2.1 Impedance definitions from the energy budget

When obtaining the power balance equation for an electromagnetic wave [see the Poynting theorem in Eq. (2.9)] we can define the radiated power associated with the flux of the Poynting vector. Also, electric and magnetic fields describe the contributions of the pure electric and pure magnetic energy and power. Finally, the Joule dissipation accounts for losses in the media. This power distribution can also be linked to the impedances associated with those contributions. To do that, we define a closed volume, v, where the radiation and the resonant element are placed. Radiated power is described by the propagation of the Poynting vector scattered by the resonant element, $\vec{S}_{\text{scat}}$, as

$$P_{\text{rad}} = \int_s \vec{n}\,\vec{S}_{\text{scat}} ds, \tag{2.59}$$

where $\vec{n}$ is the normal vector to the surface, s, enclosing the volume, v. At the same time, power, P, in an electromagnetic circuit is associated with the product of voltage, V, and current, I. Also, voltage and current are related through Ohm's law as $R = V/I$. Then, it is straightforward to relate power and resistance as

$$R = \frac{P}{I^2} = \frac{V^2}{P}, \tag{2.60}$$

and radiation resistance is finally given as

$$R_{\text{rad}} = \frac{P_{\text{rad}}}{|I|^2}, \tag{2.61}$$

where I is the amplitude of the current flowing in through the antenna feed.

In the radiation regime, radiation resistance can be calculated analytically from basic antenna theory for several simple cases [Balanis, 2005]. The case of a half-wave dipole is given as

$$R_{\text{rad}} = \frac{2\pi}{3}\left(\frac{l}{\lambda}\right)^2 Z_0 \simeq 789\left(\frac{l}{\lambda}\right)^2 \Omega, \tag{2.62}$$

where λ is the wavelength, l is the length of the dipole, and $Z_0 = 377\ \Omega$ is the vacuum impedance.

Joule heating also contributes to the power budget as a dissipation factor, and following a similar reasoning as for the radiation resistance, it is possible to define a loss resistance as

$$R_{\text{loss}} = \frac{P_{\text{loss}}}{|I|^2}, \tag{2.63}$$

where

$$P_{\text{loss}} = \int_{v_{\text{ant}}} \vec{j}^{*}\vec{E}dv, \tag{2.64}$$

where * means complex conjugation, and the integration is carried out within the volume of the resonant element, v_{ant}. Both loss and radiation resistances are combined in the electric resistance of the antenna:

$$R_{\text{elec}} = R_{\text{rad}} + R_{\text{loss}}. \tag{2.65}$$

Radiation and loss resistance are real valued and contribute to the real part of the impedance of the antenna or resonant element. However, the interaction of the electromagnetic wave with the structure also excites electric and magnetic fields that contain electric and magnetic energy in a reactive form.

For an antenna-coupled diode, the reactive part is easily identified with the diode itself and is described as a capacitive load in parallel with the resistive impedance, having a value related to its geometry through its transverse area, A, and gap thickness, d, and also to the electric permittivity of the insulator material, ϵ (see Fig. 2.2.a). The diode is located at the feed point of a two-arm dipole. The capacitance will be important when considering the cut-off frequency of these devices. More complicated arrangements, such as transmission lines, can be also modeled using equivalent circuit concepts. Figure 2.2.c shows the coupling of two dipole antennas to a metal-oxide-metal (MOM) diode using an asymmetric configuration of coplanar strip lines. These waveguides work as transmission lines carrying the high-frequency signal from the dipole antenna to the transducer. The transmission lines show attenuation, and this effect can be modeled as a resistive load distributed

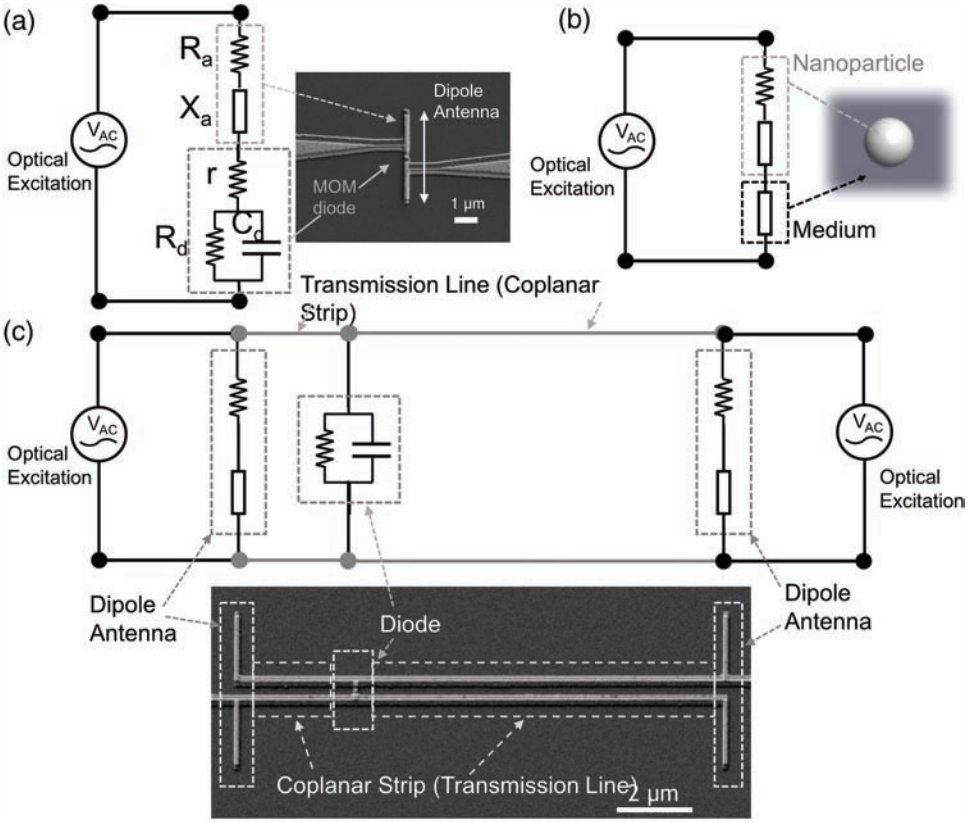

Figure 2.2 An equivalent circuit model depicted for three cases: (a) an antenna detector coupled to a diode, (b) a nanoparticle within a dielectric matrix, and (c) a system coupling the signal from two dipole antennas to a MOM diode though two coplanar strips with different lengths. In this last case, both antennas are excited simultaneously by the incoming optical radiation (adapted from [Slovick, 2011]).

along the line. In this configuration, the asymmetry of the transmission lines can be used to sense a phase delay in the incoming optical excitation equivalent to a tilted incidence direction. After transduction in the load, the phase information of the currents is lost and the signal can be extracted as coming from the diode connections.

In the case of resonant nanoparticles, the imaginary part of the impedance can be extracted from the electric and magnetic powers through

$$X = \frac{P_{\text{reactive}}}{|I|^2}, \tag{2.66}$$

where the reactive power is calculated from the Poynting theorem [Eq. (2.9)] as

$$P_{\text{reactive}} = \omega \int_v (\epsilon_r' |\vec{E}|^2 + \mu_r |H|^2) dv, \tag{2.67}$$

and where we are assuming that the magnetic permeability of the material is real, and the integration is carried out within the volume of the nanoparticle. At the same time, this evaluation needs to be done in the medium surrounding the nanoparticle to take into account the contribution of the media (see Fig. 2.2.b).

2.2.2 Equivalent circuit for antenna-coupled diodes

When antennas work as harvesters of electromagnetic radiation, they couple the incident power to a load properly connected to the antenna. This loading of the antenna has to be optimum to deliver as much power as possible from the incoming wave to the load. Radioelectric antennas perform this job quite efficiently based on the behavior of the antenna arms as near-perfect metals with very little absorption. In any case, antennas are commonly characterized by a complex impedance. This impedance is also denoted as the input impedance. The real part of the input impedance describes the dissipative and radiative losses, corresponding to the Joule heating and re-radiated or scattered radiation, respectively. The imaginary part is strongly dependent on the excitation frequency. For an optimum power transfer between the antenna and the load, both parts have to have complex conjugate impedances: the same values for the real part and imaginary parts as well as opposite signs for the imaginary parts. At this point, we should recall that, even in this optimum matching condition, only half of the power collected by the antenna is delivered to the load [Balanis, 2005]. When moving to the optical regime, the concept of input impedance and impedance matching remains, but its realization is not exactly the same. For example, the impedance of a radioelectric antenna is almost exclusively linked to the geometry of the antenna and the feed point. However, at higher frequencies, where metals stop behaving as perfect conductors, material properties are of great importance when considering absorption and resonances. As we have previously explained, the description of the interaction of light with metals at infrared and visible frequencies needs the Drude–Lorentz model to explain absorption, reflectivity, and some other interesting phenomena. From an antenna design point of view, one of the most relevant changes is the scaling of the geometrical relations by means of the use of an effective wavelength. This effect is related to the excitation of the surface plasmon polariton resonances [Cubukcu & Capasso, 2009] and to the skin depth penetration of the incoming radiation [Novotny, 2007].

A common type of antenna-coupled IR sensor is the MOM diode. The impedance interaction between the diode and the antenna determines the response speed of the diode. The MOM diode can be described by a junction

capacitance, C_d, in parallel with a nonlinear voltage-dependent resistance, $R_d(V)$. This parallel combination is in series with the resistance, r, which represents metal-lead resistance and/or spreading resistance [Sanchez *et al.*, 1978]. An antenna functioning as a receiver of the infrared radiation can be described by an AC source that is the time-dependent excitation induced by the incoming light. This is connected in series with impedance $R_a + jX_a$, where R_a is the real impedance of the antenna, and X_a is the reactive impedance that is zero at the resonant frequency. This model is presented in Fig. 2.2.a. In this model the antenna shows a complex impedance having a real part, R_a, and a imaginary part, X_a, that is dependent on the frequency of the excitation. The imaginary part of this impedance cancels out at the resonant frequency. In this figure, the diode is represented as the parallel combination of R_d and C_d, in series with r. For this circuit, the RC time constant is determined by the parallel combination of the diode capacitance, C_d, and the equivalent diode resistance, R_d, in series with R_a and r. This leads to a cut-off frequency, f_c, of

$$f_c = \frac{1}{2\pi RC} = \frac{R_a + r + R_d(V)}{2\pi(R_a + r)R_d(V)C_d}. \tag{2.68}$$

While rectification and mixing are still observed above this frequency, its efficiency diminishes. To minimize the response time of the diode and attain a high cut-off frequency, the diode capacitance must be small. If the capacitor considered can be modeled as a small parallel-plate capacitor, the diode capacitance, C_d, is

$$C_d = \frac{\epsilon_{ox}\epsilon_0 A}{d}, \tag{2.69}$$

where ϵ_{ox} is the relative permittivity of the oxide in the MOM diode, ϵ_0 is the permittivity of free space, A is the junction area, and d is the thickness of the dielectric. For a diode with a 25 Å barrier composed of Al_2O_3, with a relative permittivity at 28.3 THz approximately equal to 1 [Momida *et al.*, 2007] [Rajab *et al.*, 2008] and an equivalent resistance of 1 kΩ, a $75 \times 75\,nm^2$ or smaller overlap area is required to obtain a cut-off frequency high enough to rectify 10.6 μm incident radiation. Discussions of impedance matching at IR frequencies can be found in several contributions, with an excellent discussion in [Olmon & Raschke, 2012].

2.2.3 Resonant structures

Meander lines, frequency-selective surfaces, and reflectarrays transmit, or reflect, light according to the characteristics of the element that interacts with the incoming radiation. A circuit equivalent model is quite useful in this case to better understand how this interaction occurs and how to analyze the

results in terms of reflected and transmitted waves along a transmission line [Munk, 2000]. These structures can be taken as impedance elements located at the interface between two media (see Fig. 2.3), and spaced by a dielectric film with thickness comparable to the wavelength (see Fig. 2.4). This dielectric layer works as a transmission line connecting consecutive impedances. Therefore, the concept of transmission lines to model the propagation of light between multiple-layer resonant structures makes the analysis easier and directly written in electrical-engineering terms.

For example, a meander-line single layer can be modeled as two orthogonal transmission lines, one for each orientation of the electric field. One of these transmission lines (along the spacing) has a capacitive impedance, and the other (along the meanders) has an inductive impedance. The net result along the transmission line is a net phase delay between the two components, explaining the observed retardation. Figure 2.3 shows how these two transmission lines are associated with the geometry of the structure. Also, in Fig. 2.4 we show the equivalent circuit of a three-layer meander line. These structures can work in reflection or transmission. When in reflection, the

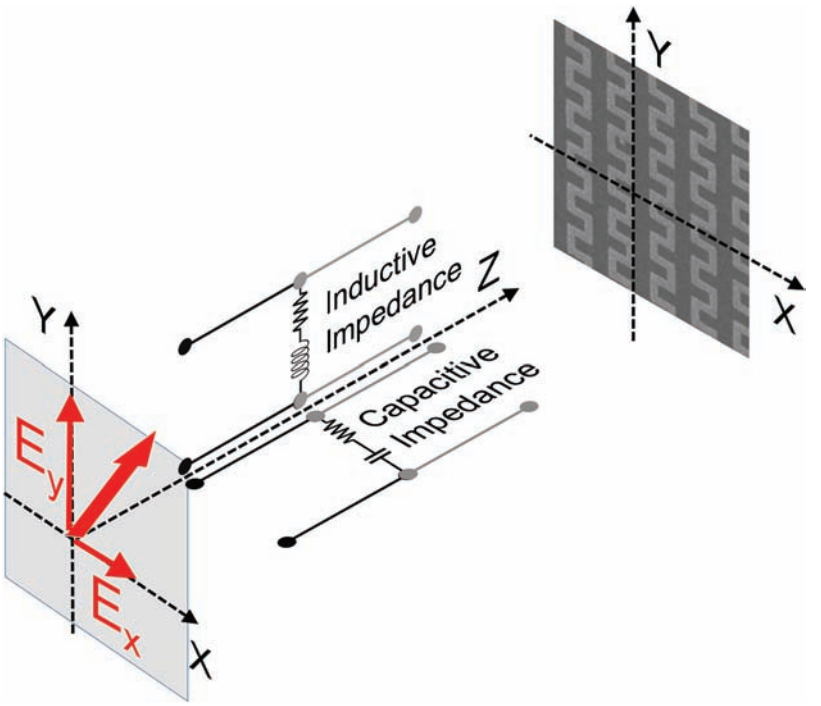

Figure 2.3 Equivalent circuit model for a single-layer meander line. Two transmission lines act as capacitive and inductive loads for the two components of the field. The geometry of the device is linked to the capacitive or inductive character of the impedance.

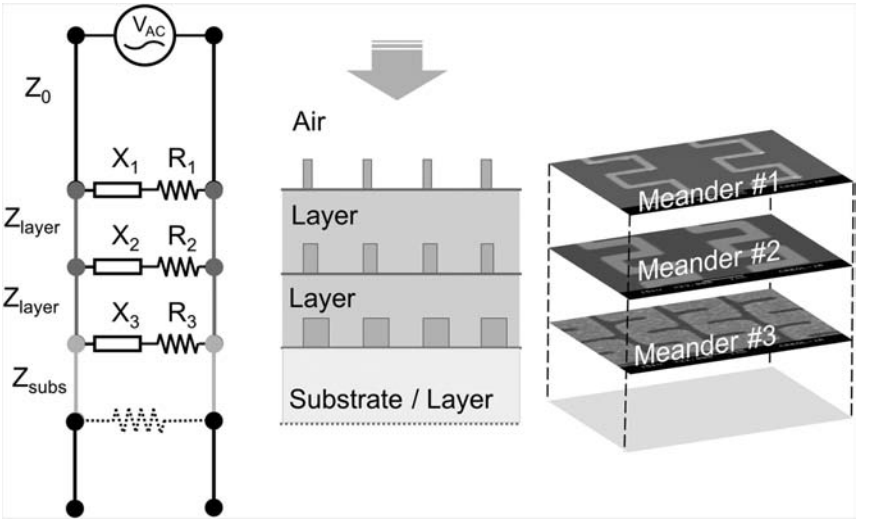

Figure 2.4 A multilayer meander-line structure (center and right) is modeled as a transmission line (left). The imaginary part of the impedance, *X*, is capacitive or inductive depending on the orientation of the electric field vector of the incident radiation (see Fig. 2.3). For transmissive devices, the transmission line is terminated by the substrate material. For reflective devices, a ground plane is placed under the meander-line structure. This ground plane is modeled as a resistive load. Different materials show different impedances.

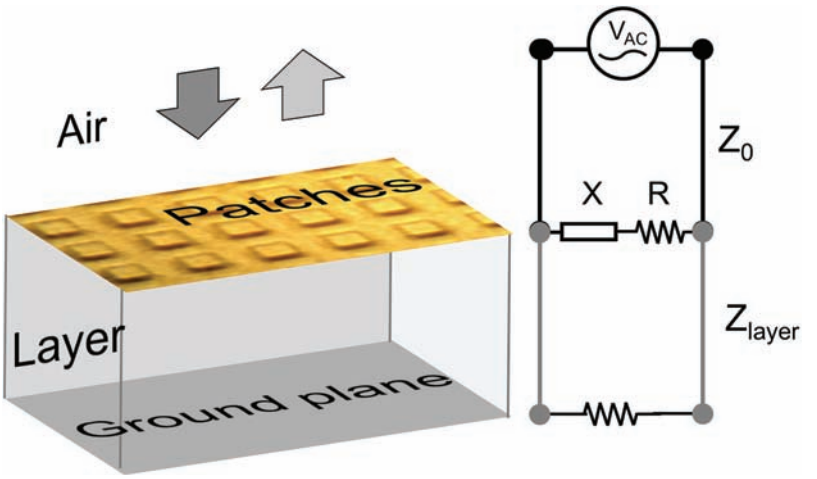

Figure 2.5 Reflectarrays modeled as a complex impedance associated with the resonant elements (square patches) followed by a waveguide representing the stand-off layer of the resonant patches. The ground plane terminates the transmission line as a resistive load to model its dissipative loss.

transmission line is terminated with a resistive load that models a dissipative ground plane (this has been plotted with dashed lines in the equivalent circuit). Different materials along the transmission line are characterized by different impedances. If those materials are absorbing radiation, then some resistive load needs to be included in the transmission line model. These impedance mismatches will cause reflections at the interfaces.

Reflectarrays can also be modeled using a circuit equivalence. In Fig. 2.5 we show how the plane where the resonant elements are placed can be described by a complex impedance. In this case the elements are square patches. The thickness of the layer between the patches and the ground plane works as a waveguide, and the ground plane reflects back the light (except for some dissipation given by the resistive load).

Chapter 3
Modeling, Design, and Simulation

Infrared antennas and resonant structures take advantage of the successful designs in the radioelectric and microwave spectra. A quite simple and naïve approach would be to consider the geometry and shape of those designs and transfer them into the optical regime with simple wavelength structure size scaling. However, this translation misses the specific behavior of metals and dielectrics at optical frequencies, and how these characteristics can strongly change the geometries and arrangements of a working antenna in the infrared.

3.1 Material and Fabrication Constraints

Fabrication of optical antennas and resonant structures has been possible only since technology has provided tools and processes able to produce smooth metallic surfaces with sizes ranging in the subwavelength scale for the optical domain. This means that resonant elements are nanophotonic devices and systems. This tiny size also needs an appropriate approach for the design of working elements. The first constraint is related to the physical substrate that the antennas are placed on or embedded in. Most of the antenna-coupled detectors and resonant structures are written on a dielectric substrate or on a dielectric stand-off layer deposited on top of a metallic surface that typically has been evaporated on a dielectric substrate. The thicknesses of these layers are a fraction of a wavelength, and the substrates are dielectric wafers, or plastic flexible substrates [Shelton *et al.*, 2007]. When the device is illuminated from the substrate side, the substrate has to be transparent enough for the given wavelength of operation. In any case, the optical properties of every material involved in the proposed design have to be properly included in the design and modeling of the device. But not only optical properties are important. When thermal effects are at play, thermal conductivity and electrothermal coefficients are also of interest and need to be considered.

In section 2.1.4 we saw how the imaginary part of the index of refraction, κ, affects the value of the skin depth for different materials. This means that when changing the material, the radiation will interact with different volumes of the antenna structure, building current distributions that also differ from material to material. In Fig. 3.1 we have represented the optimum length of a dipole antenna fabricated with different metals and deposited on a Si wafer coated with an insulating SiO_2 layer. We see that the optimum length decreases when increasing the skin depth, δ_{skin} [Cuadrado *et al.*, 2013a] [Cuadrado, 2014].

As has been demonstrated, the optimum length of a dipole antenna working at the first resonant wavelength differs from the $\lambda/2$ design applicable to the radioelectric spectrum. In the optical range, the effect of the induced surface charge waves gives rise to the concept of effective wavelength. Novotny [Novotny, 2007] describes the resonant element as a metallic waveguide, where the electric field fills the material and produces charge oscillations at the interface between the metal and the surrounding material. The main conclusion is summarized as the following linear relation:

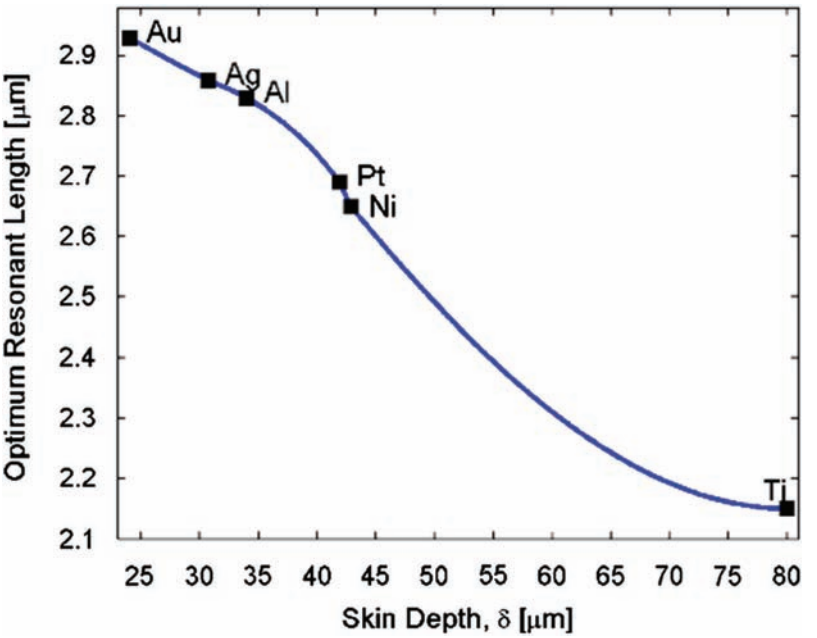

Figure 3.1 Variation of the dipole length that produces the maximum signal as a function of the skin depth of the material. The dipole has a width of 200 nm and a thickness of 100 nm, and is deposited on a Si wafer coated with a SiO_2 layer 1.2 μm-thick. The wavelength used in this calculation is $\lambda_0 = 10.6\,\mu m$. The line connecting the points corresponding with the analyzed metals is obtained from the interpolation of the optical constants of the limiting metals at each portion (adapted from [Cuadrado *et al.*, 2013a] and reproduced with permission of SPIE).

$$\lambda_{\text{eff}} = a_1 + a_2 \frac{\lambda_0}{\lambda_p}, \tag{3.1}$$

where λ_0 is the wavelength in vacuum, and λ_p is the plasma wavelength of the material of the resonant element. The coefficients a_1 and a_2 depend on the geometry of the resonant element as well as the dielectric permittivities of the surrounding medium and the metal. This relation makes it possible to adapt those designs valid at radioelectric frequencies to the optical range.

3.1.1 The role of the substrate

For the case of dipole or patch antennas deposited onto a substrate, there exists another wavelength scaling due to the fact that half of the antenna is in contact with the substrate and the other half is typically embedded in air. We assume that air is equivalent to vacuum. In this case, the effective wavelength seen by the resonant element is

$$\lambda_{\text{eff}} = \frac{\lambda_0}{\sqrt{\frac{1}{2}(\epsilon_0 + \epsilon_s)}}, \tag{3.2}$$

where ϵ_0 and ϵ_s are the electric permittivities of the vacuum and the substrate, respectively, and $\lambda_{\text{eff}} = 2.97\,\mu\text{m}$.

These scaling factors have been experimentally demonstrated when analyzing the antenna response in the infrared at a fixed wavelength [Fumeaux *et al.*, 2000]. A collection of 30 dipole-antenna-coupled bolometers were fabricated on a Si wafer, on top of a 200 nm layer of SiO_2 for electrical and thermal isolation. The length of the dipole ranged between 0.7 and 20 μm. For all of the antenna lengths tested, the polarization-dependent signal was measured as a function of the length, L. The results are plotted in Fig. 3.2 and are presented with measurements obtained at a fixed wavelength ($\lambda = 10.6\,\mu\text{m}$). The measured curve exhibits a first resonance for antennas with a length shorter than 2.5 μm, and was not well defined in the measurement because of the dimensions of the bolometer and bond pads relative to the antenna length. Past the first resonance, the measurements show a first minimum around $L = 5\,\mu\text{m}$ and a second maximum for $L = 7.5\,\mu\text{m}$. In this experiment, the interpretation of the resonant lengths in terms of the free-space wavelength of the incident radiation is not straightforward because of the layered substrate.

The minimum appearing at $L = 5\,\mu\text{m}$ can be interpreted as the mode of the current distribution showing a minimum value at the feed point where $L = 2\lambda$. These results indicate an apparent wavelength, $\lambda_{\text{app}} = 2.5\,\mu\text{m}$, that is a little shorter than the expected effective wavelength obtained from Eq. (3.2), i.e., $\lambda_{\text{eff}} = 2.79\,\mu\text{m}$. This difference is mostly caused by the effect of the bond pads adjacent to the antenna arms. The measured width of the

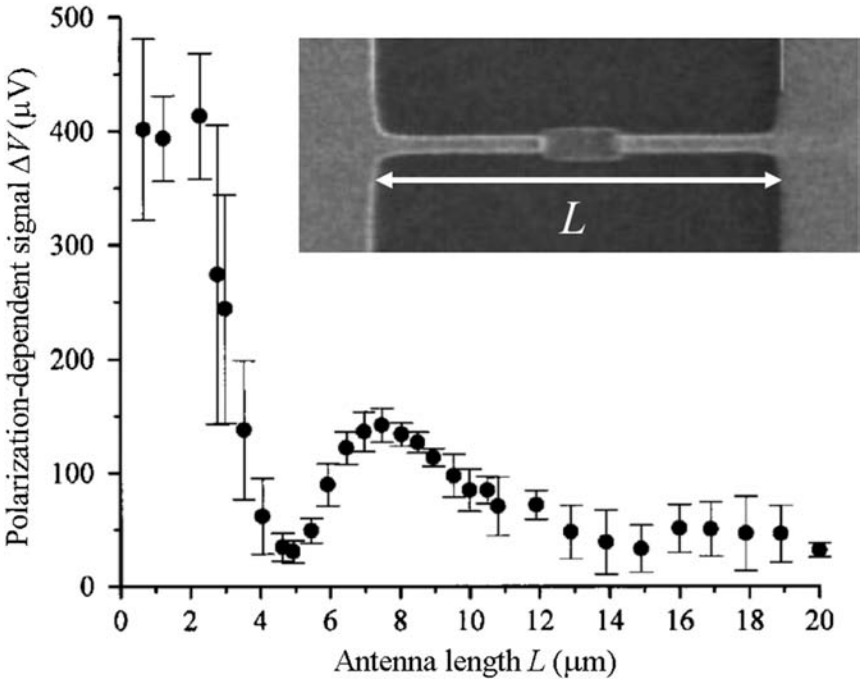

Figure 3.2 A collection of dipole antennas coupled to Nb nanobolometers are tested at a fixed wavelength ($\lambda = 10.6\,\mu m$). The response of the antenna is plotted versus the antenna length. The mean and standard deviation of the signal are shown. Four devices are measured for every value of *L* (adapted from [Fumeaux *et al.*, 2000] and reproduced with permission of Elsevier).

first resonance is broad enough to contain resonances corresponding to $\lambda/2$, $\lambda\Delta$, and $3\lambda/2$.

Actually, when thermal and electric isolation is of importance for the transduction mechanism or for enhancement of a resonance, it is beneficial to place the antenna on a stand-off layer made of a dielectric material [Middleton & Boreman, 2006]. The arrangement of optical antennas on photonic crystals and metamaterial substrates is also of interest because it allows the spectral response of the antenna to be tuned to that of the photonic crystal [González & Alda, 2010a] [González & Alda, 2010b] [González & Alda, 2011]. A simple configuration that works for the infrared is the use of a Si wafer coated with a SiO_2 thin layer. The thickness of this layer is selected to reduce thermal conduction towards the substrate. From simulation, it has been found that 1.2 μm of this material is sufficient [Cuadrado *et al.*, 2013a]. At the same time, this layer can be dimensioned to constructively enhance the absorption of the resonant element placed above the coating. Figure 3.3 shows the periodic behavior of the electromagnetic absorption at the resonant element (a dipole) caused by the interference produced within the insulating

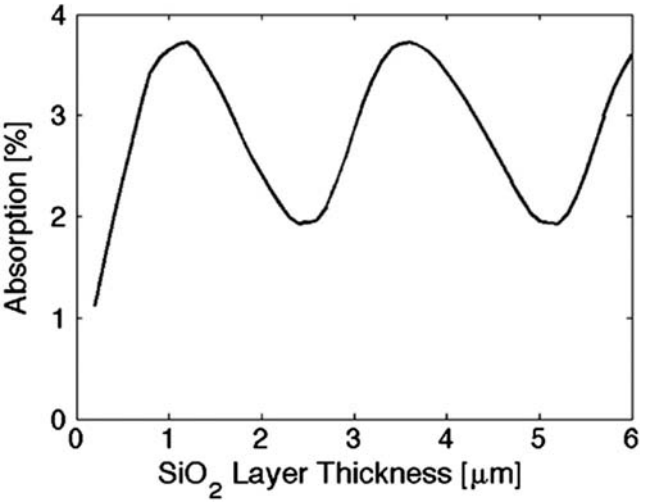

Figure 3.3 The absorption of the resonant structure (a dipole on a SiO_2/Si) substrate depends periodically on the thickness of the insulating SiO_2 layer. For an incident wavelength of $\lambda_0 = 10.6\,\mu m$, the first maximum occurs around $\lambda = 1.2\,\mu m$, where the thermal leakage towards the Si substrate reaches an asymptotic value (adapted from [Cuadrado *et al.*, 2013a] and reproduced with permission of SPIE).

layer, as a function of the thickness of this layer for a design wavelength of $\lambda_0 = 10.6\,\mu m$. Taking into account thermal and optical properties, it is possible to optimally adjust the thickness of this layer.

When working with antenna-coupled detectors on a substrate, it is also important to take into account the direction light is coming from in the final operating device [Bean *et al.*, 2010]. The antenna is usually located at the interface between two media: the substrate and the superstrate (typically air). So, light incidence may take two different configurations: from the substrate and from the superstrate. The ratio of power delivered (or detected) by an antenna for these two possible incidence situations is given as [Brewitt-Taylor *et al.*, 1981] [Rutledge & Muha, 1982]

$$\Gamma = \frac{\Phi_1}{\Phi_2} \approx \left(\frac{\epsilon_1}{\epsilon_2}\right)^{3/2} = \left(\frac{n_1}{n_2}\right)^3, \tag{3.3}$$

where Φ_1 and Φ_2 are the powers when the incidence is coming from medium 1 and 2, respectively, ϵ denotes the electric permittivity, and n is the index of refraction. Since the materials surrounding the antenna are dielectric, all of these variables are real valued. From Eq. (3.3) and for a typical case of air and Si substrate, this ratio should be around $\times 35$, meaning one order of magnitude better response when radiation is incident from the substrate compared to from the air. If the antenna were emitting, this would also correspond to a larger radiation on the substrate side. This first approach would indicate a

much better illumination layout from the substrate side. However, this approach is not always possible because of unwanted absorption bands in the substrate, or the presence of metallic layers at the bottom of the design that prevent illumination from the substrate [Codreanu & Boreman, 2002a]. In this case, the presence of insulating layers also increases the thermal impedance of the antenna, and produces a large response and a shift of the resonance. This is especially important in bolometers, where better thermal isolation retains the dissipated energy at the bolometer location. The shift in resonance frequency is caused by the decrease in capacitance when increasing the thickness of the insulating layer, and by the fringing effect, which affects the electrical size of the resonant element [Codreanu & Boreman, 2002a]. Additionally, some experimental results from actual devices written on coated wafers show strong antenna response when radiation is incident from the air side [Alda *et al.*, 2000]. Figure 3.4 shows the responses of antenna-coupled bolometers with a long dipole design. These devices respond better from the substrate side, but the enhancement factor is around $\times 1.20$, a value much lower than that predicted from the model. The reasons behind this discrepancy are the existence of various material interfaces in the structure that reflect light away from the antenna as well as the tight focus used in those measurements that includes some angular spectrum contributions at large angles, which are primarily reflected at the interface.

When using a special hemispherical immersion lens to measure the angular pattern of an antenna-coupled detector in the infrared, some of the previous limitations of measurements are removed and the air–substrate efficiency comparison becomes closer to the theoretical prediction. Figure 3.5 shows the angular pattern of a dipole antenna for different incidence planes. It also compares the responses for air-side illumination and substrate-side illumination. In this case, air-side illumination provides a clearly lower response than illumination through the Si lens [Lail *et al.*, 2009].

An experimental and theoretical study was conducted to investigate the limits of increased antenna response when illuminating through a high-index material [Lail *et al.*, 2009]. Antennas were fabricated directly on the flat side of a Si hemispherical lens. This configuration avoided excitation of substrate modes that are common with slab substrates. The increase in response seen depends on the $f/\#$ of the radiation that illuminates the antenna because of the angular response characteristics of the antenna. The best experimental results obtained in that study were a response multiplication factor in the range of $\times 5$ to $\times 7$, using a single-layer anti-reflection coating and $f/1$ illumination.

The thermal properties of materials are of great importance when considering transduction mechanisms involving a change in the temperature of the transducer, as happens with thermoelectric and bolometric transducers. The voltage responsivity for a bolometer is given as

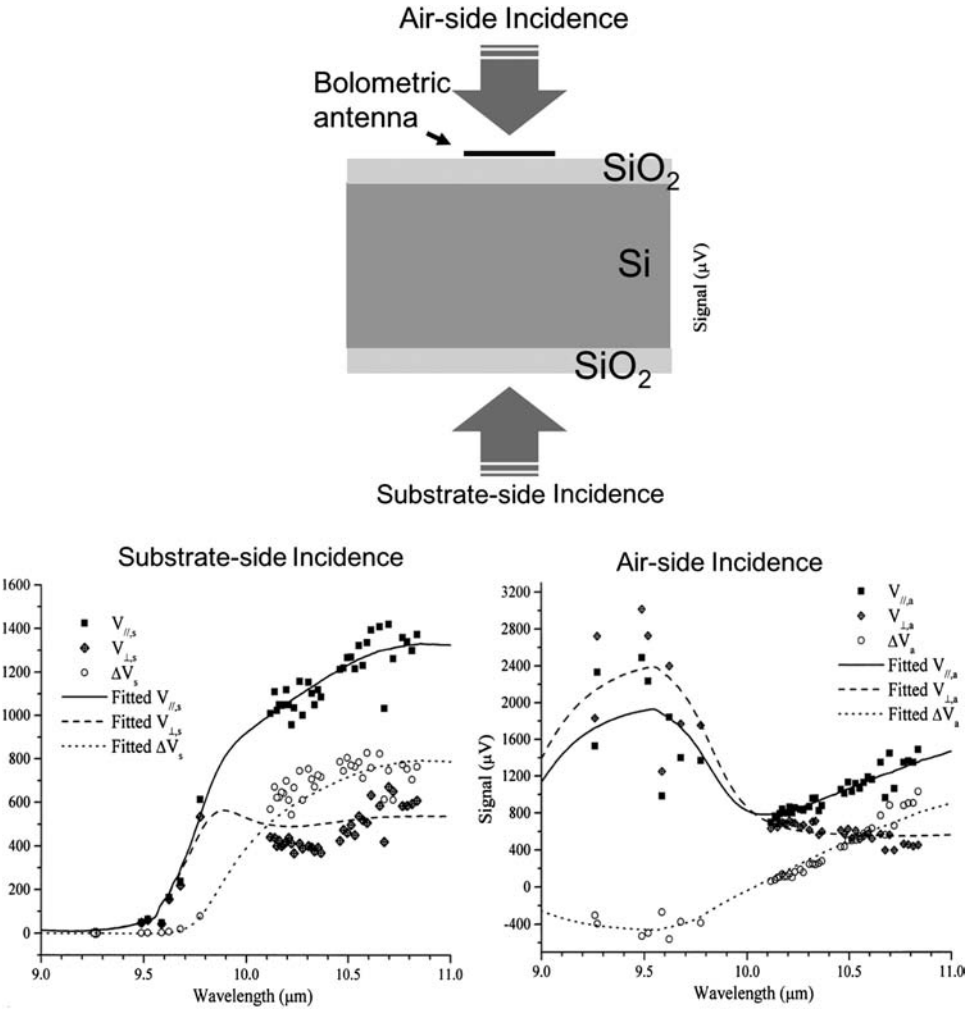

Figure 3.4 Air-side and substrate-side incidence produce different results when measuring the signal provided by a Nb microbolometer coupled to a dipole antenna made of Al on a Si wafer 380 μm-thick coated with 1.5 μm of SiO_2 insulation layer. The strong absorption of SiO_2 below $\lambda = 9.7$ μm clearly defines two behaviors where air- or substrate-side incidences are distinguished (adapted from [Alda *et al.*, 2000] and reproduced with permission of Elsevier).

$$\mathcal{R}_V = \alpha Z_{\text{therm}} V_{\text{bias}}, \tag{3.4}$$

where α is the temperature coefficient of resistance, V_{bias} denotes the bias voltage applied to the bolometer, and Z_{therm} is the thermal impedance describing the heat flow from the bolometer [González *et al.*, 2000] [González *et al.*, 2004a]. This thermal impedance is strongly dependent on the thermal material characteristics of the substrate and the structures, including antenna arms and lead lines. The equation that describes this thermal impedance is

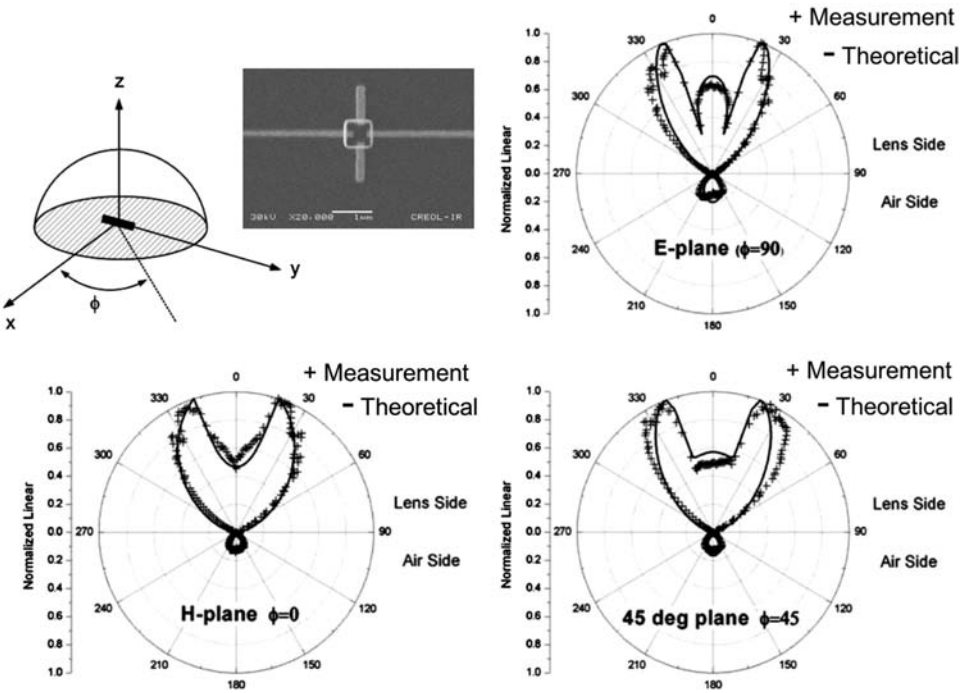

Figure 3.5 Angular pattern for the *E*-plane, *H*-plane, and 45° plane for dipole antennas coupled to Nb microbolometers. The antenna is fabricated on the flat surface of a hemispherical immersion lens made of Si. The dipole is oriented along the *Y* axis (adapted from [Lail *et al.*, 2009] and reproduced with permission of Elsevier).

$$Z_{\text{therm}} = \frac{R_{\text{therm}}}{\sqrt{1 + \omega_{\text{mod}}^2 R_{\text{therm}}^2 C_{\text{therm}}^2}}, \tag{3.5}$$

where ω_{mod} is the modulation frequency of the input optical signal, and R_{therm} and C_{therm} are the thermal resistivity and thermal capacitance, respectively. These two parameters are related by a thermal time constant as $\tau_{\text{therm}} = R_{\text{therm}} C_{\text{therm}}$. The main conclusion of this model is that a higher response will be obtained when the thermal impedance increases. However, this enhanced signal will show a longer time constant, and the device will be slower to respond [González *et al.*, 2005]. Figure 3.6 shows an experimental comparison of the signal obtained from a collection of infrared antennas coupled to microbolometers and fabricated on two types of coatings on a Si wafer: one coating is a 200 nm-thick thermally grown SiO_2, and the other is a 700 nm-thick spun aerogel. Aerogel is considered one of the best isolating stand-off layers from the thermal point of view. The results show a slower response from the aerogel devices, which also produced a response 30 times larger than that of those fabricated on the SiO_2 layer.

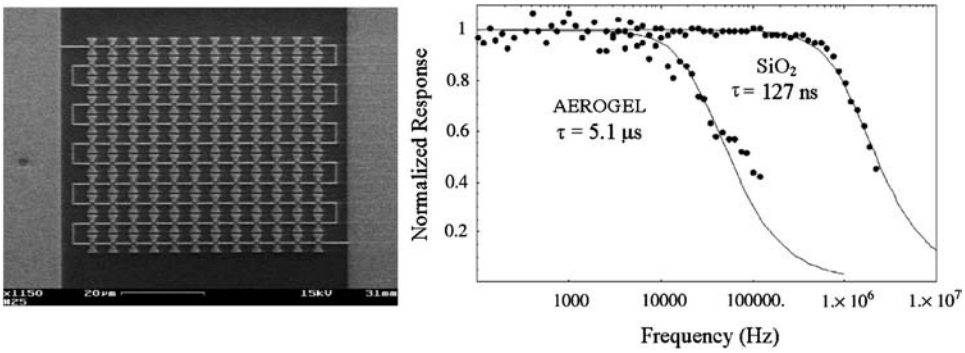

Figure 3.6 An array of 11×12 bow-tie gold antennas coupled to Nb microbolometers written on two substrates coated with two types of insulating layers: SiO_2 and aerogel. Those devices fabricated on aerogel present a slower response than those fabricated on SiO_2, with time constants, $\tau_{therm,Aerogel} = 5.1$ μs, and $\tau_{therm,SiO_2} = 127$ ns, respectively (adapted from [González *et al.*, 2004a] and reproduced with permission of Elsevier).

3.1.2 Material characterization

When considering fabrication at the nanoscale, it is important to note that material characteristics can be strongly affected by the nanofabrication tools used in the manufacture of devices. Furthermore, electromagnetic dimensional parameters, such as the penetration depth, are comparable in magnitude to the actual thickness of fabricated elements. Therefore, any deviation of the design geometric parameters will affect the actual performance of fabricated elements.

In these cases, the experimental characterization of materials being used to fabricate a given device should be taken as compulsory when refining the results of modeling and simulation. One of the most important parameters is probably the complex index of refraction, $\tilde{n}$. This optical constant can be measured by placing a sample of the material deposited with the same technique and method that will be used for the fabrication of the actual devices. Spectroscopic ellipsometry is likely the best technique for such a measurement, and the obtained results can be directly included within the computational electromagnetism packages used for simulation of the fabricated devices [Ginn *et al.*, 2007a]. Some discrepancies between the results obtained from spectroscopic ellipsometry and reference values in the literature have been observed [Folks *et al.*, 2008] [González *et al.*, 2009]. These discrepancies are within a 10% range and are likely due to the specific deposition techniques used to prepare the samples. Although in the visible spectrum the dispersive character is of great importance, some computational analyses where the spectral response of dipole and bow-tie antennas are studied in the infrared show acceptable results within a limited spectral range when only a constant value for $\tilde{n}$ is used [González *et al.*, 2009].

Additionally, the actual geometry of the devices can differ from the designed geometry. To properly determine the fabricated parameters, a scanning electron microscope photograph should be taken, and the geometric parameters that are actually fabricated should be compared with the design specification. Again, those discrepancies should be considered in a final refinement of simulations.

3.2 Classical Designs

Antenna design in the radioelectric range is full of geometries adapted to enhance performance in a variety of situations. When moving to the infrared we need to cope with some constraints and conditions that alter the design and capabilities of the proposed geometries. In section 2.1 we have seen how material characteristics are an important issue that affects scaling, through the concept of effective wavelength, recognizing ohmic losses and the interaction of light with the whole structure of the resonant element. Additionally, fabrication of nanoantennas typically limits the design to two-dimensional (2D) layouts where the antenna is placed on, or embedded in, dielectric materials.

However, some very common and successful designs that work in the radioelectric regime have been translated to the optical range. This is the case for dipoles, bow-ties, spirals, and patch antennas.

The dipole antenna is probably the simplest case of a working antenna. Its treatment provides analytical solutions in idealized cases [Balanis, 2005]. A dipole antenna is strongly dependent on the polarization state of the incident electric field. Because of that characteristic, it served to prove the capabilities of this technology when optical antennas were first being developed. The analysis of its dependence on length provided a clear understanding of the resonant modes of a given infrared antenna with a dipole design [Fumeaux *et al.*, 2000]. Then, the dipole antenna allowed the splitting of the thermal non-selective response and the electromagnetic, antenna-like selective response in polarization [Alda *et al.*, 1999] [Fumeaux *et al.*, 1999a]. Bow-tie antennas are also polarization-selective devices that produce a larger signal than dipole antennas because of the larger metal region exposed to the incoming radiation and larger spectral bandwidth. Both dipole and bow-tie antennas respond very selectively to linear polarization. Some other designs, such as spirals [Boreman *et al.*, 1996] [Fumeaux *et al.*, 1997], respond better to circular polarization adapted to the helicity of the design: right-handed circular polarization (RCP) or left-handed circular polarization (LCP) [Cuadrado *et al.*, 2014a]. Figure 3.7 shows this dependence for four antenna designs: dipole, bow-tie, square spiral, and log-periodic. This polarization sensitivity is an added value that is intrinsically given by the interaction mechanism of the resonant structures

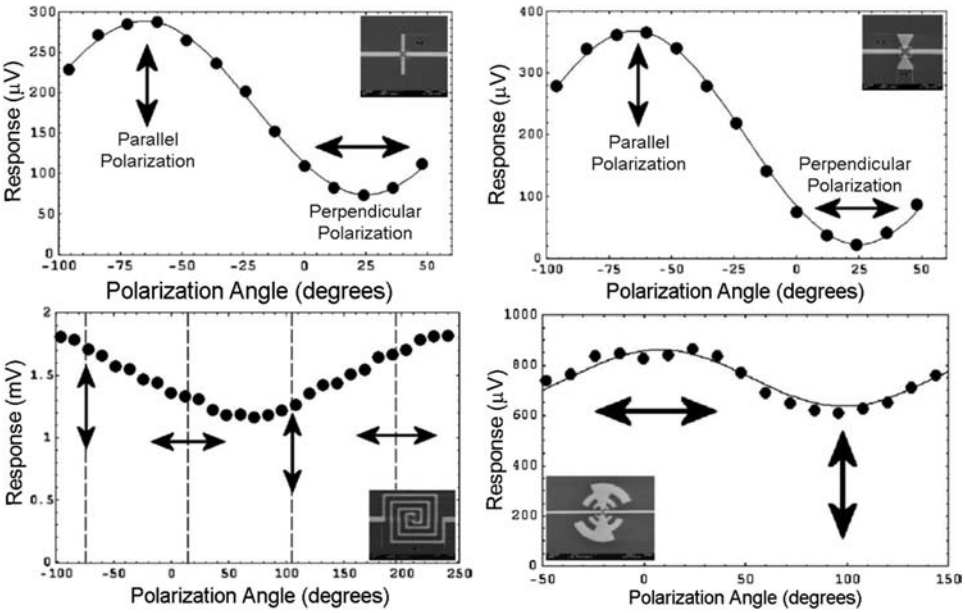

Figure 3.7 Response of dipole, bow-tie, square spiral, and log-periodic designs as a function of the orientation of a linearly polarized incoming wave (adapted from [González & Boreman, 2005] and reproduced with permission of Elsevier).

with light [Boreman *et al.*, 1998]. An appropriate use of this selectivity may give rise to polarization-selective pixels made of a proper combination of antenna-coupled detectors [Krenz *et al.*, 2008] [González *et al.*, 2002] [Simon & González, 2011] [Cuadrado *et al.*, 2014a]. Polarization-dependent focal plane arrays have been demonstrated using log-periodic antennas for IR imaging applications [González *et al.*, 2006] (see Fig. 3.8).

However, some applications, such as energy harvesting or thermal imaging, require no polarization selectivity and need designs that resonate with any polarization state. This is possible by combining dipoles in a star-like design. Figure 3.9 shows a design where the antenna elements are designed not to be polarization dependent, and to respond to different wavelengths within the infrared region [Boreman *et al.*, 2006]. A multiwavelength design can also be obtained by using fractal geometries [Volpe *et al.*, 2011] [Gottheim *et al.*, 2015] [Cuadrado *et al.*, 2015a], mimicking the case already proposed at lower frequencies as variations of the Sierpinski triangle [Puente-Baliarda *et al.*, 1998]. Some of these classical designs can be adapted to have tunability features [Codreanu, 2001]. One way to accomplish this feature is by electrically modifying the geometry of the device [Gritz, 2003] [Gritz *et al.*, 2004]. This can be done, for example, by placing the antenna as an air bridge suspended on a central electrode. The design will work as a capacitor, where one of the plates is movable [Gritz *et al.*, 2003a] [Gritz *et al.*, 2005].

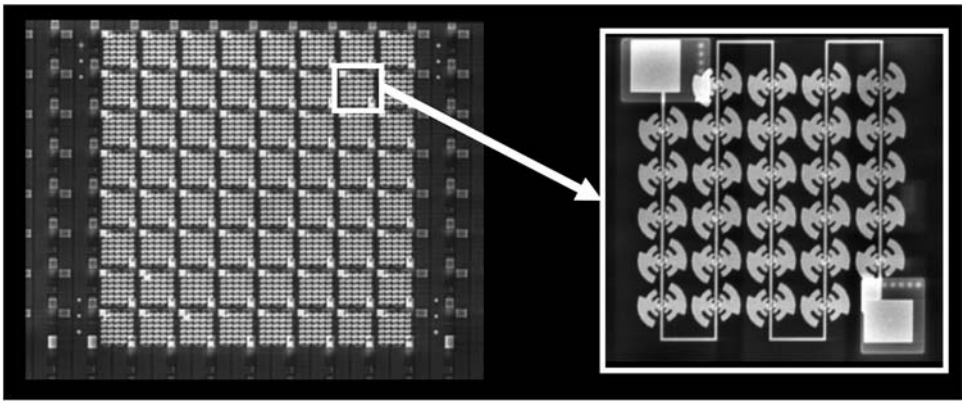

Figure 3.8 An 8×8 pixel focal plane array (left) of infrared antennas coupled to commercial read-out integrated circuits. The signal from each pixel is generated by 28 log-periodic antennas (right) connected in series (adapted from [González *et al.*, 2006] and reproduced with permission of Wiley).

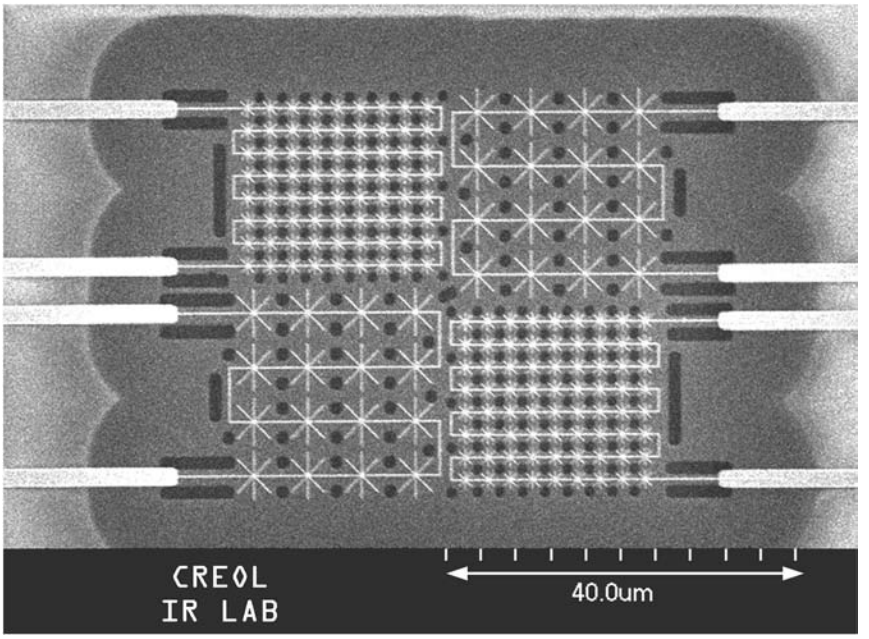

Figure 3.9 A collection of star-like antennas connected in series is able to generate signals independent of polarization for two different wavelengths [Boreman *et al.*, 2006].

3.2.1 Slot antennas

Another possibility in optical antenna design is the use of slot antennas made on a metallic layer. A very simple way to see how slots work from a resonance point of view is by interchanging the roles of the magnetic and electric fields.

Then, a dipole antenna selectively responds to an electric field aligned along the length of the dipole. Its slot counterpart will resonate with a magnetic field aligned along the length of the slot. Figure 3.10 shows this fact in terms of the near-field distribution of the magnetic and electric fields. This behavior needs to be considered when combining antennas having complementary geometries.

An interesting application of the previous characteristic has been demonstrated in dual-band detection for millimeter waves and IR radiation. Figure 3.11 shows a device that combines a slot antenna having a dipole-like geometry sized to resonate in the millimeter-wave band at 92.5 GHz, and a

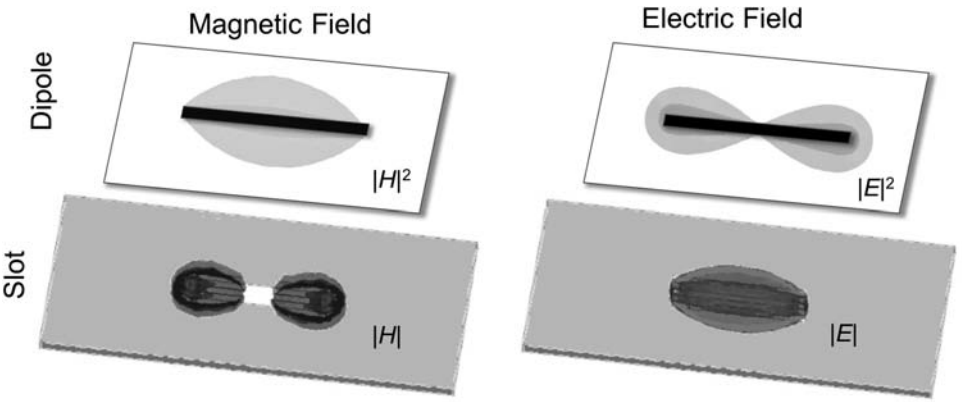

Figure 3.10 Maps of the electric and magnetic fields are complementary to each other when comparing the dipole response to the slot response having the same dimensions (adapted from [Cuadrado, 2014]).

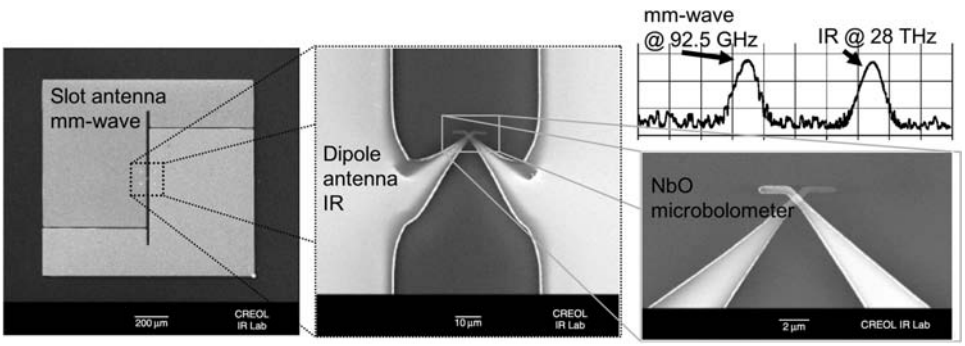

Figure 3.11 A combination of a slot and a dipole antenna used for the simultaneous dual-band detection of millimeter waves and IR signals. The device is made of Ni and includes a NiO layer that forms a MOM diode at the center of the dipole and slot geometries. The spectrum analyzer trace above the IR dipole shows the simultaneous detection of both signals when two different modulation frequencies are applied to the IR and the millimeter-wave radiations (adapted from [Abdel-Rahman *et al.*, 2004] and reproduced with permission of the Institution of Engineering & Technology).

dipole antenna tuned at 28 THz in the infrared [Abdel-Rahman *et al.*, 2004] [Abdel-Rahman *et al.*, 2005b] [Abdel-Rahman *et al.*, 2005a]. Both elements are oriented to selectively receive radiation having the proper orientation of the electric field. The signal is transduced by a metal-oxide-metal tunnel diode placed at the center of the slot and at the feed point of the dipole.

Slot antennas can be arranged to perform other tasks, such as making the transition between free-propagating radiation and wave confinement in a coplanar strip waveguide. This is the case of tapered slot antennas [Florence, 2012] [Florence *et al.*, 2011] [Florence *et al.*, 2012], which, when properly arranged, can collect radiation and redirect it into the waveguide maintaining the field amplitudes. Figure 3.12 shows experimental near-field data obtained when infrared radiation incides with an angle of incidence of 60° to the plane of the device at the wide end of the tapered slot.

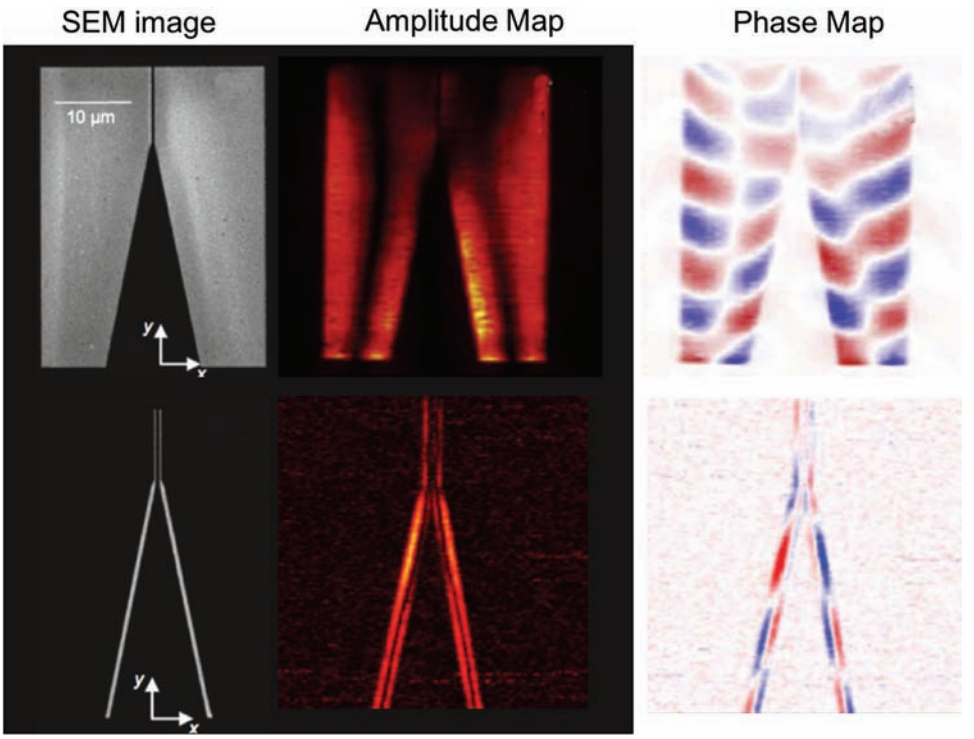

Figure 3.12 The use of slot antennas as couplers between free propagating waves and waveguides was demonstrated in two linear designs. One design resembles a conic horn (tapered slot antenna), and the other uses two slots that converge from the input to a metallic waveguide. The results are a good match with the electric field obtained from simulation. The experimental results were obtained by registering the scattered near field excited in the structure under oblique incidence conditions using scanning near-field optical microscopy (SNOM) techniques. This characterization method is presented in section 5.8 (adapted from [Florence *et al.*, 2012] and reproduced with permission of Elsevier).

3.2.2 Diffractive optical elements and antennas

Another interesting issue related to materials and auxiliary elements is the integration of optical elements in combination with optical antennas or resonant elements. We have seen how the thickness of the insulating layer may enhance the delivered signal through constructive interference. At the same time, the wafer thickness can be used to focus optical radiation on the antenna device. This can be accomplished by writing a Fresnel zone plate (FZP) on one of the sides of the wafer. The design and dimensions of this FZP are made to focus light on the antenna element located on the other side of the wafer. In this case, fabrication assures the alignment of the optics and the detector. When considering the fabrication and optimization of a FZP, it is interesting to explore not only the classical circular FZP design, but also some other square or polygonal designs that could be of interest to better adapt to fabrication constraints [Alda & Boreman, 2008] [Alda *et al.*, 2006a] [Alda & González, 2009b]. On the other hand, this combined design increases the collection area from the $\approx\lambda^2$ value to several hundreds of λ^2 [González *et al.*, 2005] [González *et al.*, 2004b]. Figure 3.13 shows a fabricated circular FZP aligned through the wafer with a square spiral antenna coupled to a Nb microbolometer. The diameter of the outer circle of the FZP is around 260 μm, and the FZP collects energy that impinges on an antenna device having a lateral dimension of around 5 μm.

A further step in the use of FZP is the transformation of this geometry into a working antenna device. This element combines two functions: the FZP focuses light through the substrate to the detector at the other side of the wafer, and at the same time, it generates a current distribution when excited by electromagnetic waves resonating on the arms of the FZP antenna. The

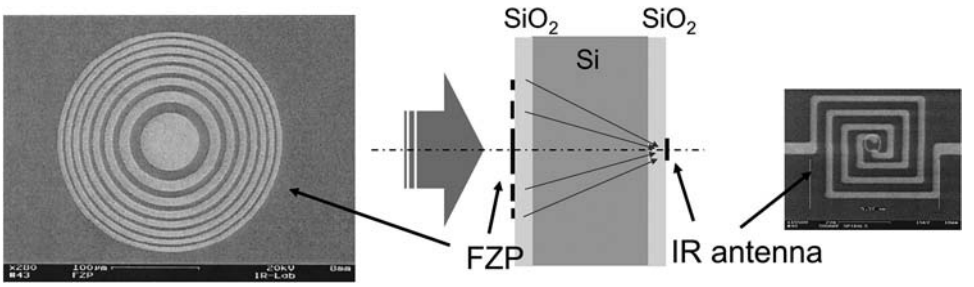

Figure 3.13 A Soret-type circular FZP is written on a Si substrate having a thickness of 380 μm and double-side coated with an insulating layer 200 nm-thick. Both the antenna and the FZP opaque zones are made of 100 nm-thick gold, and the antenna is coupled to a Nb bolometer deposited at the center of the square spiral having a size of 500×500 nm^2. The measured gain of this arrangement is around $\times 60$ when compared to similar devices without the FZP (adapted from [González *et al.*, 2004b] and reproduced with permission of OSA).

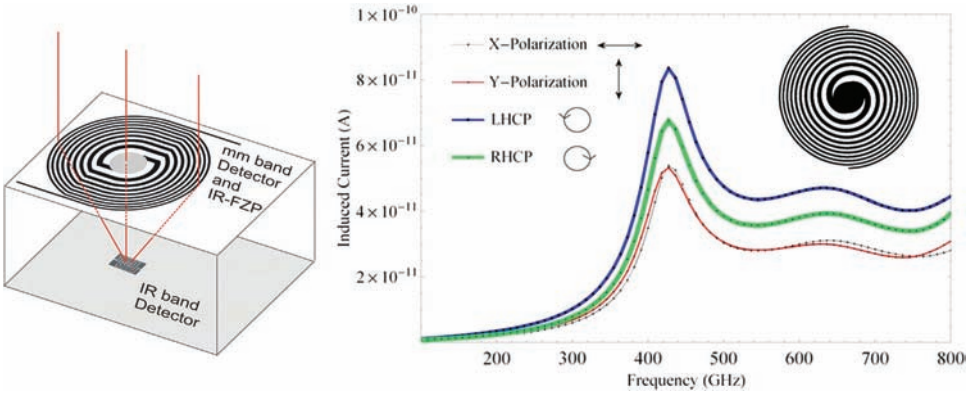

Figure 3.14 A spiral antenna can be arranged as a FZP that is able to focus light on the back of the wafer in which it is deposited. This arrangement serves as a dual-band detector that generates currents on the arms of the FZP antenna and focuses light on an IR detector that can be, as in [González *et al.*, 2004b], another IR antenna. This system can work as a millimeter or terahertz detector and an infrared detector. The main advantage of this arrangement is that both bands are aligned along the same optical axis (adapted from [Alda & González, 2009a] and reproduced with permission of OSA).

transformation is quite simple and results in a spiral antenna with arms of a size that follows the Fresnel zone arrangement. The mismatch between the size of the detector at the FZP plane and at its focal point makes the system suitable for dual-band detection. As can be seen in Fig. 3.14, the FZP antenna resonates at a frequency around 2 orders of magnitude lower than the infrared detector located at the opposite side of the wafer (450 GHz versus 30 THz). As in the previous case, alignment is ensured by fabrication tolerances, and signals coming from the infrared and millimeter band are routed separately on each side of the wafer. These designs combine the actual detection at two separate bandwidths in the same device, expanding the capabilites of millimeter- and terahertz-band detectors [Kazemi *et al.*, 2005] [Kazemi *et al.*, 2007b] [Kazemi *et al.*, 2007a].

3.3 Computational Electromagnetism. Methods and Approaches

Computational electromagnetism has a simple goal: solving Maxwell's equations for a wide variety of cases involving different media, different excitation, and different domains (frequency, time, or both simultaneously). Most commercial packages applicable to the optical range are extensions of well-proven tools in the development of radiofrequency and microwave designs. The equations are the same, but we have previously seen how some material characteristics change significantly when moving to higher

frequencies, and this fact, along with the meshing limitations associated with the smaller wavelength, needs special care in this transition to the optical range.

Currently, there is a large collection of computational electromagnetism programs that have been developed as multipurpose suites (multiphysics, CAD integration, etc.), or as stand-alone single-purpose applications. Universities and companies offer their products and packages under paid or freeware license, as proprietary or open codes, and working in a variety of platforms: from basic desktops to mainframe scientific computers and clusters. The choices are enough to satisfy the needs and resources available, both in price and computational power. In any case, all of the programs share an important characteristic that every beginner should know when using them: they always produce an output, whatever the input is. The user has to approve the quality of this output using knowledge, reasonable expectations, and the ultimate comparison to previous proven results or, even better, to experimental data. It should be remembered that a well-designed experiment always produces an actual result that includes the evaluation of experimental uncertainties.

In addition to the main objective of properly solving Maxwell's equations, some computational packages include other physical domains that are relevant for infrared antennas. For example, when considering bolometric or thermoelectric transduction, thermal behavior becomes as important as electromagnetism. Then, a correct simulation requires inclusion of thermal behavior in the calculation.

In this section we briefly describe some of the most common numerical methods used in the design of optical antennas and resonant structures. There are also many numerical methods in computational electromagnetism [Deslise, 2014]. Beyond hardware requirements, licensing, and price limitations, each method is specifically adapted to certain problems and characteristics. The methods presented here are not a complete list, and variations are sometimes wisely used to analyze scattering, energy budget, or other kinds of interaction of light and matter [Hafner, 1999] [Mittra, 2014]. Our goal is to show some the most commonly used numerical methods in the analysis of optical antennas and resonant structures [Rico-García, 2003].

3.3.1 Green's tensor methods

Basic electromagnetism uses Green's tensor, or Green's function, to obtain electromagnetic fields produced by dipoles located in a given spatial domain. Green's tensor can be seen as the propagating kernel of an integral equation that adds together all of the individual contributions of the dipole sources within the volume of the scattered source. Thus, in free space, Green's function is given by

$$G(\vec{r},\vec{r}') = \frac{\exp(ik\,|\,\vec{r}-\vec{r}'\,|)}{4\pi\,|\,\vec{r}-\vec{r}'\,|}, \tag{3.6}$$

where $\vec{r}$, and $\vec{r}'$ define the position where the field needs to be calculated and the position of the source, respectively, and k is the wavenumber. In a real case, Green's function takes the form of a 3×3 matrix, which is also technically denoted as a dyadic or Green's tensor. In a Cartesian 3D coordinate system, the columns of this tensor can be interpreted as the contributions to the electric field at position $\vec{r}$ of three dipoles, orthogonally oriented, representing point sources at the location $\vec{r}'$ within the volume of interest where the scattering object is placed [Martin & Piller, 1998] [Martin *et al.*, 1995].

Computational electromagnetism uses Green's function to solve the following equation for the electric field outside the source volume, produced by a collection of sources radiating from a volume domain:

$$\vec{E}(\vec{r}) = \vec{E}_{\text{inc}}(\vec{r}) + i\omega\mu\mu_0 \int_v \mathbf{G}(\vec{r},\vec{r}')\vec{j}(\vec{r}')dv', \tag{3.7}$$

where $\mathbf{G}(\vec{r},\vec{r}')$ can be seen as a matrix, or more technically, a dyadic structure. The success in solving this problem will depend on the convergence of this integral equation and the adequate selection of the functions representing currents $\vec{j}$, along with the selected coordinate system and volume boundaries.

3.3.2 Method of moments (MoM)

The method of moments expands the currents induced by the incident radiation in a resonant structure. The expansion uses different types of functions depending on the problem under consideration. They can take the form of a collection of modes applied over the entire calculation domain, or a set of functions adapted to the geometry of the resonant elements. From a fundamental point of view, this method obtains the scattered field as the contribution of a collection of currents, $\vec{j}_q$, that flow within the interaction volume, v:

$$\vec{E}_{\text{scatt},p}(\vec{r}) = K \int_v G(\vec{r},\vec{r}')_{p,q}\vec{j}_q dv, \tag{3.8}$$

where $G(\vec{r},\vec{r}')_{p,q}$ is the Green's function that relates the currents to the electric field, and K summarizes the constants and frequency dependence that do not vary within the integration volume. This method can be also expressed in matrix form: $[Z][I] = [V]$, which resembles Ohm's law. Actually, the success of the method in evaluating a valid solution relies on the capability of finding a suitable current base function, and the proper conditioning of the matrix problem [Harrington, 1967].

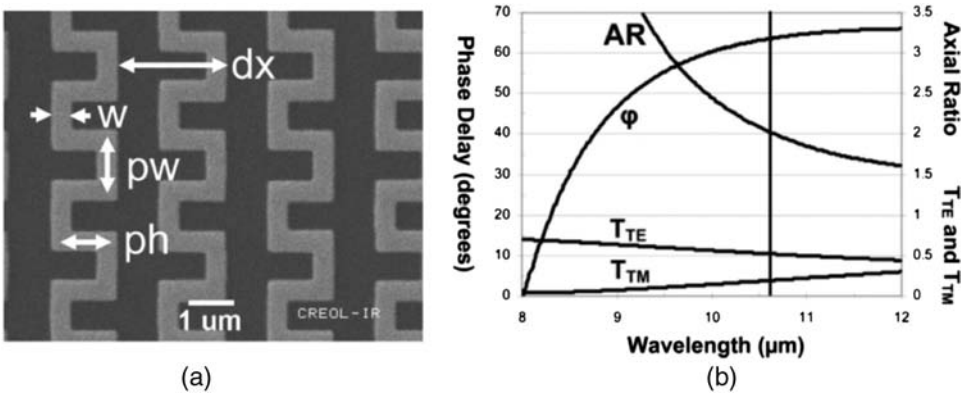

Figure 3.15 (a) Because of its geometry, a meander-line structure in the IR is used as a retarder plate. Its analysis can be done by using periodic method of moments, which evaluates the currents built up along the repetitive structure. (b) The axial ratio of the polarization ellipse and phase retardance between TE and TM components for a given design (adapted from [Tharp *et al.*, 2006b] and reproduced with permission of OSA).

A variation of the method of moments applicable to periodic structures is the periodic method of moments (PMM) [Munk, 2000]. This numerical strategy is very well suited to treat problems involving repetitive cells along 2D structures. Figure 3.15 shows the results of the application of the method of moments when simulating the polarization characteristics of meander-line structures in the infrared.

3.3.3 Multiple multipole (MMP) method

While the method of moments is based on current distributions, the multiple multipole method uses a collection of sources that can be monopolar, dipolar, or multipolar in nature. These elements are typically located near the interface between two media (in a scattering problem, one of them is the scattering object and the other is the surrounding media). Mathematically, this expansion can be given as

$$\vec{E}(D_i) = \vec{E}_{\text{inc}}(D_i) + \sum_{j=1}^{N} \alpha_k(D_i)\vec{e}_k, \tag{3.9}$$

where D_i represents the domain where the calculation is made, and $\vec{e}_k$ are the multipolar functions defined in the problem. These multipole functions can be analytical solutions of Maxwell's equations and are locally defined around the source of the multipole. The MMP method fixes the boundary condition based on the multipole selection. This selection is adapted to the geometric and material characteristics of the problem and is organized across the boundary limits of the domains under consideration [Moreno *et al.*, 2002].

3.3.4 Transmission line matrix (TLM) method

The TLM approach uses electrical-engineering nomenclature where the propagation problem is framed using voltages, currents, impedances, and transmission lines [Johns & Beurle, 1971] [Hoefer, 1985] [Russer & Russer, 2012]. It works in the time domain by discretizing the space domain into nodes connected through transmission lines that carry information about the electromagnetic field propagating within the volume of interest. In a 2D Cartesian system, each node is connected by 4 transmission lines to its neighbor nodes (in 3D this number is 6). These transmission lines are used to receive or scatter/emit radiation. A graphical representation of these transmission lines is given in Fig. 3.16. As far as this radiation can be modeled using voltages related to the electric field and currents related to the magnetic field, the analysis is transformed to an equivalent circuit, where impedances of the transmission lines between nodes are linked to the electric properties of the material in which the wave is propagating. In the simplest case, this will be the wave impedance $Z = \sqrt{\frac{\mu_0 \mu_r}{\varepsilon_0 \varepsilon_r}}$ (see section 2.2). The situation at a given time evolves by propagating voltages along the transmission lines with a time period adjusted to reach the neighboring nodes. This constraint is applicable to any time domain method and links both spatial, Δl, and temporal, Δt, discretizations using the speed of the electromagnetic wave: $\Delta l = c\Delta t$.

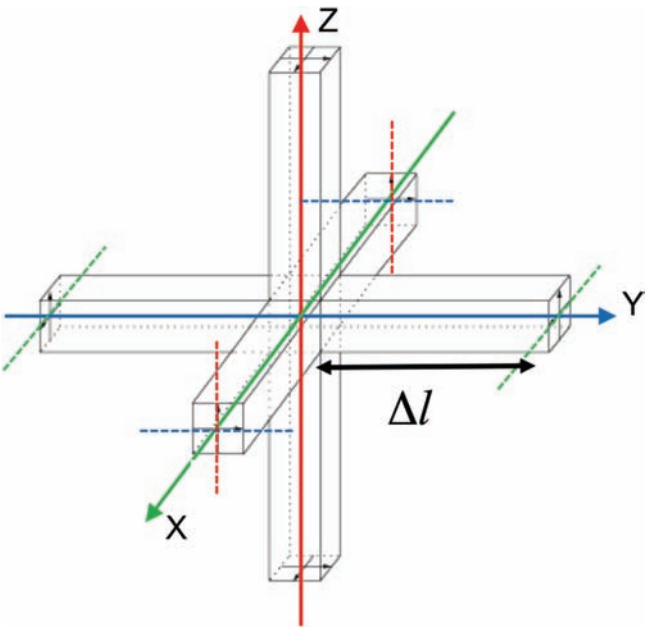

Figure 3.16 Voltages propagate through a transmission line connecting neighbors along a 3D cubic mesh.

3.3.5 Finite differences in the time domain (FDTD) method

The FDTD method probably produces the most intuitive results because it tracks the temporal evolution of the electromagnetic fields over a given volume. This is done by discretizing the region of interest with a meshing able to faithfully represent the geometry and materials under study.

As with any finite difference method, FDTD is strongly dependent on the meshing density and adaptation of the mesh to the actual geometries. At the same time, FDTD is also a method requiring a large amount of memory allocation to store the values of the electromagnetic fields on the given mesh. The method, once restricted to large computer systems, has become more generally available as the computer industry has provided desktop systems able to manage large amounts of memory. Furthermore, this method can exploit parallelization strategies to evaluate larger meshing volumes and finer meshing.

At the same time, FDTD algorithms are easy to compute and are applicable to a variety of materials, including nonlinear, anisotropic, or dispersive. The method is explicit in the sense that no matrix inversion algorithm is necessary (as happens, for example with the MoM), and the results in temporal step $n+1$ only depend on the solution for step n. Figure 3.17 shows the modulus and phase of a hexapolar mode excited in a photonic crystal cavity. These results have been obtained from a FDTD script written in C++ and executed on a regular desktop PC [Rico-Garcia *et al.*, 2004] [Rico-Garcia *et al.*, 2005].

At the core of the FDTD method is the so-called Yee algorithm, which evaluates the finite differences along three spatial dimensions and time [Yee, 1966]. The Yee method uses differences centered at each point of the mesh to discretize Maxwell's rotational equations (Faraday's law and the Ampere–Maxwell law). A full coverage of the foundations of the method and its

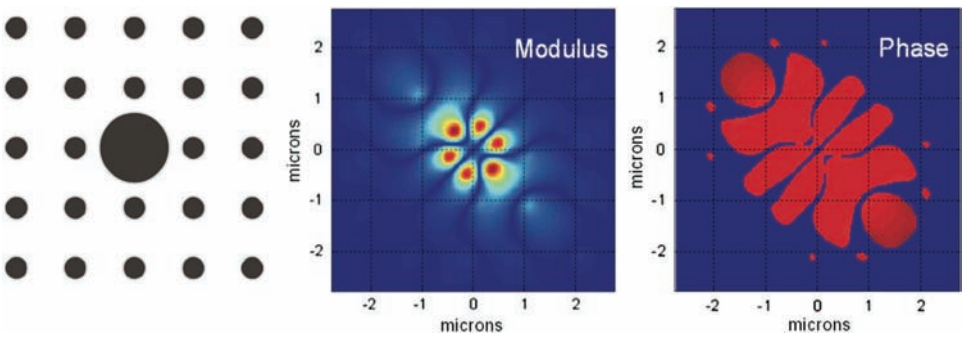

Figure 3.17 The photonic crystal cavity made of GaAs cylinders arranged in a rectangular array can be analyzed by a FDTD algorithm to obtain the modulus and the phase of the cavity modes (adapted from [López-Alonso *et al.*, 2004] and reproduced with permission of OSA).

successive extensions is given, for example, in the Taflove books [Taflove & Hagness, 2005] [Taflove *et al.*, 2013]. The results given by this method can be analyzed in more depth by applying multivariate techniques, such as principal component analysis, that provide better insight into the link between spatial-temporal and spectral characteristics of the results [López-Alonso *et al.*, 2004], including the effect of fabrication tolerances [Rico-García *et al.*, 2005].

3.3.6 Finite element method (FEM)

Finite element methods have been applied to a variety of areas where a set of coupled partial differential equations are solved on a given volume of interest [Volakis *et al.*, 1998] [Jin, 2014]. Mechanics, thermal analysis, and electromagnetism are some of the most successful areas.

FEM and FDTD methods share the necessity of very precise and adaptive meshing, and therefore these methods are memory-intensive. Typical FEM algorithms in electromagnetism are devoted to the steady state solution, where time is no longer an issue and the frequency dependence becomes explicit. FEM solves the partial differential equation associated with electromagnetism. In some cases, Maxwell's four equations are combined to produce differential equations using potentials. These are the magnetic vector potential, $\vec{A}$, and the scalar electric potential, V, defined as

$$\vec{B} = \nabla \times \vec{A}, \tag{3.10}$$

$$\vec{E} = -\nabla V. \tag{3.11}$$

These potentials obey some other relations, such as the Coulomb gauge condition, that make them suitable for use in electromagnetism problems [Jackson, 1998].

From a numerical point of view, the solution of the corresponding partial derivatives across the volume of interest is given as a combination of basis functions. These basis functions are adapted to the geometry (mesh) and the problem under analysis to produce a reliable solution. On the other hand, an optimization approach is added to take into account the physical realization of the problem. In the case of computational electromagnetism, one of the usual optimization conditions is the minimization of the total energy integrated over the volume of the meshed cell.

In the design of antennas and resonant structures, FEM algorithms have been successfully applied to the analysis of reflectarrays (see Fig. 3.18.a) and to the mutual validation of scattering scanning near-field optical microscopy (s-SNOM) measurements (see Fig. 3.18.b). An interesting property of FEM is its capability to analyze different multiphysics problems using the same geometry but changing the set of differential equations. This fact also makes possible the interaction between domains to produce results in cases where a

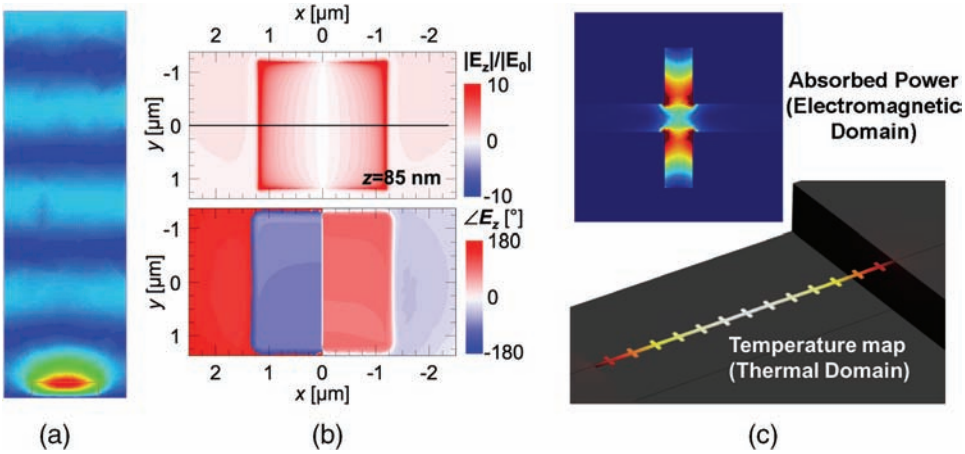

Figure 3.18 Results from FEM packages. (a) The electric field distribution (modulus) of a plane wave interacting with a square metallic patch on a dielectric stand-off layer. (b) The amplitude and phase of the E_z component calculated for its comparison with s-SNOM measurements on resonant structures. (c) Combining the results from the electromagnetic domain and the thermal domain, it is possible to obtain the temperature map of an array of dipole antennas working as a NOEMS device (adapted from [Ginn, 2009], [Ravichandran *et al.*, 2013], and [Cuadrado, 2014], and reproduced with permission of SPIE).

variety of phenomena occur simultaneously, as happens for example with the combination of thermal and electromagnetic domains used in the simulation of thermoelectric antenna-coupled devices (see section 6.1.3). In Fig. 3.18.c we show the combined results obtained from the electromagnetic domain in terms of the absorbed power by a dipole antenna. This antenna is arranged as a linear array in a nano-opto-electro-mechanical system (NOEMS) device, where its mechanical oscillations depend on the temperature map of the device.

3.3.7 Material considerations and computational implementation

The experience we accumulated in the design, fabrication, and testing of optical antennas and resonant elements has made us pay special attention to a very fundamental issue related to the final reliability of the simulated results — the accurate characterization of materials.

Most of the computational electromagnetic methods rely on published results for the value of the physical constants involved in each domain. From an optical point of view, these constants are the dielectric permittivity, magnetic permeability, and conductivity. If some models are applicable (for example the Drude model), it is possible to obtain resistivity, index of refraction, or penetration depth. If the system is nonlinear, electric and magnetic susceptibilities should be provided accordingly. Also, when mechanical or thermal domains are included, density, thermal coefficient of

resistance, thermal coefficient of expansion, etc., should be part of the set of physical constants involved in the calculation. Typically, handbooks are used to obtain the necessary values [Palik, 1997] [Lide, 1995] [Yang *et al.*, 2015]. These material data are constantly revised, and new materials and conditions are reported in applicable journal papers. The choice of the source of the material database becomes an important issue when considering the reliability and quality of the computational results.

As a matter of fact, material characterization in micro- and nanotechnology is a significant issue related to the change of material properties when moving to the nanoscale. Tabulated bulk material properties should not be fully trusted, and a dedicated revision of those parameters is sometimes necessary. Furthermore, when considering fabricated devices and nanostructures, the method for deposition or evaporation may become relevant to the actual values of the material properties. To solve this problem, it is highly advisable to check the feasibility of the material characteristics with measurement techniques applicable to the materials and structures actually fabricated. Spectroscopic ellipsometry in the visible and the infrared is a valuable technique to validate the optical properties of materials and structures. Figure 3.19.a shows the setup of an infrared ellipsometer used for material characterization of metals and dielectrics used in fabrication of optical antennas. In Fig. 3.19.b we can see how the implementation of the optical material properties actually measured with an infrared ellipsometer improves the fitting of the experimental data with the results obtained from the simulations (in this case using a method-of-moments algorithm) [Ginn *et al.*, 2007a].

3.4 Multiphysics Approach

In resonant structures where the incident optical field builds up currents and generates an antenna-like interaction, the structure is not an ideal entity suspended in an ideal vacuum volume. These structures are associated with a substrate, a surrounding element, and, when producing a measurable external signal, a transduction mechanism (see section 6.1).

Computational electromagnetism packages are able to model some interactions between physical domains. FDTD methods model dispersive and dissipative materials and accurately predict the effects of them. FEM algorithms solve these situations, providing connections with other physical domains: mechanical and thermal domains, which are useful in determining the behavior of NOEMS and thermal transduction (bolometers and thermopiles).

However, using computational tools requiring fine meshing of large volumes is not always the best approach to understand the effect and role of the underlying physics. The need for properly combined, convoluted

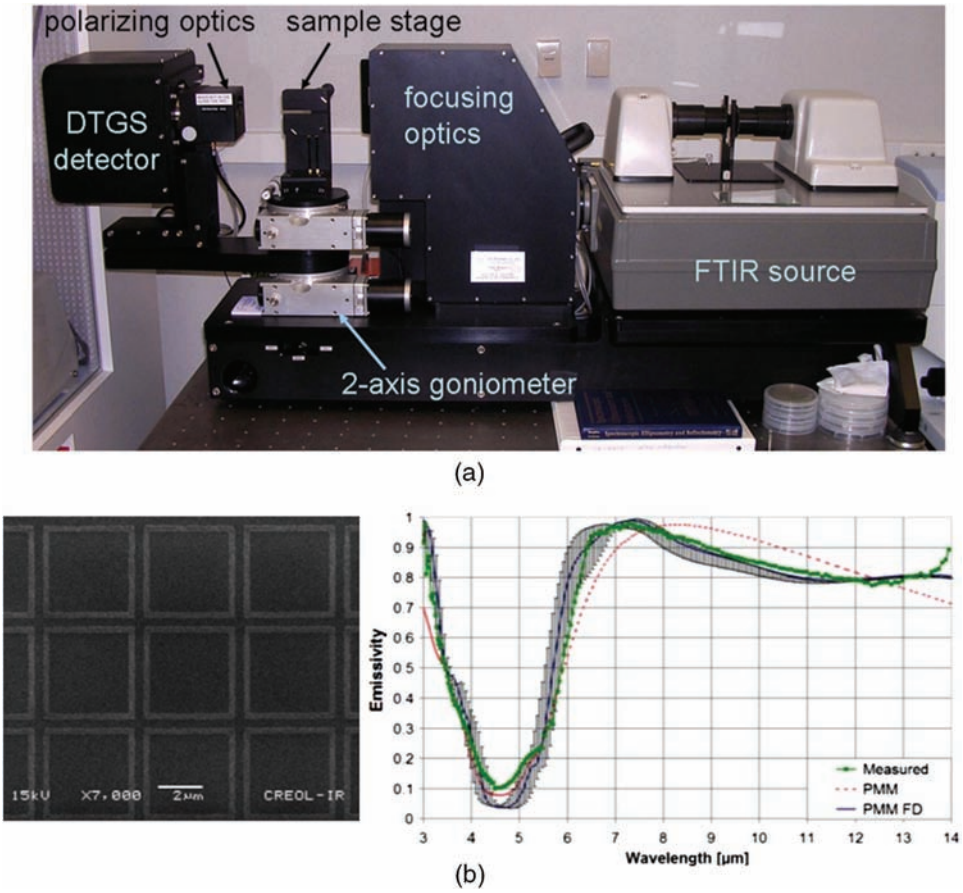

Figure 3.19 (a) Photograph of an infrared variable-angle spectroscopic ellipsometer used for material characterization in the infrared (DTGS is deuterated triglycine sulfate; FTIR is Fourier transform infrared). (b) Experimental data obtained from an IR spectrometer of the emissivity of Mn square loops on a ZrO_2 stand-off layer on a gold ground plane more closely match the simulated data when material properties are incorporated into the computational electromagnetism algorithm (method of moments) (adapted from [Ginn *et al.*, 2007a] and reproduced with permission of ACES).

boundary conditions, or the existence of variable meshing strategies, may obscure the meaning of the results and therefore the derived conclusion.

In such cases, different physics may need different approaches. An example of this case is the modeling of diode transducers, where the diode itself is modeled as a lumped element with the appropriate parameters, typically the complex impedance. This device model is inserted into the allocated position having incoming voltage or current values that drive the diode. This approach allows a better understanding of the different elements of the optical nanocircuit and makes possible a simpler calculation of characteristic parameters, for example, the efficiency of the element [Briones *et al.*, 2013].

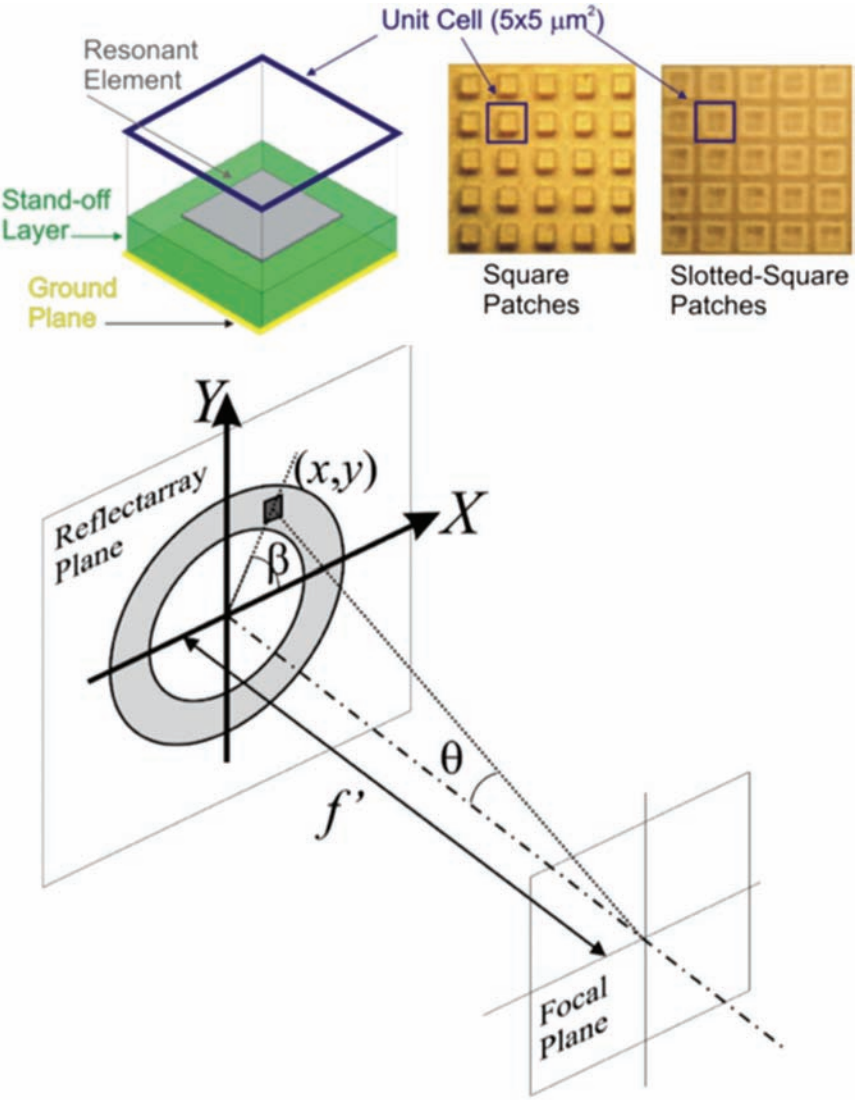

Figure 3.20 A reflectarray composed of a Fresnel zone arrangement of unit-cell elements. These individual elements, adapted to different predetermined phase shifts, are successfully modeled using a FEM package. The resulting phase shift is arranged as a phase window to calculate the performance of the system using propagation kernels to compute the amplitude distribution at the plane of interest (adapted from [Ginn *et al.*, 2010a] and [Gómez-Pedrero *et al.*, 2011], and reproduced with permission of OSA).

Another example of a proper combination of computational electromagnetism results and optics is the case of optical characterization of reflectarrays. The phase map produced at the resonant structure level is arranged and stitched among elements to realize a propagating wavefront using the same reasoning as Huygens' principle describes: the individual wavelets generated at the resonant

elements combine to form the wave that is propagating through the corresponding media. This approach has made possible the analysis of the optical performance of reflectarrays, in the same way and with the same metrics as those used in regular optical systems [Ginn *et al.*, 2010a] [Gómez-Pedrero *et al.*, 2011]. In Fig. 3.20 we show how the modeling of unit cells changing the phase according to the reflectarray pattern is modeled as a phase window to obtain the amplitude distribution at any plane after the reflectarray. This calculation is done by using wave propagation kernels. These elements will be treated in more depth in section 7.3.

Chapter 4
Fabrication

Fabrication of infrared and optical antennas requires high-resolution lithography so that thin films of the required materials can be deposited and patterned onto a suitable substrate. Resonant structures, including multilayer arrangements, are also made with nanofabrication techniques [Tharp *et al.*, 2008]. Compared to the operating wavelength, the overall size of the antenna structures themselves is subwavelength in dimension. It is useful to have about a factor of ten higher resolution available than the overall dimension of the structure, so that fine features and sharp corners can be implemented in the design, as seen in the example shown in Fig. 4.1 [González, 2003] [Cuadrado *et al.*, 2015a].

Experimental research in device development often involves fabrication of one-of-a-kind devices, or at least small batches of devices. From a flexibility point of view, this indicates the convenience of electron-beam lithography so that evolving designs can be changed and adapted according to experimental results. This has the disadvantage of the relatively slow, serial nature of the electron-beam writing process. When device designs become more mature, mask-based optical lithography can be usefully employed to take advantage of the parallel nature of the process to increase the speed of fabrication and the device throughput. It is worth considering early on the choice of specific materials to be used in a device so that compatibility with standard foundry processes may be obtained if possible.

Several techniques have been used to fabricate optical antennas and resonant elements. Optical lithography, which is extensively employed in microelectronics integrated circuit fabrication, has been successfully applied to the generation of optical antennas in the infrared. In the far-infrared range the effect of imperfections and lower spatial resolution of optical lithography is less relevant, and modern deep-ultraviolet optical lithography techniques are applicable for some devices and structures. However, when the wavelength of operation shrinks, the constraints on the spatial resolution and fine detail of the fabricated elements are beyond the limitations of optical lithography. In these cases, probably the most popular technique is electron-beam lithography

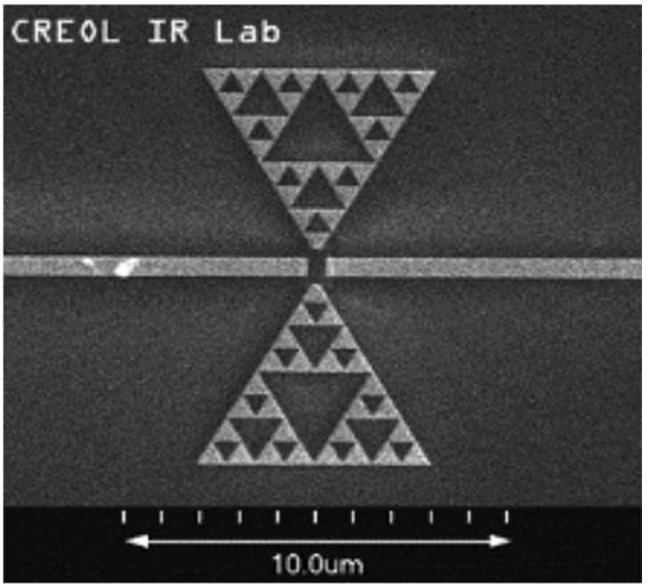

Figure 4.1 Example of substructure in an infrared fractal antenna (adapted from [González, 2003]).

[Gritz *et al.*, 2003b]. This technique is able to generate nanosized structures smooth enough to sustain currents on and within the fabricated elements. In the following section we describe the main steps necessary to fabricate optical antennas using electron-beam lithography technologies. In addition to this nanofabrication technology, the need for large-area and low-cost devices has encouraged the development of cheaper alternative techniques. Among them we can name nano-imprint technology [Puscasu *et al.*, 2000a] and projection lithography [Bonakdar *et al.*, 2015].

4.1 Optical and Electron-beam Lithography

The first step in the lithographic process is to deposit a uniform, thin layer of light- or electron-sensitive material called resist onto the substrate material, most often a semiconductor wafer. The most common method to apply resist to the wafer is spin coating. A small amount of liquid resist is deposited at the center of the wafer, which is attached by a vacuum chuck to a pedestal that can be spun rapidly after the resist is dispensed. The thickness of the resulting film of resist depends on the angular rotation speed, the duration of the process, and the viscosity of the liquid resist. The next step is typically to heat the wafer to drive off solvent from the resist layer. This has the effect of improving the adhesion of the resist film to the wafer, and also serves to anneal residual stresses in the film. At that point, the desired spatial

information is transferred into the resist pattern by exposure to either light (optical lithography) or electrons (e-beam lithography). Exposure to light or electrons causes breakage of chemical bonds in positive resists, or cross linking of polymers in negative resists. These chemical changes make the resist either more soluble to a developer (positive resist) or less soluble (negative resist).

Both the present generation of ultraviolet optical-lithography systems as well as typical electron-beam systems have sufficient resolution to accommodate most optical and infrared antenna designs. In optical lithography, the resist layer is selectively exposed by passing narrowband, short-wavelength light through a reticle or mask that has the spatial pattern information for the particular layer being fabricated. The resolution limit is approximately given as the ratio between the exposure wavelength and the numerical aperture of the projection lens. In electron-beam lithography, a focused beam of electrons is scanned across the region to be exposed, with the pattern transfer accomplished by temporal modulation of the moving electron beam. To facilitate faster writing speeds, an electron-beam system will usually decompose the desired pattern into elementary shapes and operate in a vector-scan mode, scanning the electron beam over only those areas that are to be exposed. This is much faster than a simple serial-writing process that exposes one pixel at a time. The typical electron-acceleration voltage used is on the order of tens of kilovolts. This voltage transforms into the equivalent wavelength of the electron by means of the de Broglie relation:

$$\lambda = \frac{h}{\sqrt{2m_e eV}}, \tag{4.1}$$

where h is Planck's constant, and m_e and e are the mass and charge of the electron, respectively, where V is the acceleration voltage. For example, for $V = 10\,\text{kV}$, the equivalent de Broglie wavelength is $\lambda = 0.0122\,\text{nm}$. Then, the resolution limit is set by the diameter of the scanning electron beam. The resolution is also affected by small-angle forward scattering in the resist or large-angle backscattering from the substrate. Both of these processes result in some exposure outside the desired areas, referred to as the proximity effect.

Since most structures require successive layers of different materials, an important aspect of the lithographic process is layer-to-layer alignment, especially critical for accurate positioning of very small structures. Most electron-beam systems have the capability to detect alignment marks placed within the field of view of the instrument, based on electron backscatter from metallic features. Often there will be a series of nested alignment features, facilitating both global and local alignment. Alternatively, optical lithography systems typically have dual-sided imaging capabilities to facilitate positioning of successive layers or back-side printing.

4.1.1 Choice of resist

The performance of a resist is specified in terms of sensitivity (the amount of energy per unit area necessary to create the desired chemical change) and resolution (the smallest feature that can be reproduced). As a general rule, resists with the highest resolution are the least sensitive. Photoresists normally have three components: a resin material that acts as a matrix, an active compound, and a solvent that controls the mechanical properties, such as viscosity. Positive resists usually have better resolution than negative resists, since the unexposed regions are not penetrated by the developer. In negative resists, the developer penetrates both the exposed and unexposed regions, with some consequent swelling and distortion of the resist pattern.

Polymethyl methacrylate (PMMA) is a commonly used positive resist for e-beam lithography. It has high resolution but low sensitivity, requiring a dose of about $100\,\mu C/cm^2$. Another characteristic of PMMA is that it has poor resistance to plasma etching. Research to improve the sensitivity of PMMA led to new resists with higher sensitivities, for instance, copolymer P(MMA-MAA), which is prepared by copolymerizing methyl methacrylate and methacrylic acid. When thick layers of resist are necessary for implementing a liftoff process, a bi-layer resist structure is often made by spinning PMMA on top of a P(MMA-MAA) layer. The liftoff is implemented by immersing the sample in acetone or methylene chloride.

4.1.2 Patterning processes

Two basic processes are used to define the desired spatial patterns on the substrate where the pattern transfer takes place by having some areas protected with resist and other areas exposed. In a subtractive process, the entire substrate is covered by a thin film layer, of which selected regions are protected by resist. An etch process then removes material from the areas unprotected by resist. In an additive process, also known as liftoff, the substrate is coated with a resist layer that is patterned with openings where the next layer's material is to be deposited. A thin film of the desired material is then deposited over the entire surface. The substrate is then immersed into a solvent solution that dissolves the resist so that the material deposited on the top of the resist is removed and the material deposited into the openings in the resist layer remains. Figure 4.2 illustrates the two processes.

In order to ensure a successful liftoff, it is necessary to have a distinct separation between the material deposited on top of the resist and that deposited on the exposed substrate. A general rule of thumb is that the resist thickness should be about three times that of the film that is to be lifted off. To ensure liftoff with thick layers, a bi-layer resist scheme is commonly used (see Fig 4.3). A thick layer of resist with high sensitivity is deposited onto the substrate first, then a thinner layer of resist with low sensitivity but high

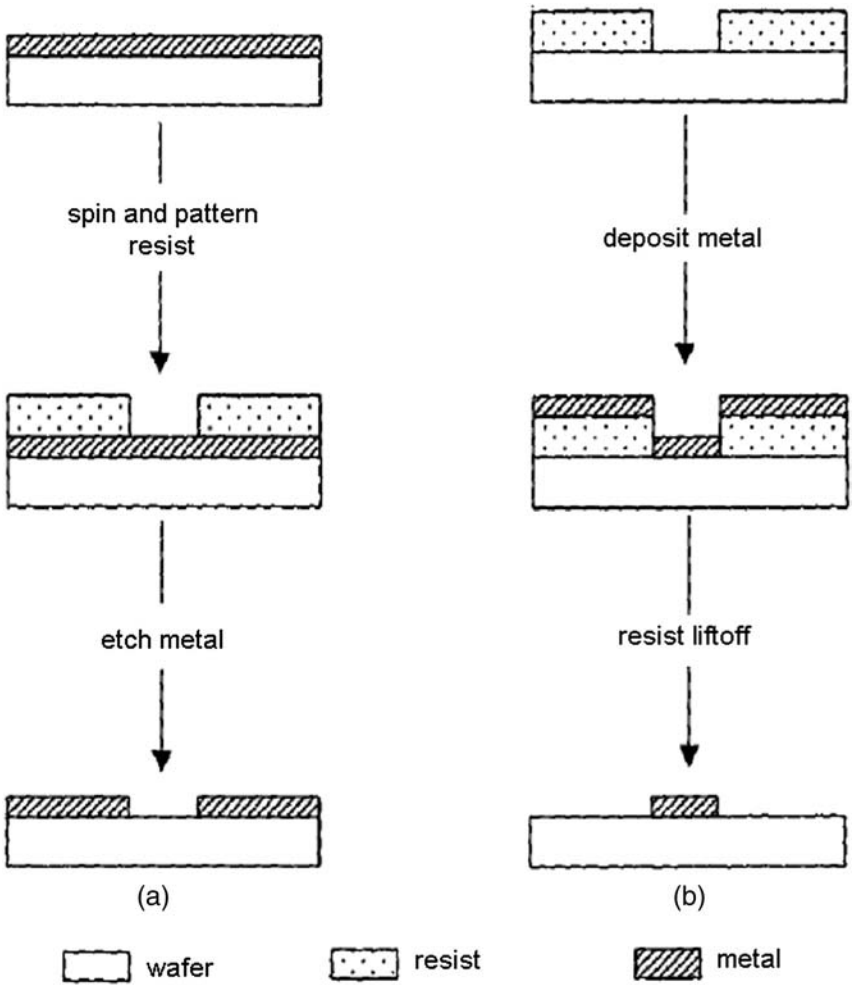

Figure 4.2 Pattern definitions by (a) subtractive etching and (b) additive liftoff (adapted from [Codreanu, 2001]).

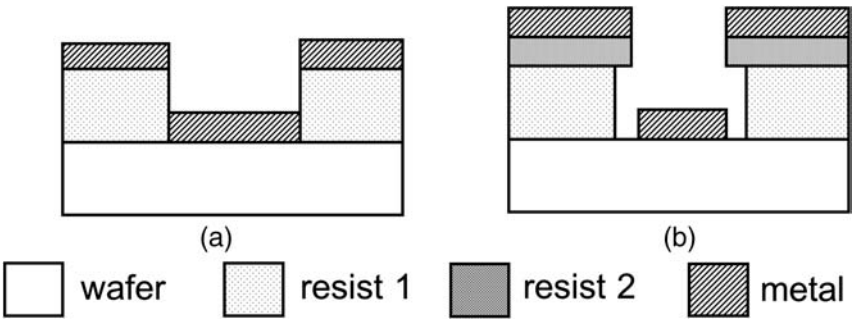

Figure 4.3 Pattern definitions using liftoff with (a) single-layer resist and (b) bi-layer resist (adapted from [Codreanu, 2001]).

resolution is deposited on top. Assuming a directional deposition of material, the linewidth on the substrate will be determined by the high-resolution top layer of resist. Owing to its higher sensitivity, the bottom layer of resist is exposed over a wider region, leading to an undercut profile. When the material to be lifted off is deposited over the bi-layer structure, it does not come in contact with the bottom layer of resist because of the undercut. This ensures a distinct break in the top film of material, allowing a clean liftoff of the pattern adhering to the substrate.

4.2 Thin-Film Deposition Methods

In the fabrication of optical and infrared antennas, it is necessary to be able to accurately deposit continuous films of known thickness of both metals and dielectrics onto appropriate substrates. The metals are used to fabricate ground planes, adhesion layers, and antenna structures. Dielectric materials are often used as stand-off layers between a ground plane and an antenna, or as overcoat layers. It is advisable to implement a witness sample in any developmental deposition process so that physical and optical measurements can be made on the as-deposited film to determine thickness and complex refractive index. Several techniques are available for this process. The most commonly used are evaporation, sputtering, and chemical vapor deposition, with all of their possible variations.

4.2.1 Evaporation

In the evaporation process, a material is heated to its vaporization temperature by means of resistance heating (thermal evaporation) or a beam of energetic electrons (electron-beam evaporation). Thermal evaporation is achieved by placing the material to be deposited into a crucible of high-melting-temperature metal such as tungsten. An electric current is passed through the crucible, raising the temperature of the material to the melting point and then to the evaporation point. In an e-beam evaporation system, a high-intensity beam of electrons is focused onto a ceramic crucible containing the evaporant material. The electron beam is moved magnetically across the crucible, leading to uniform heating of the material. Evaporation takes place in a high vacuum environment (typically 10^{-7} Torr), which implies a long mean-free path of the evaporated constituents. This tends to make evaporation a directional process, since the evaporant travels in a straight path until it strikes a surface where a film of material is formed. This characteristic of evaporation makes it difficult to deposit a continuous film over a step-height change on the substrate, with the evaporated film often becoming discontinuous on a vertical wall. This can be advantageous for implementing a liftoff procedure, or for shadow evaporation, where non-continuous films are required. If a continuous film is desired, a non-directional deposition method

such as sputtering is indicated. It should also be noted that the evaporation process works best for elemental materials, and that alloys and compounds tend to dissociate under evaporation, making the composition of the resulting film difficult to control.

4.2.2 Sputtering

In the sputtering process, the target material is bombarded by energetic ions generated in an electric discharge, physically dislodging the material to be deposited from the target. The dislodged material travels toward the substrate because of a voltage difference held between the target cathode and the substrate. The directionality of the process is affected by the pressure of the gas in the chamber in which the sputtering occurs. The gas environment can be inert or reactive, depending on the process to be implemented. Pressure within a sputtering chamber is generally within the range of 10^{-4} to 10^{-1} Torr. At low pressures, the sputtered material tends to travel in a straight path, while at higher pressures, the material deposition is less directional, providing better step coverage of the substrate topology. There are many parameters that can be varied in a sputtering process, allowing control of the chemical and physical properties of the deposited film. Because the deposition process is physical in nature, sputtering can be used with a wide variety of materials, from metals to insulators. Conductive materials are generally sputtered using a DC power source, whereas dielectric materials require an RF power source because of charge accumulation on the target surface. A magnetron sputtering system uses a magnetic field in the vicinity of the target to force the electrons into spiral paths, increasing the sputtering rate. Sputtering of alloys or compounds generally results in a film of similar composition to the target material.

4.2.3 Chemical vapor deposition

The chemical vapor deposition (CVD) process involves the introduction of reactive gases into the deposition chamber. Chemical reactions between these gases deposit a film on the substrate, which is generally held at an elevated temperature. Controlling the reactant gas flow rates provides control of the film stoichiometry. An advantage of plasma-enhanced CVD (PECVD) is that the deposition reaction can occur even for relatively low substrate temperatures (typically less than 300 °C). CVD processes generally have good step coverage and produce high-quality films.

4.3 Etching

After thin films are deposited onto the substrate, they can be patterned by selective etching. Etching is done in either a wet or dry environment. Wet etching involves the use of liquid etchants, where the exposed material is

removed primarily by chemical processes. Dry etching uses gas-phase etchants in a plasma environment, where the material removal is a combination of chemical and physical processes. Wet etch processes are usually isotropic, whereas plasma etching is generally more directional in nature, providing a more accurate pattern transfer, as seen in Fig. 4.4. Important criteria for selecting an etch process are the material etch rate, the capability of a process to selectively etch a material, and the degree of anisotropy. Oxides, nitrides, or metals are robust to etch conditions as compared to photoresist, and are referred to as hard masks. These materials may be selectively etched, usually with photoresist as the masking layer. The etching of a thin film is typically continued until the next layer (the etch stop) is reached.

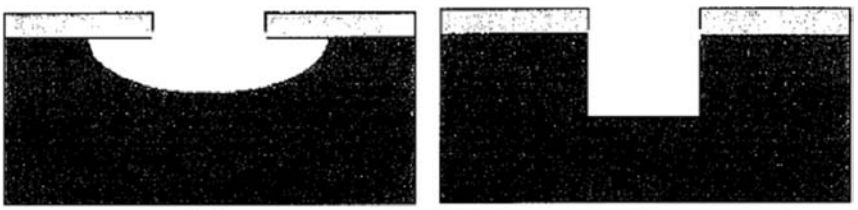

Figure 4.4 Schematic of (a) isotropic and (b) anisotropic etching (adapted from [González, 2003]).

Chapter 5
Characterization and Testing of Infrared Antennas

These days, when computational power and resources are widely available, it is commonplace to rely on numerical tools that have demonstrated their capabilities to simulate physical phenomena involving electromagnetic radiation and its interaction with materials. However, we should recall that the scientific method is based on the comparison of the outputs given by physical models to the results of measurements of those outputs. Furthermore, from an engineering point of view, simulation is just an extension of the design process, and only through measurement and testing can the fabricated devices reach their final realization. A well-executed measurement is always more certain than simulations and provides the true values of the physical parameters being analyzed. Therefore, all of our efforts to understand, model, and simulate how antennas behave within the IR/optical regime should be compared against the actual measurements of the as-fabricated devices.

In this chapter we explain how experimental conditions and setups have been adapted for the testing and evaluation of antenna-coupled sensors.

Characterization of antenna-coupled IR sensors falls into several categories: spatial, angular, spectral, and polarization response. Signal-to-noise ratio and specific detectivity are also of primary importance when characterizing optical antennas.

5.1 Spatial Responsivity

The signal obtained from a detector is proportional to the irradiance distribution integrated over the collecting area of the device. For classical macroscopic IR sensors, the photosensitive region is well defined and is usually described as an effective area within which a constant spatial responsivity is assumed, with zero response outside. To characterize such devices, one typically scans a probe beam across the photosensitive region, measuring the

output of the detector as a function of the position of the probe beam. The measured output signal is, in general, the convolution of the sensor's spatial responsivity and the beam profile. If the dimensions of the photosensitive region are large compared with the beam, the detector's spatial responsivity can be approximated directly as the measured output signal.

An antenna-coupled detector presents a different situation compared to the usual IR detector, where a physical detection area is clearly defined in the form of a pixel or limited receiving area. Antennas are subwavelength structures that can be considered as the minimum-sized detector for an electromagnetic wave. For the simplest design of a half-wave dipole in vacuum, this means a length of around 3–4 μm for an element in the infrared ($\lambda = 10.6\,\mu m$), where we have already taken into account the wavelength scaling due to the dispersive properties of metal in the infrared and the effect of the substrate refractive index [Novotny, 2007].

On the other hand, antenna-coupled devices respond to the electric field distribution falling onto them. This field generates currents, and these currents are finally transduced as an electrical signal that is extracted from the device (see section 6.1). In any case, the detected signal carries information about what is happening in the whole antenna structure. Therefore, spatial responsivity can be presented as a map that indicates how each point of the antenna contributes to the detected signal. At a fundamental level, spatial responsivity could be given in terms of the electric field. This approach is of importance when considering the transduction element incorporated at the location of the feed point, or when the incoming field has some phase, or polarization distribution, that affects the spatial distribution of the induced currents within the structure. However, most IR-antenna-coupled devices work, in practice, with a nearly uniform illumination; the electric field can be considered constant, or slowly varying, along the antenna, and phase variations within the spatial domain of the antenna are not considered. In these cases, it is more practical to define the spatial responsivity map in terms of the incident irradiance, $I(x, y)$ (W/cm^2). We will denote the spatial responsivity as $R(x, y)$.

The ideal way to measure a spatial responsivity map is by placing a very concentrated irradiance at the antenna plane and scanning it. However, when a laser beam is focused on the detector, its size is limited by diffraction and by the special characteristics of laser beam propagation [Alda, 2003]. Subwavelength antenna-coupled IR detectors are smaller than the waist dimensions of laser beams, even when low-$f/\#$ focusing optics are used. Roughly speaking, the probe beam will have a minimum area of approximately $\pi(1.22\lambda f/\#)^2$, whereas the effective collecting area of the detector is known to be a fraction of λ^2 [Fumeaux *et al.*, 1999b]. Therefore, the signal given by the antenna is due to the simultaneous contribution of the different portions of the antenna and all of the elements surrounding it that are illuminated by the

beam (lead lines, bond pads, etc.). In this case, the spatial responsivity distribution must be obtained by a deconvolution process.

A method of measuring this parameter is simply to scan the detector across a fixed beam (or to scan the beam across the detector). The retrieved signal, S, will depend on the position of the antenna relative to the beam. This situation is mathematically described by the convolution of the spatial responsivity map (see Fig. 5.1), R, and the irradiance distribution of the illuminating beam, I:

$$S(x,y) = \int_{-\infty}^{\infty}\int_{-\infty}^{\infty} R(x',y')I(x-x',y-y')dx'dy'. \tag{5.1}$$

If the beam were much smaller than the antenna, $I(x,y) \sim \delta(x,y)$, then, by using the sampling properties of the delta function, the signal would be proportional to the spatial responsivity. This is the typical method to assess response non-uniformity when measuring large-area detectors. However, this is not applicable to IR antennas; consequently, the spatial response measurement involves deconvolving the spatial response of the antenna from the data obtained from the raster scan. The deconvolution process is complicated because the antenna typically has dimensions smaller than the probe beam used for the measurement. In order for the deconvolution to work well, a good signal-to-noise ratio is needed, along with an accurate knowledge of the illuminating beam distribution [Alda *et al.*, 1999] [Alda *et al.*, 2004].

Some deconvolution strategies applicable to similar problems have been proposed. In the case of spatial response retrieval, the Richardson–Lucy algorithm [Richardson, 1972] [Lucy, 1974] applied for image enhancement works very well. An important difference between these spatial response measurements and the image enhancement case is that, for optical/IR antenna measurements, the "image" is obtained through a scanning procedure that typically takes tens of minutes. Therefore, it is not practical to average a large

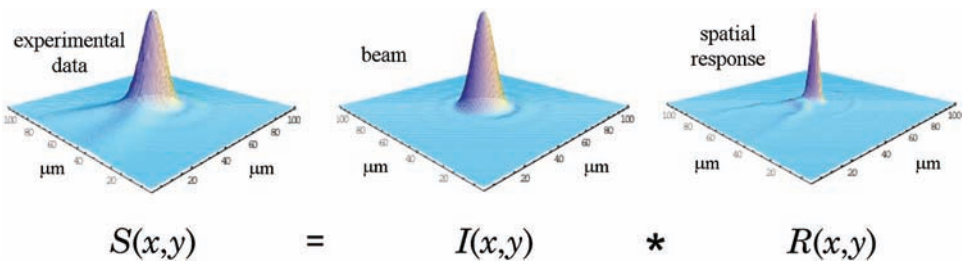

Figure 5.1 The measured signal (left) obtained after a raster scan is the convolution between the beam irradiance (middle) and the actual spatial response (right) (adapted from [Alda *et al.*, 1999] and reproduced with permission of OSA).

number of images to obtain a lower noise level. The residual noise limits the accuracy of the results obtained. On the other hand, the Lucy–Richardson algorithm is iterative. This fact requires the definition of a stop criterion for the iterations. This criterion relies on a comparison between the actual measured response and the calculated spatial response obtained when convolving the irradiance distribution with the results of the Richardson–Lucy algorithm at a given iteration step. When the mean-squared differences between these two results are smaller than the noise-related uncertainties of the measurement process, the algorithm should be stopped and the spatial response retrieved at that iteration [López-Alonso *et al.*, 2005b].

5.1.1 Probe beam characterization

To produce an accurate deconvolution, we need an accurate characterization of the irradiance distribution, $I(x, y)$, of the probe beam at the plane of the measurement [López-Alonso & Alda, 2006]. In the case of image restoration, this corresponds to a faithful characterization of the point spread function (PSF) of the optical system. The plane is chosen to be that of the beam waist where the irradiance reaches its maximum value. In a limiting ideal case, if the beam were a circularly symmetric Gaussian beam, only one knife-edge scan per axial plane would be necessary to obtain the irradiance profile, and this knife-edge data would follow the error function, $\mathrm{erf}(x)$. Although ideally one considers a diffraction-limited beam, the uncertainties in alignment may introduce some residual aberrations. Therefore, a typical beam used in these characterizations will have a waist area of approximately $10\lambda^2$. Pixelated IR imaging systems do not have sufficient spatial resolution to provide a fine enough sampling of such a tightly focused laser beam. Consequently, a knife-edge scanning method is used to characterize the beam [Schneider & Webb, 1981].

In the simplest practical configuration, a knife edge is moved across the beam along two orthogonal axes. Light that is not blocked by the knife edge is detected by a large-area thermal IR detector. To begin the procedures, several knife-edge measurements are taken at different locations along the propagating axis near the beam waist. This is necessary to find the beam waist plane. This plane corresponds with the location having the sharpest knife-edge data. Once the beam waist is identified, two perpendicular knife-edge measurements are taken at this plane. These two orthogonal knife-edge data are compared with another two orthogonal knife-edge results numerically simulated using a postulated model of the beam (see Fig. 5.2). A Gaussian beam is a reasonable starting point for this model if the focusing optics are sized to avoid aperture-truncation effects. The beam model is then refined by the addition of aberrations and diffractive terms as necessary [Born & Wolf, 1980] [Alda *et al.*, 1997] [Mendoza-Yero & Alda, 2007]. In the optical train of Fig. 5.3 the optical system produced a focused spot having a primarily Airy-function character. In addition, residual alignment errors in the setup produced

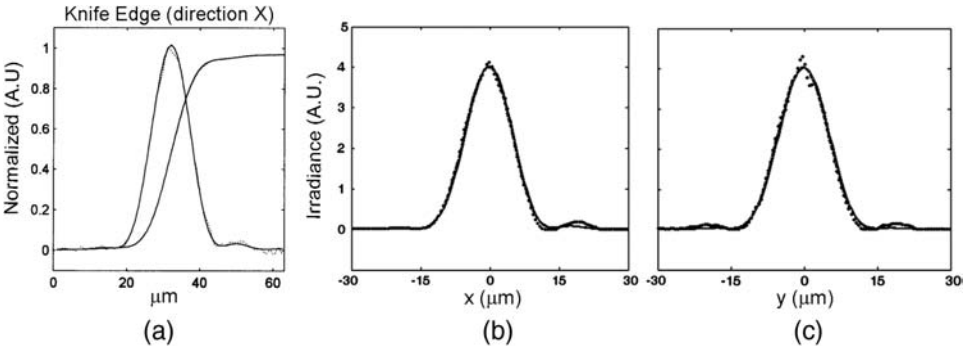

Figure 5.2 (a) Normalized knife-edge data (monotonically increasing curve) and its derivative along the scanning direction. The solid curves represent the simulated knife-edge data for a Gaussian beam containing coma and affected by diffraction. The dashed lines around the curves correspond to the actual measured data (extracted from [Alda *et al.*, 1999] and reproduced with permission of OSA). (b) and (c) Results from two *X* and *Y* scans, represented by the derivative along the knife-edge direction. The solid curves are for the simulated knife-edge calculated from the aberrated beam model, and the dots are obtained from the measurements. In this case, the beam model incorporates spherical aberration and coma, which improves the fitting of the model with the experimental results (adapted from [Mendoza-Yero & Alda, 2007] and reproduced with permission of Elsevier).

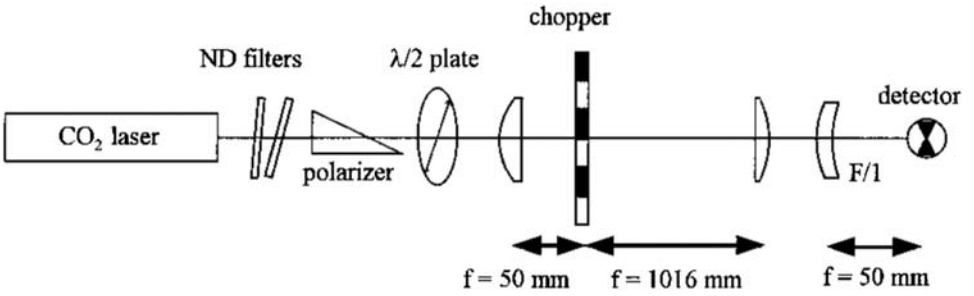

Figure 5.3 Experimental setup used to measure the spatial response of infrared antennas. A CO_2 laser illuminates the detector through an optical train that contains neutral density (ND) filters, polarization control elements ($\lambda/2$ and polarizers), a mechanical chopper for modulation, and a collimation and focusing optics. The detector is placed on a three-axis stage. The movement along the optical axis is used to locate the detector at the beam waist position, and the other two directions serve to obtain the response of the antenna by scanning the device under the beam (adapted from [Alda *et al.*, 1999] and reproduced with permission of OSA).

small amounts of spherical aberration and coma, less than $\lambda/20$. Thus, for deconvolution using two knife-edge measurements, the beam was modeled as a convolution of the Gaussian beam delivered by the laser and the slightly aberrated Airy function [Born & Wolf, 1980].

As shown in Fig. 5.2, knife-edge data follow a monotonically increasing behavior. This is caused by the knife-edge movement over the beam, which

continuously passes more light to the detector as the knife edge moves to open the beam. It is sometimes useful to take the derivative of this function to better visualize the beam dimensions. It is important to note that the Gaussian-like appearance of the derivative in Fig. 5.2 should not be mistaken for a profile of the beam distribution. These plots contain the effect of integrating the beam irradiance along the direction perpendicular to the scan.

A more detailed procedure is possible that avoids the need to construct an aberrated beam model to use in the deconvolution. A tomographic reconstruction method can be used, which allows the spatial irradiance distribution at the antenna (and also the spatial phase) to be determined directly from a set of knife-edge measurements at the beam waist where the knife edge is oriented at a set of different angles, once the beam waist location is found as described above (see left sketch in Fig. 5.4).

The number of angles necessary to reconstruct the incident beam depends on the smoothness of the amplitude and phase variations of the beam under test. In Figs. 5.4.a and 5.4.b we show a collection of 18 knife-edge measurements, equally spaced in angle every 10º, and the reconstructed irradiance distribution after applying a tomographic method based on the Radon transform for a quasi-Gaussian beam in the visible ($\lambda = 658$ nm) [Quabis *et al.*, 2001] [Rico-García, 2007].

When considering actual data, some noise filtering, normalization, and centering of the data set are necessary before applying the tomographic reconstruction algorithms. These knife-edge measurements can be expressed as

$$KE(u,\theta) = \iint I(x,y)\delta(u - x\cos\theta - y\sin\theta)dxdy, \tag{5.2}$$

where u is the variable along the knife-edge movement, and θ is the rotation angle (see Fig. 5.4). From the collection of $KE(u,\theta)$ integrated profiles, it is possible to obtain the irradiance distribution, $I(x,y)$, using the inverse Radon transform,

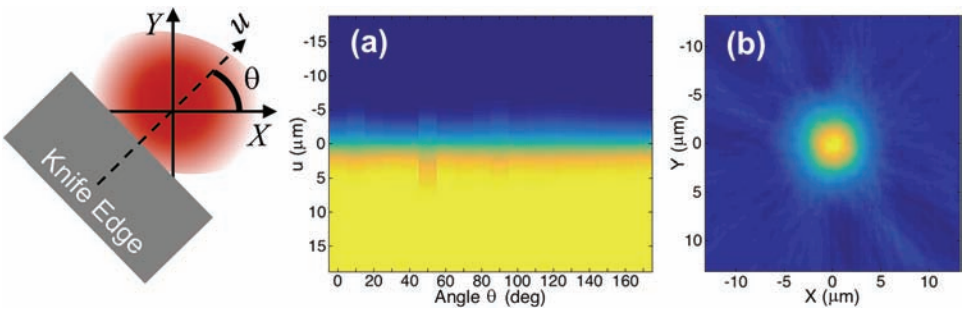

Figure 5.4 Left: The knife edge is scanned over the beam at different angles, θ, along direction u. (a) The measured knife edges produce (b) the irradiance map (adapted from [Rico-García, 2007]).

$$I(x,y) = \int_0^{\pi} \int_{-\infty}^{\infty} d\rho d\theta |\rho| \left[\int_{-\infty}^{\infty} P(u,\theta) e^{-i\rho u} \right] e^{i\phi(x\cos\theta + y\sin\theta)}. \tag{5.3}$$

If we only need the irradiance map for the characterization of the beam, we can stop here, and even apply the method to a single axial plane. We have seen that the spatial responsivity map retrieval uses an irradiance distribution with a flat phase distribution on the plane of the antenna. To refine the characterization of the probe beam, it is interesting to check how flat and constant the phase is at the plane of interest. In addition, the information of the phase would be necessary if the spatial responsivity were to be given in terms of the electric field. Then, when the phase has to be known or checked, the same tomographic procedure can be applied for a collection of planes along the propagation axis [Gureyev & Nugent, 1996] [Teague, 1983]. The goal is to include the plane of interest, typically the beam waist plane, within the axial range of those measurements. With this information, both irradiance and phase can be extracted using the transport of intensity equation,

$$\frac{2\pi}{\lambda}\frac{\partial I}{\partial z} = -\nabla_{\perp} \cdot (I \nabla \phi), \tag{5.4}$$

where $\nabla_{\perp} = \left(\frac{\partial}{\partial x}, \frac{\partial}{\partial y}\right)$. This approach can be applied to the case of IR laser beams and provides an experimental way of characterizing the phase of the probe beam used for spatial response measurements. Figure 5.5 shows a collection of irradiance and phase maps at different locations along the propagation of the beam obtained using this approach.

5.1.2 Experimental setup

Once we know the spatial distribution of irradiance incident on the antenna, the device is located under this distribution and is moved under the beam. To do this in the infrared, it is possible to use a measurement station as presented in Fig. 5.3. The beam is delivered by a linearly polarized CO_2 laser with a TEM_{00} mode, with enough temporal stability over the measurement time [López-Alonso *et al.*, 2005a]. The plane of polarization can be rotated by a half-wave plate. The laser beam is focused onto the device by a set of lenses. The first lens focuses the beam onto a plane where a mechanical chopper is placed to modulate the beam. A second lens collimates this radiation, filling the aperture of the last lens, which should be as free of spherical aberration as possible while maintaining a low $f/\#$. The antenna is typically illuminated from the substrate side to avoid interference effects occurring at the thermal isolation layer, and to produce a better coupling of the radiation to the antenna–detector structure [Alda *et al.*, 2000]. The device has to be mounted on a three-axis micropositioner stage, and if needed for operation, the

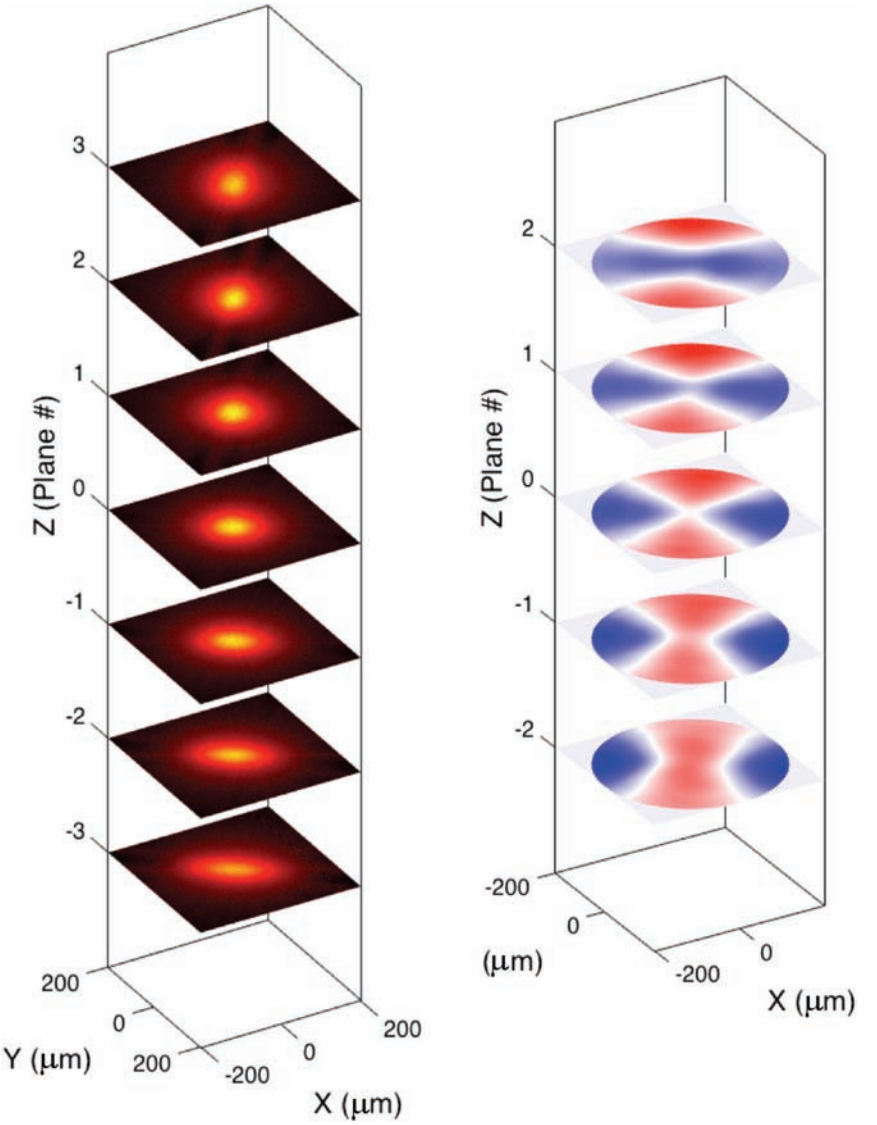

Figure 5.5 Contour maps of (a) the irradiance distribution and (b) phase distribution of a CO_2 laser beam at $\lambda = 10.6\,\mu m$ at different axial planes. The phase has been obtained from the application of the transport of irradiance equation. The laser has an astigmatic profile that changes orientation when passing through the beam waist region. The planes are spaced around 100 μm along the propagation axis (adapted from [Silva-López *et al.*, 2012] and reproduced with permission of OSA).

antenna-coupled detector is connected to a current or voltage biasing source. The detected signal is measured by a lock-in amplifier synchronized with the mechanical chopper. The beam waist has the largest irradiance along the propagating direction. Then, a first approach to the plane of the beam waist is

made by moving the detector along the three axes and by maximizing the response. Once the antenna-coupled sensor is located at the beam waist, the position along the axis of propagation of the beam is fixed, and a 2D serial scan is performed, moving the device in the X and Y directions. A typical scan with 100×100 points requires around 90 minutes with the measurement setup in Fig. 5.3. If necessary and possible, some repetitive scans can be made to improve the signal-to-noise ratio and to decrease uncertainties coming from the setup, or accumulated during the calculation process [López-Alonso *et al.*, 2005b] [Rico-Garcia *et al.*, 2008].

If the antenna has a marked polarization selectivity, as happens for instance with dipole and bow-tie antennas, to obtain a thorough characterization of the device, it is necessary to measure the spatial response for two polarizations, one with the electric field parallel to the antenna axis (co-polarization), and the other with the electric field perpendicular (cross-polarization). The current waves induced in the arms make the parallel response larger than the perpendicular one. The parallel response can be modeled as the sum of two contributions: one arising from a polarization-independent thermal effect in the substrate and the other arising from the antenna response. The thermal response is represented by the deconvolution of the image obtained for the cross-polarization orientation. Finally, the spatial responses for both polarizations are subtracted to obtain the antenna's actual spatial response (see Figs. 5.6.a–c).

Spatial responsivity maps are important when assessing the interaction of the antenna with the auxiliary elements used as signal extraction lines, impedance-matching networks, and other supporting structures. The responsivity map can delineate a detection area as that area containing a given amount

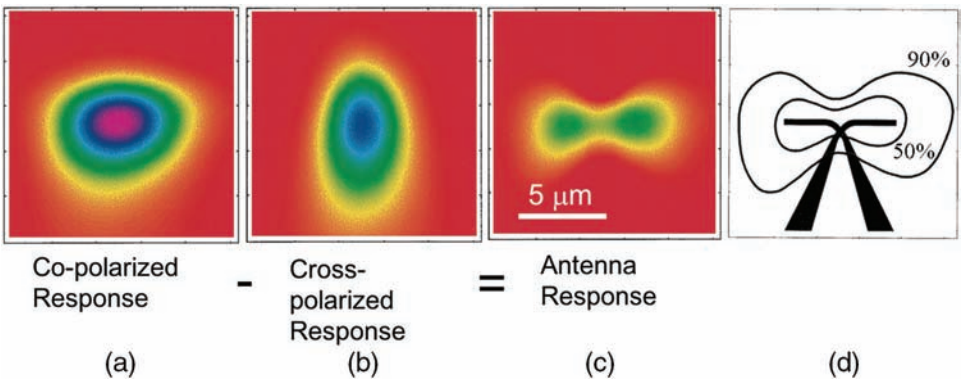

Figure 5.6 (c) The resonant response of a dipole antenna obtained by subtracting (b) the cross-polarized response map from (a) the co-polarized response, to eliminate the thermal non-polarization-dependent response of the device. (d) Plot of the responsivity map for a dipole antenna in the IR. The two contours correspond to the fraction of the total responsivity contained within those lines: 50% and 90% (adapted from [Alda *et al.*, 1999] and reproduced with permission of OSA).

of the total spatial responsivity. Figure 5.6.d shows the case of a dipole antenna where the two contours surrounding the resonant structure contain 50% and 90% of the total responsivity obtained for this antenna.

This spatial responsivity map is of great interest when defining the detection area appearing in the definition of other figures of merit, for example, the specific detectivity, D^*. Additionally, the shape of the responsivity map may be used to conform or adapt the irradiance distribution for better collection and efficiency at a cost of tighter alignment.

5.2 Far-field Measurement: Angular Response

Some antenna arrays have demonstrated a capability to steer the angular pattern of detection [Slovick *et al.*, 2011b] [Cuadrado *et al.*, 2014b]. An antenna-coupled detector's far-field directional properties can be verified by measuring its angular radiation pattern. At infrared frequencies, this pattern can be measured by rotating the device while illuminating it with a laser beam. From an experimental point of view, a far-field measurement might seem to be easier and less demanding than the near-field characterization just described in section 5.1. However, when the angular characterization is made for an antenna-coupled sensor, the illumination conditions have to be very stable and precisely centered on the device under test. Since the devices are of micrometer size, the accuracy in pointing and the required homogeneity of illumination become an issue. An accurate radiation pattern can be measured only if the device is coaligned with the axis of rotation and the focus of the laser beam, and if the beam delivered to the antenna is free of artifacts caused by aberrations [Krenz *et al.*, 2010b] [López-Alonso & Boreman, 2005] [López-Alonso *et al.*, 2005].

In Fig. 5.7 we see how the angular response can be measured. A CO_2 laser operating at $\lambda = 10.6\,\mu m$ is focused onto the device. A quasi-collimated beam obtained from an $f/8$ optical system is used for illumination. Its angular size (7° full angle) determines the angular resolution of the data. The device is

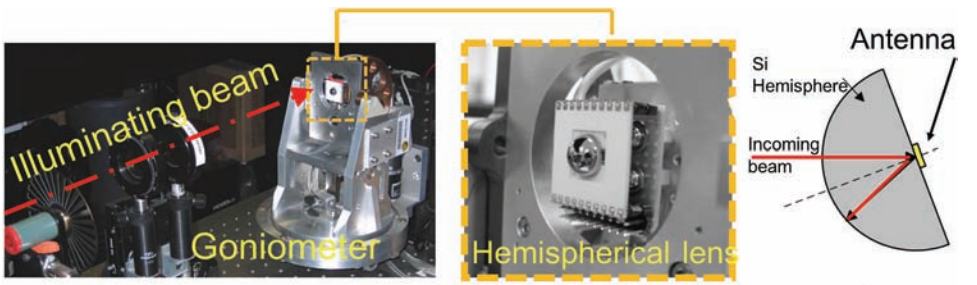

Figure 5.7 Experimental layout to measure the angular response of infrared antennas. The devices are typically illuminated from a substrate made of a hemispherical Si lens. The goniometer specifications and operation are set to maintain the axis of propagation of the incoming radiation intersecting the antenna device.

mounted on a five-axis goniometer, which is shown. The fine position of the antenna-coupled sensor can be manipulated in X, Y, and Z as well as rotated and tilted about the center of rotation of the goniometer. Because the fine XYZ positioning range is limited, the goniometer assembly is mounted on a three-axis nano-mover-controlled stage to allow precise positioning of the device with respect to the laser focus. The goniometer can thus be moved externally, both perpendicular or parallel to the laser beam, thus enabling the device under test to be positioned with eight degrees of freedom. To maintain the desired accuracy for the measurement, it is necessary to follow a detailed alignment procedure that ensures the antenna-coupled sensor is located at the focus of the illuminating beam and that this focus is coincident with the center of rotation [Krenz *et al.*, 2010b]. This precise positioning is necessary because any position errors will induce asymmetric artifacts in the measured angular pattern. This arrangement requires the antenna to be fabricated at the center of the flat surface of a hemispherical lens [Middlebrook *et al.*, 2006]. This choice reduces substrate-mode contributions and improves the coupling of the irradiance to the sensor because of the higher index of Si. Additionally, following a precise measurement procedure, the effect of the lead lines is determined and used to extract the signal from the devices under test [Krenz *et al.*, 2011].

Examples of measured infrared antenna patterns using this technique are seen in Fig. 5.8, which compares (a) a one-element dipole, (b) a two-element dipole phased array, and (c) an asymmetric configuration of a two-dipole phased array that steers the radiation pattern. The experimental results (dots) are compared with the numerical evaluation using a computational electromagnetism package (HFSS from ANSYS Inc.) [Slovick *et al.*, 2011a].

One open issue is that classical antenna theory states that there is a Fourier transform relationship between the E fields on the antenna and the E fields in the far field, at least within the paraxial angular range. The collection area measurements referred to above do not measure electric fields and thus do not provide the required near-field measurement. However, with the recent capabilities of measuring amplitude and phase of fields on IR antennas using the near-field scanning microscope described in section 5.8, this possibility is getting closer to being realized. One limitation is that s-SNOM techniques usually have a fixed angle of incidence. A typical value determined by experimental constraints is around 60º. With illumination at normal incidence in such an instrument, antenna E fields could be measured and then Fourier transformed (and squared) to yield the far-field angular pattern in power units.

5.3 Spectral Selectivity

Due to the lossy behavior of metals at high frequencies, optical antennas show quite a broad spectral response that is not as narrow as for lower-frequency antenna devices [Codreanu & Boreman, 2001]. This broadband response may

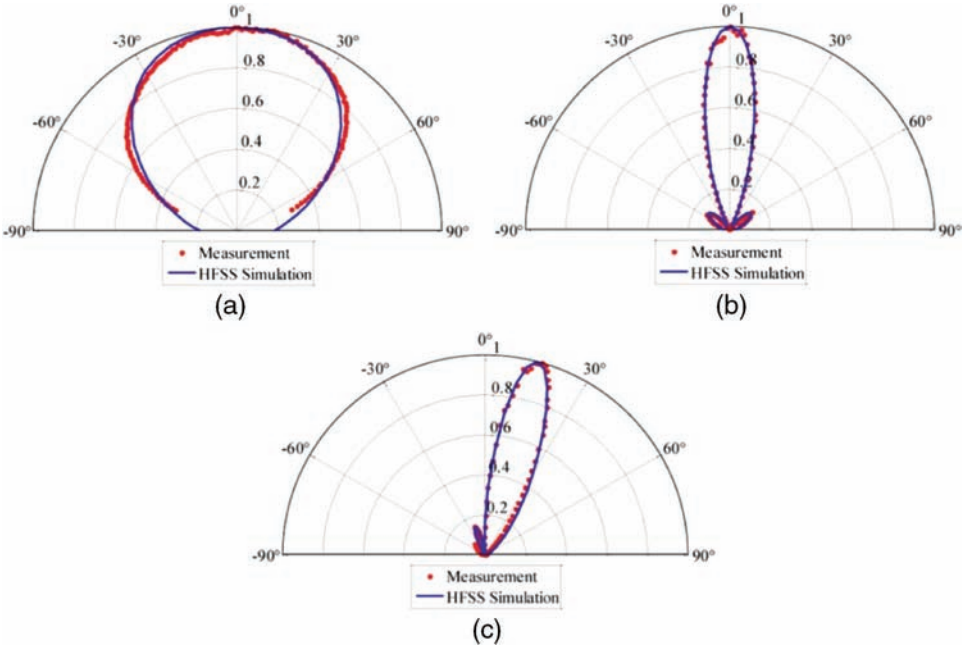

Figure 5.8 Experimental data (dots) obtained with the setup shown in Fig. 5.7 compared with the numerical results obtained from HFSS simulation (solid lines). The angular plots correspond to the reception pattern of (a) a single dipole, (b) a symmetric two-element dipole array, and (c) an asymmetric two-element dipole array for beam steering (adapted from [Slovick *et al.*, 2011a] and reproduced with permission of IEEE).

be advantageous when incident radiation is broadband, as from a blackbody. However, a broad resonance is generally of lower response magnitude. Recent proposals have highlighted the possibility of using temperature as a possible driving parameter when tuning optical antennas [Cuadrado *et al.*, 2017]. In Fig. 5.9 we show results of the broadband spectral response for a microstrip antenna coupled to a bolometer, as well as simulated results for a dipole-antenna-coupled diode, and for an antenna as a distributed bolometer, for the case where the device temperature is varied. In each case we can see that narrow tuning is not possible using these configurations.

The responsivity (output per unit input) as a function of wavelength of an antenna-coupled sensor can be assessed with a source that is tunable in wavelength. If one measures the output power of the source as a function of wavelength with a spectrally flat sensor, and one measures the output from the antenna-coupled sensor as a function of wavelength, the spectral responsivity of the antenna-coupled sensor can be measured. This quantity normally tracks the wavelength resonance of the antenna itself. The problem with this approach is that the spectral irradiance ($W/cm^2/\mu m$) in the output beam of a prism spectrometer is not sufficient to reach a good signal-to-noise ratio with current antenna-coupled IR sensors. Synchrotron sources of course have

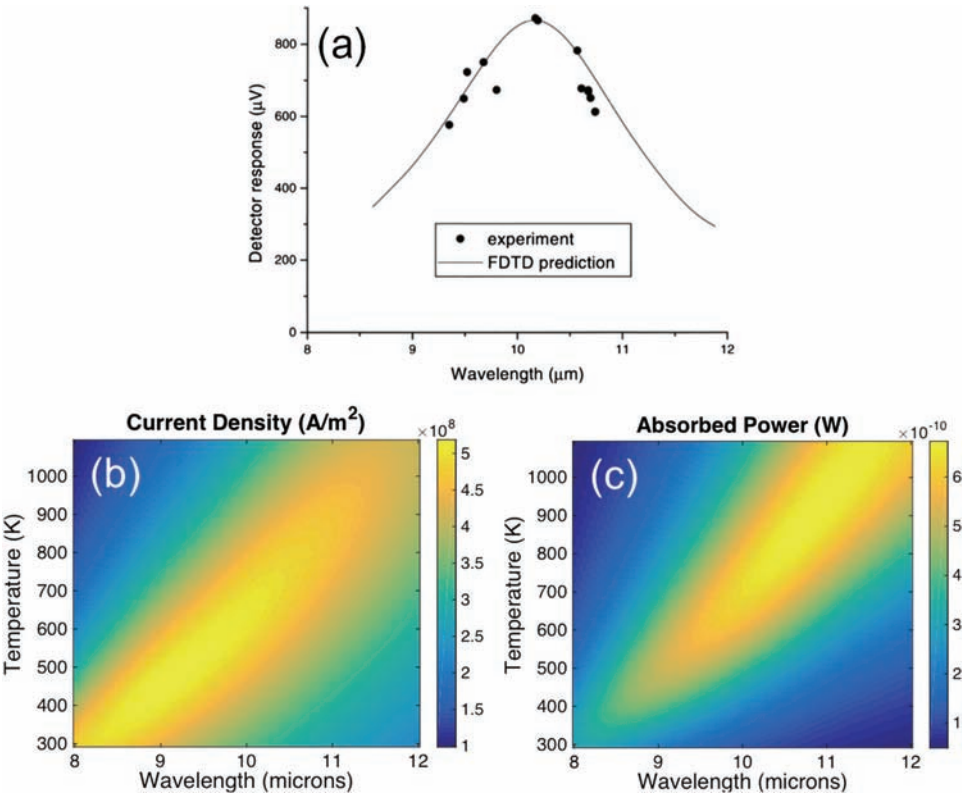

Figure 5.9 The spectral response of antennas is broadband due to the losses and dispersive behavior of metals at IR/optical frequencies. (a) A microstrip antenna coupled to a bolometer (adapted from [Codreanu & Boreman, 2001] and reproduced with permission of Wiley). (b) and (c) Numerical evaluation of the current flowing through the junction (applicable to a metal-oxide-metal diode), and the total absorbed power (for a distributed bolometer) for a dipole antennas, respectively (adapted from [Cuadrado *et al.*, 2017] and reprinted under the terms of Creative Commons Attribution 4.0 International License, http://creativecommons.org/licenses/by/4.0/).

much higher spectral irradiance, but their general inaccessibility makes them inconvenient for sensor measurement. A spectral responsivity measurement can be made with a tunable laser (see Fig. 5.9.a), for instance, using various lines in a CO_2 laser, but this approach still covers a very narrow bandwidth. Using different laser outputs can be used as well, but this provides few data points on the spectral responsivity curve. Broadly tunable sources in the IR such as quantum cascade lasers may be useful for spectral responsivity measurements as they become more reliable and commercially available. One other technique that may be implemented is to replace the sensor in a FTIR setup with the sensor to be measured. Taking the ratio of spectra measured with the sensor under test to spectra measured with the normal (spectrally flat) instrument sensor may give usable data, given the throughput advantages of

FTIR instruments, and perhaps using temporal averaging to increase the measurement signal-to-noise ratio.

In any event, the measured spectral responsivity curve can be compared to that yielded by computational electromagnetic calculations. If the proper material dependencies are included in the computations, the results should be quite similar (see Fig. 5.9.a).

5.4 Polarization Selectivity

An antenna is intrinsically a polarization-selective device, and indeed verification of a polarization-dependent response is a simple and direct proof of antenna-coupled sensor response. Therefore, when testing antenna-coupled devices, one of the first measurements usually checks the response of the antenna versus the state of polarization of the illuminating radiation. The antenna design will impact the polarization response; thus, the geometrical orientation of the antenna arms determines the primary polarization state of the received radiation (see Fig. 5.10). Dipoles and bow-ties respond strongly to linear polarization along the arms. The same happens with log-periodic structures that detect better linear polarization along the orientation of the teeth. Spiral designs select ideally circular polarization states. Electromagnetic duality dictates that slots have polarization orthogonal to metallic structures of corresponding geometry (see section 3.2.1 and Fig. 3.10).

The preferred polarization of an IR antenna for reception is the incident polarization state that gives maximum response from the antenna-coupled sensor. Most assessments of polarization response are performed with a linear

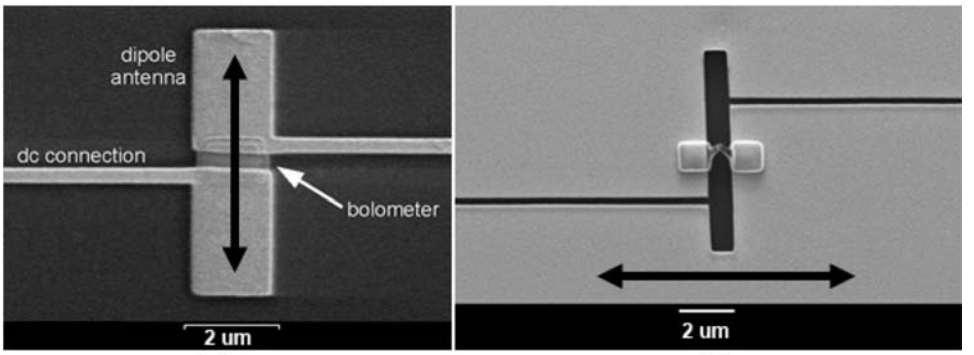

Figure 5.10 The preferred direction of polarization coupled to the antenna depends on its geometry. (a) The dipole antenna resonating along the vertical direction. (b) A slot dipole antenna. In both images the low-frequency signal-extraction lines are arranged as orthogonal as possible with respect to the preferred direction of polarization (adapted from [Codreanu & Boreman, 2002b] and [Abdel-Rahman *et al.*, 2005a], and reproduced with permission of Elsevier and IEEE).

polarization state whose orientation can be controlled by rotation of a half-wave plate. From those measurements a maximum and minimum response orientation can be determined, and polarization contrast measured. Equal response to both linear polarizations for a spiral antenna would indicate circular polarization in reception. Of course, illumination with left-circular and right-circular handedness can be used for more detailed circular polarization characterization.

At the same time, one sees cross-polarization effects from low-frequency lead lines, bond pads, etc., the result being that spirals generally have elliptical polarization on reception, and linearly polarized antennas have a distinct but non-unity linear polarization contrast. Generally, in the design of an antenna, one orients the lead lines to be orthogonal to the primary polarization desired in the antenna (see Fig. 5.10). Besides that, the contribution produced by absorption and the thermal response of the substrate and signal extraction lines is not negligible and provides a polarization-independent response that is added to the polarization-dependent signal. This is why, when analyzing the spatial response of the antenna structure, it is necessary to subtract the cross-polarized signal from the co-polarized one (see section 5.1). In Fig. 5.11 we represent several experimental results where the response of different devices is plotted against the angle of polarization. When the selectivity is in terms of the orientation of a linearly polarized field, the larger the difference between co-polarized and cross-polarized response the better the antenna is resonating and the lower is the contribution of the auxiliary elements that mask the desired response of the antenna structure.

For the case of a metal-oxide-metal tunnel diode coupled to an asymmetric log-spiral antenna, it was found that modulating the sign of the bias voltage led to a tuning of the preferential polarization state [Boreman *et al.*, 1998] for received radiation. This can be explained by the existence of two current modes that propagate on the antenna arms. These two modes are not balanced because of the capacitance of the transducer (a MOM diode) and the asymmetries of the antenna and feed structures. By changing the bias voltage, the balance between the modes is altered, and the signal changes accordingly (see Fig. 5.12) [Fumeaux *et al.*, 1997].

Figure 5.13 shows a typical example of the experimental setup needed to measure the polarization response of an infrared antenna with the case of the analysis of the polarization response of a dipole antenna in the visible [Fumeaux *et al.*, 1999a] [Rico-García, 2007]. The antenna coupled to a Ni-NiO-Ni diode is illuminated with a linearly polarized laser beam coming from a laser diode in the visible. After collimating the beam, three polarization elements are placed consecutively. The first quarter-wave plate compensates any residual ellipticity caused by the monomode optical fiber and assures a linear polarization state after it. The second element is a half-wave plate that rotates the plane of polarization at will. Finally, another quarter-wave plate is placed to generate, if necessary, a circular or elliptical

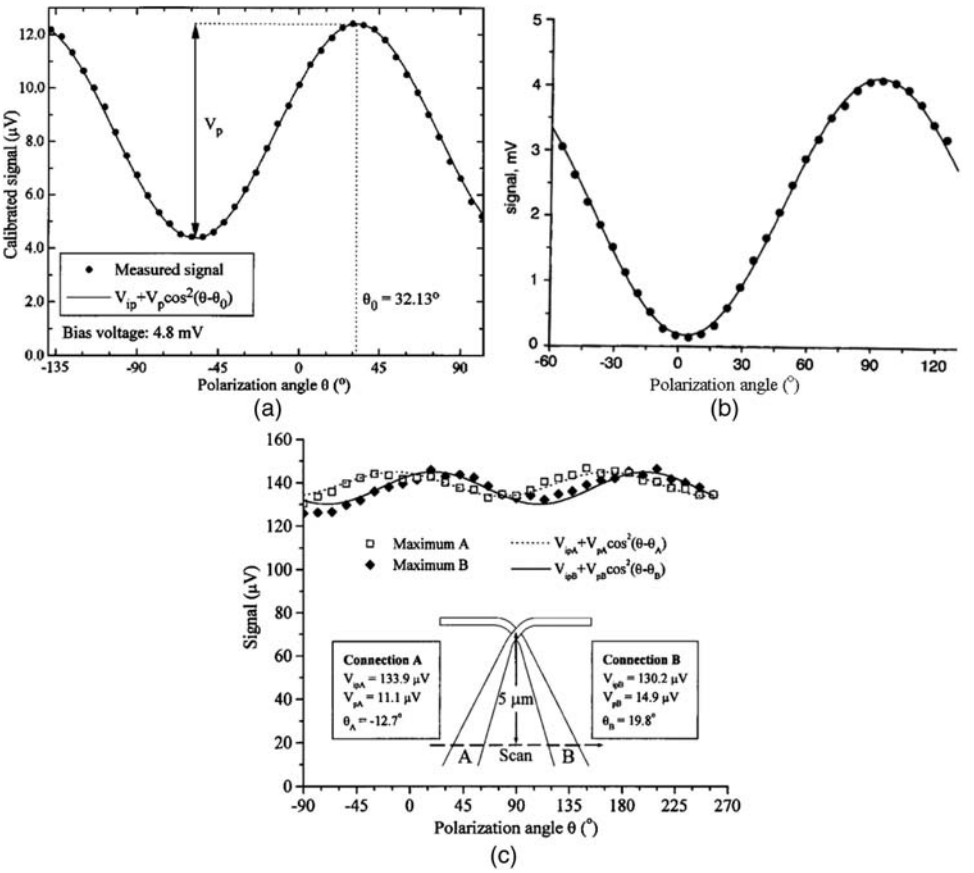

Figure 5.11 Polarization selectivity is one of the simplest tests that verifies the operation of the antenna at the frequency of measurement. This occurs for different geometry antennas coupled with (a) diodes or (b) bolometers in the infrared, or (c) even in the visible (adapted from [Boreman *et al.*, 1998], [Codreanu *et al.*, 1999], and [Fumeaux *et al.*, 1999a], and reproduced with permission of OSA and Institution of Engineering & Technology).

state of polarization. After passing through this polarization configuration subsystem, light is focused onto the antenna and the signal is retrieved by phase-sensitive detection electronics locked in frequency with the modulation frequency of the diode laser driver. An auxiliary beam splitter is placed along the optical train to obtain a reference signal of the irradiance reaching the antenna, and also to see the structure under analysis through the focusing optics for positioning and device selection purposes.

The signal obtained from the antenna is fitted to the following function:

$$V = V_{ip} + V_p \cos^2(\theta - \theta_0), \tag{5.5}$$

where V_{ip} represents the polarization-independent response, V_p is the depth of the polarization-dependent signal, and θ is the angle of rotation of the

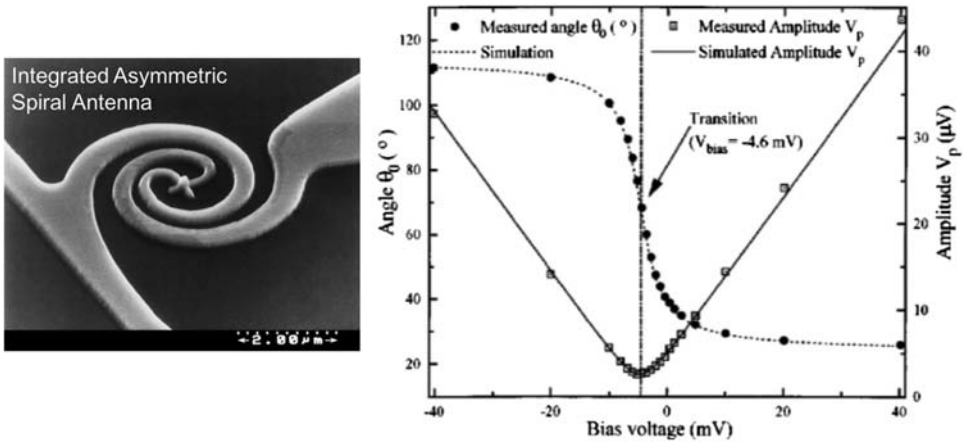

Figure 5.12 The detected polarization state can be tuned using the bias voltage applied to a spiral antenna coupled to a Ni-NiO-Ni diode (adapted from [Boreman *et al.*, 1998] and reproduced with permission of OSA).

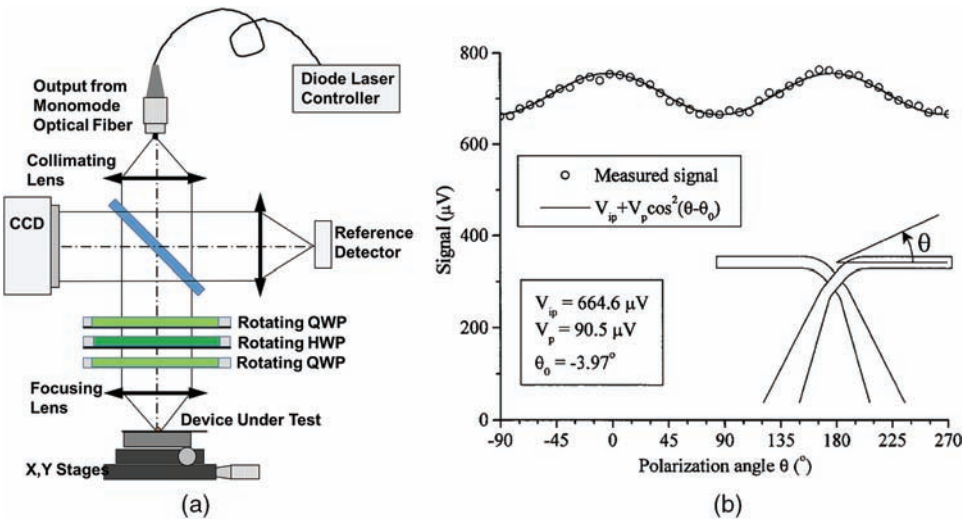

Figure 5.13 (a) Experimental setup for characterizing the polarization response of antennas in the visible. Light coming from a diode laser is collimated and its polarization state is changed and controlled by a subsystem composed of a quarter-wave plate (QWP), a half-wave plate (HWP), and a quarter-wave plate (QWP). Finally, a focusing lens illuminates the antenna, providing the response signal [Rico-García, 2007]. (b) This signal is fitted with Eq. (5.5) (adapted from [Fumeaux *et al.*, 1999a] and reproduced with permission of OSA).

linear polarization state with respect to a given reference (typically oriented along the expected direction of the maximum). Angle θ_0 represents an angular shift that describes some residual orientation mismatch between the antenna structure and the reference frame for polarization measurement.

The ideal situation is when $\theta_0 = 0$. In this case, for a dipole antenna, the maximum signal is measured at a polarization angle close to zero, $\theta \simeq 0$, corresponding to polarization parallel to the antenna dipole axis (see Fig. 5.13). For a symmetric antenna arrangement, the deviation of the value of the angle for the maximum signal, θ_0, can be explained by the mounting tolerances of the detectors on their chip carriers and by the uncertainties of the angular orientation of the polarizing elements. The polarization-dependent contribution to the signal is evidence of an antenna-coupled effect. In addition to the dipole-antenna response, usually there appears a response from the electrical connections to the sensor element. These signal-extraction connections typically respond as long-wire antennas when illuminated at optical or IR frequencies at polarizations consistent with their dominant geometry. In Fig. 5.11.c the connecting lines are responding with a signal that is less than 20% of the maximum detector response. In this case, the response of each connection can also be represented as the sum of a constant and a cosine squared oscillating with the polarization angle (see Fig. 5.13). The two connections exhibit a maximum response oriented according to the geometry of the connections. This response of the electrical connection structure is more noticeable in visible-wavelength experiments than in measurements reported at infrared frequencies. Actually, the antenna under test behaves as a long-wire antenna in the visible, and as a half-wave dipole in the IR.

5.5 Noise in Antenna-Coupled Detectors

The performance of an optical detector is limited by the noise of the physical mechanisms involved in the transduction of the signal. For bolometric devices, it is possible to model the noise as the addition of three main contributions: thermal noise, temperature noise, and Johnson noise. These different sources of noise depend on the geometry as well as the electrical and thermal properties of the material. For diode sensors, there is also a contribution from shot noise. Additionally, most sensors also exhibit $1/f$ noise arising from ohmic contacts.

Johnson noise can be described as a voltage source with the following dependence:

$$V_{\text{Johnson}} = \sqrt{4k_B T R \Delta f}, \tag{5.6}$$

where k_B is the Boltzman constant, Δf is the detection bandwidth, and R is the resistance of the device at temperature T.

Thermal-fluctuation noise appears through the heat exchange between the device at temperature T and the environment at T_0. Typically, this noise is described as a noise-equivalent power (NEP):

$$\mathrm{NEP}_{\mathrm{therm}} = \sqrt{\frac{8k_B A_d \sigma_{\mathrm{SB}} \Delta f (T^5 + T_0^5)}{\epsilon}}, \tag{5.7}$$

where σ_{SB} is the Stefan–Boltzman constant, ϵ is the emissivity of the device, and A_d is the detector area.

Another contribution to noise is called temperature noise, which can be modeled as the following power fluctuation:

$$\sqrt{\langle \Phi_{\mathrm{temp}} \rangle^2} = \sqrt{4k_B K T^2}, \tag{5.8}$$

where K is the thermal conductance of the device.

Shot noise arises from quantization of electric charge and is described by a current passing through a diode:

$$I_{\mathrm{shot}} = \sqrt{2qI_{\mathrm{ave}}\Delta f}, \tag{5.9}$$

where I_{ave} is the average current flowing through the device.

The various noise sources above are given in their traditional forms as voltage, current, or power. Upon transformation by the sensor transduction mechanism and read-out electronics, these noises are manifest in the units of the signal output, typically voltage. These contributions, along with any amplifier noise, add in quadrature to produce a total noise contribution coming from the device itself. In most instances, $1/f$ noise can be filtered out by modulating the incident power using mechanical choppers or other modulation techniques to avoid the high-noise region at low frequencies.

5.6 Signal-to-Noise Ratio and Specific Detectivity, *D**

Two of the most important characterization parameters of antenna-coupled IR sensors are the signal-to-noise ratio (SNR) and the specific detectivity, D^*. To obtain these parameters, the first step is to measure the responsivity, $\mathcal{R}$, of the sensor, defined as

$$\mathcal{R} = \frac{V_{\mathrm{signal}}}{\Phi_{\mathrm{det}}}, \tag{5.10}$$

where V_{signal} is the peak signal voltage, and Φ_{det} is the power falling on the sensor. For an antenna-coupled sensor, one multiplies the incident irradiance, I (W/cm^2), by the effective collection area of the sensor, as characterized in section 5.1. The total collected power can be calculated as

$$\Phi = \int_{-\infty}^{\infty}\int_{-\infty}^{\infty} \bar{R}(x,y)I(x,y)dxdy, \tag{5.11}$$

where $\bar{R}(x,y)$ is a normalized and dimensionless distribution proportional to the spatial responsivity map, $R(x,y)$, defined in section 5.1. As we may see, due to the special characteristics of the spatial response of an optical antenna, specific detectivity requires some adaptation and analysis when applied here [Cuadrado *et al.*, 2015b].

When measuring optical antennas, the optical flux is typically modulated by a mechanical chopper at a few kilohertz, and the peak signal voltage is the peak-to-valley excursion of the sensor output at the chopping frequency, usually read as the output of a lock-in amplifier.

The RMS sensor noise, V_{noise}, is measured in some electrical bandwidth, Δf, generally with an electronic spectrum analyzer. One must be careful that it is the sensor noise being measured, and not the noise of any post-detection amplification. This will require that close attention be paid to the amplifier design so that its noise floor is well below the sensor noise.

The SNR in voltage terms is then given as

$$\text{SNR} = \frac{V_{\text{signal}}}{V_{\text{noise}}}. \tag{5.12}$$

In most IR sensors, the RMS noise level is found empirically to be proportional to the square root of the detector area, A_d. Also, since white noise power is proportional to bandwidth, the RMS level of electronic noise is generally proportional to the square root of the electrical bandwidth. In the case of antenna-coupled IR sensors, the collection area and the sensor area are not constrained to be identical as in the case of classical IR detectors. The actual area of the sensor is quite small, while the collection area of the sensor is on the order of λ^2, as seen in section 5.1. This can be beneficial in terms of increasing the SNR.

Most sensor analyses use the specific detectivity, D^*, to account for the basic dependence on area and bandwidth, defined as follows:

$$D^* = \frac{V_{\text{signal}}\sqrt{A_d}\sqrt{\Delta f}}{V_{\text{noise}}\Phi_{\text{det}}}. \tag{5.13}$$

It can be seen that if V_{noise} is proportional to $\sqrt{A_d}$ [see Eq. (5.7)] and $\sqrt{\Delta f}$ [see Eq. (5.6)], then these effects cancel out and the parameter D^* becomes independent of area and/or bandwidth. The area term in Eq. (5.13) is generally taken as the collection area, which is larger than the sensor area. This is consistent with the placement of sensors in a focal plane array arrangement where the spacing between pixels defines the collection area in

order to avoid pixel-to-pixel crosstalk. So there is potential for antenna-coupled sensors to have higher values of D^* than non-antenna-coupled sensors. The difficulty up to now has been finding an adequate definition of the collection efficiency, i.e., the fraction of the power incident on the collection area of the antenna, Φ_{det}, that actually gets to the sensing element. This parameter has not been characterized quantitatively to date and remains a developmental topic in the pursuit of high-performance antenna-coupled IR sensors. Optimization of the collection efficiency requires that the sensor and the antenna be impedance matched at the IR operating frequencies of interest. This has motivated the development of near-field techniques to assess the feedpoint impedance of IR antenna structures so that impedance-matching networks can be implemented.

5.7 Biasing Electronics and Modulation

Antenna-coupled detectors deliver an electric signal to external read-out electronics. In most of the cases, especially when the transduction mechanism is bolometric, or corresponds to a symmetric metal-insulator-metal diode, an external biasing is required. Because of their small size, the elements under test are fragile and exposed to failure due to thermal damage induced by electrostatic discharge or electric current spikes in the biasing circuit. Although electrostatic discharge is not merely a thermal process, it causes an increase in the temperature of the device that could be catastrophic [González *et al.*, 2000] [Cuadrado *et al.*, 2013c]. On the other hand, if the biasing is reduced too much, the signal-to-noise ratio is also low, and detected signal becomes less reliable.

The selection of voltage or current source for biasing is also of importance when considering the effect of the auxiliary elements around the antenna because the contribution of the impedances of the biasing circuit and the antenna is different depending on the chosen strategy. Figure 5.14 shows these two possibilities where the antenna device is part of a voltage divider network. The voltage signal, V_{out}, is retrieved from this divider. These circuits also include a contribution, $R_{\text{in-chip}}$, that describes the resistance of the auxiliary elements associated with the antenna in the form of lead lines, bond pads, and in-chip wiring. Furthermore, when interested in the temporal response of the devices, the capacitive or inductive contributions of these circuit elements (in-chip and biasing auxiliary impedances) need to be considered. If the transduction mechanism is bolometric, the signal changes because the resistance of the bolometric antenna, R, changes by an amount ΔR. In this case, the change in voltage, ΔV, across the voltage divider is given as

$$\Delta V = V_{\text{bias}} \frac{R_{\text{ext}}}{(R + R_{\text{in-chip}} + R_{\text{ext}})^2} \Delta R, \tag{5.14}$$

and

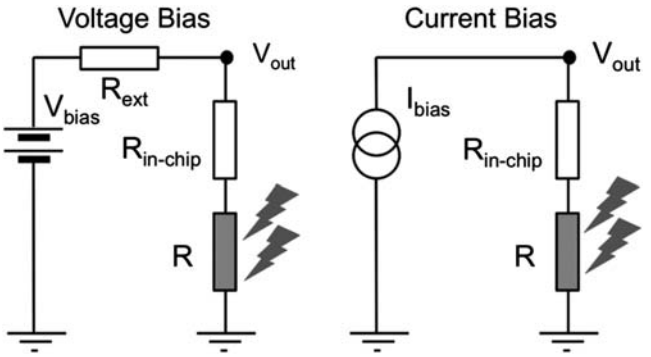

Figure 5.14 Schematics of the two modes of biasing an optical antenna: voltage bias (left) and current bias (right) (adapted from [Cuadrado *et al.*, 2013a] and reproduced with permission of SPIE).

$$\Delta V = I_{\text{bias}} \Delta R, \tag{5.15}$$

for the voltage and current biasing, respectively. We may note that when using voltage biasing, all of the elements in the divider and chip (biasing resistances and in-chip wiring) contribute to the signal obtained from the device.

The voltage extracted from the device, V_{out}, contains the signal caused by the irradiance falling on the antenna, ΔV. To extract it, V_{out} enters a low-noise amplifier that also filters out the DC component of the signal. Finally, the amplified signal, which is proportional to ΔV, is typically acquired by a lock-in amplifier synchronized with the modulation of the incoming radiation.

The reason behind the lock-in detection strategy is the low voltages involved in the detection. On the other hand, both bolometric and metal-insulator-metal (MIM) rectification mechanisms are strongly affected by $1/f$ noise derived from ohmic contacts (see section 5.5). To avoid this and thus obtain a better signal-to-noise ratio, the illuminating irradiance falling onto the devices is modulated, and the signal is typically retrieved using a lock-in amplifier synchronized with the modulation frequency. This frequency is limited by the temporal response of the devices. When antenna-coupled diodes are used for rectification, the transduction mechanism is not usually the limiting factor in the temporal response, and very high modulation frequencies well into the megahertz range can be reached. At the same time, some limitations may appear when modulating the illumination. Laser diodes used in the visible can be easily modulated at very high frequencies (hundreds of megahertz) electronically. However, a typical source in the infrared, the CO_2 laser, is usually modulated using a mechanical chopper. In this case, the modulation frequency is around a few kilohertz. Higher modulation frequencies can be obtained using an acousto-optic modulator.

5.8 Near-field Measurements using s-SNOM Techniques

Spatial responsivity provides an overall response of the antenna-coupled device when registering the signal provided by the transduction mechanism. However, what can be done to characterize the response of the device in the near field when the resonant elements do not produce any electric signal to an external circuit? We desire a method to analyze the response of frequency-selective-surface, or meander-line, or reflectarray elements at the same plane as where they are built.

Computational electromagnetism has an answer to this question, but it is a result based only on numerical evaluation. These results, although reliable, should be compared against experimental results. This is where near-field techniques play a role [Barnard *et al.*, 2011] [Tucker *et al.*, 2013] [Tucker *et al.*, 2014] [Tucker *et al.*, 2015].

Scattering scanning near-field optical microscopy (s-SNOM) is able to provide a signal directly related to the electromagnetic response of the structures under test. s-SNOM uses the tip of a metal-coated cantilever to scan the near field produced by a resonant structure. The very same near field calculated from computational electromagnetism can be measured with this technique. In the most common configuration, the tip and cantilever are part of an atomic force microscope (AFM) system.

A basic description of a s-SNOM system is a combination of an AFM and a customized illumination and detection system that incorporates an interferometer. The detected signal is treated by a dedicated lock-in amplifier properly set with the parameters of the AFM. During the measurement, the AFM tip engages with the structure in tapping mode, oscillating at its mechanical resonance frequency, f_{tip} (typically in the hundreds of kilohertz). The structure is simultaneously illuminated by an optical excitation coming from a laser source. This incidence is oblique, and the polarization angle is selected in such a way that it excites the resonant element, producing a near-field response to this excitation. The geometry of the incidence beam, its state of polarization, and the tip orientation, are selected in such a way that the tip scatters part of the generated near field. The same optics used for illuminating the field collects the backscattered radiation and forwards it into a detection arm. The actual backscattered light is composed of several contributions, including specular reflection components that may be much larger than the near-field signal and thus constitute a background. It is necessary to suppress this background to extract the near-field information. This can be accomplished by dithering (vibrating) the AFM tip at a frequency f_{AFM}. Because the amplitude of this vibration is small (typically 20 nm), the background specularly scattered signal does not vary significantly with respect to the dither frequency. However, the near field (which decays rapidly away from the surface, resulting in this component) is modulated by the mechanical

frequency of the AFM, f_{AFM}. The nonlinearity of the near-field contributions results in their better isolation from the background when detecting the second or third harmonic of this frequency ($2f_{\mathrm{tip}}$, $3f_{\mathrm{tip}}$). The background signal is further suppressed by isolating the linear polarization orientation scattered by the tip. If we use an XYZ coordinate system as in Fig. 5.15, where the sample is placed on the XY plane, the tip enhances the E_z component. This becomes particularly effective if the E_z component is cross-polarized with respect to the optical excitation. When the sample is illuminated by radiation polarized in the X direction, much of the background signal can be blocked by a wire-grid polarizer transmitting only scattered radiation polarized along Z.

To obtain a map of the near field, the sample is moved in a raster-scan pattern under a static illuminating beam and a stationary cantilever tip driven in tapping mode. Besides the proper setting of the optical excitation and retrieval of the interferometric signal, an s-SNOM measurement requires an appropriate detection setup. The acquisition of the signal relies on the combination of an interferometer and a phase-locked detection to extract the frequency components of interest using a lock-in amplifier.

In the s-SNOM technique, the sample is illuminated from the far field. The sample scatters this wave, producing both far- and near-field components. The near field contains information that is cut off by diffraction from propagating into the far field and would ordinarily remain undetectable. Figure 5.15 shows a

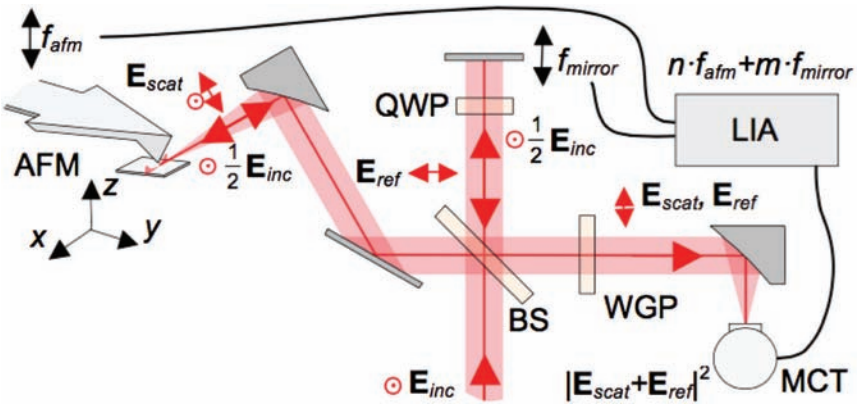

Figure 5.15 Example of an s-SNOM system. The beam illuminating the system is directed with a selected state of polarization towards the sample. The sample is scanned with an AFM tip that is typically driven in tapping mode. The back-scattered light is collected and directed towards an interferometric detection arm that combines the scattered radiation with a reference beam on a detector. The detection arm is also able to select the desired polarization state to properly suppress the background signal. The signal from the detector is read by a lock-in amplifier (LIA) driven by the AFM cantilever vibrating frequency, f_{AFM}. If the detection technique uses the pseudo-heterodyne mode, the mirror at the reference beam moves harmonically at a different frequency, f_{mirror} (adapted from [Moreno *et al.*, 2017] and reproduced with permission of OSA).

diagram of the main elements and subsystems involved in the s-SNOM setup. The AFM tip locally interacts with the near field and scatters it into the far field. An optical system collects radiation scattered from the vicinity of the tip. Then, by bringing the scattered signal into the interferometer, it is possible to obtain the values of both the amplitude and phase of the near field along the direction of the tip, generated by the resonant structure. The use of the interferometer effectively amplifies the tip-modulated signal. It also allows the extraction of both the modulus and phase of the near field. To obtain the phase, the near-field signal is combined interferometrically with a reference signal for which the absolute phase can be controlled. This reference signal is typically given by a reference leg that uses a flat mirror moved axially along its normal. One approach is to combine scans with successive registration of the interference signal for several axial positions of the reference mirror. These scans are used to fit the phase map. Figure 5.15 shows a general layout of an s-SNOM measuring station. In the infrared, the excitation source is a CO_2 laser. The polarization of the laser is selected in such a way that the currents at the resonant structure are properly excited. The back-scattered radiation is directed towards a HgCdTe detector. This detector also receives the signal from a mirror that is displaced using a piezo stage.

Besides its intrinsic interest when characterizing these decives, the information about the near-field distribution actually occurring in the surrounding of antennas is of great importance when considering resonant structures as elements for local enhancement of the electric field [Shelton *et al.*, 2011] [Shelton *et al.*, 2010a]. At the same time, this information provides an experimental test of the results given by computational electromagnetic packages.

Several detection techniques can be applied to better analyze the signals retrieved from the s-SNOM system. Among them, pseudo-heterodyne s-SNOM detection is effective for suppressing the background signal while providing a measurement of modulus and phase of the electric field component [Ocelic *et al.*, 2006]. In pseudo-heterodyne detection, the mirror of the reference beam oscillates and generates sidebands around the harmonics of the cantilever mechanical vibration frequency. These harmonics are background free and can be combined to obtain in a single scan both the amplitude and phase of the near field [Ocelic *et al.*, 2006] [Moreno *et al.*, 2017]. The main advantages of this approach is the capability to generate amplitude and phase measurements from a single scan, allowing faster and more reliable results that are not subject to mechanical drifting or the sample and tip wearing off over the measurement period.

s-SNOM techniques can also be used to obtain the electric and magnetic fields, as well as the current distribution maps in optical antennas and resonant structures [Olmon *et al.*, 2010] [Kinzel *et al.*, 2012]. To do that, it is necessary to customize AFM cantilevers to properly excite currents that respond to a variety of electric field orientations. The modified cantilevers are FIB-blunted tips that

are metalized with selective nanodeposition techniques to create a nanometric patch that scans the near-field distribution driving the cantilever in lift mode. In this configuration, the probe scans different locations of the field at various distances of the sample. The measured response is caused by the local electric field scattered by the modified tip (see Fig 5.16). From the retrieved signals obtained for two orthogonal electric field excitation vectors (*s* and *p*

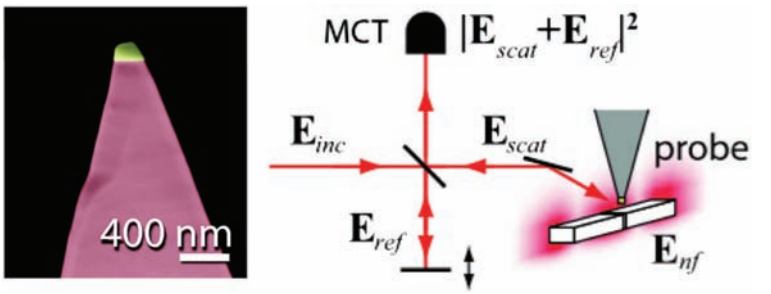

Figure 5.16 Left: A Si tip is modified by using focused ion beam (FIB) sculpturing to remove the tip and prepare a flat surface that is coated with metal (Pt). Right: The scattered electric field is combined with a reference beam using an interferometric homodyne technique. This operational mode is able to retrieve both the modulus and phase of the electric field. The illuminating field can be oriented along *s* and *p* polarizations, and the scattered field also can be selectively retrieved in polarization to finally obtain the electric field vector (adapted from [Olmon *et al.*, 2010] and reproduced with permission of APS).

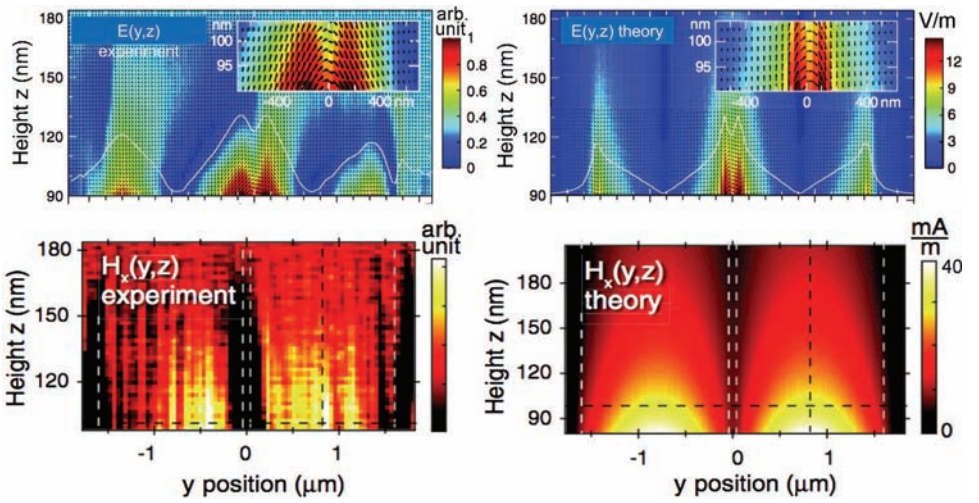

Figure 5.17 The modified tip is able to scatter the electric field from a dipole antenna having a nanometric gap at the feed point. The spatial dependence of two components of the electric vector at the axial plane of symmetry (upper row) is able to provide enough information to obtain the magnetic *H* field. The left maps are obtained from the experiment and the maps on the right are the results obtained from simulations (adapted from [Olmon *et al.*, 2010] and reproduced with permission of APS).

polarizations), it is possible to derive the magnetic field and the current distributions using Faraday's law [see Eq. (2.14)] and Hallen's integral equation for the given geometry of the resonant element [Hallen, 1956] [Balanis, 2005]. In other words, the spatial dependence of the electric field allows calculation of the magnetic field (Fig. 5.17) by means of the curl equation [see Eq. (2.3)]. Actually, the application of mirror symmetries in the resonant structure when considering the geometry and the relative position of the sample and the tip makes it possible to minimize the number of field scans applicable for each case. Therefore, a proper combination of the s-SNOM capabilities (including a coherent source and an interferometric homodyne signal detection technique) and a customized near-field probe tip resembles the operation of a radio-frequency vector network analyzer adapted to the optical range. Some more-sophisticated algorithms are of interest to ease data acquisition and generate better maps of the phase distribution of the field.

Chapter 6
Antenna-Coupled Detectors

6.1 Transduction Mechanisms in Antenna-Coupled Devices

Optical or infrared antennas are devices that receive optical radiation and transform it into a current within the resonant structure. This high-frequency current is transduced by a given mechanism to a change in voltage or current that is read by external electronics. From this point of view, optical antennas are light detectors.

Over time, several transduction mechanisms have been proposed and realized. One of the first used is the rectification of the currents flowing through the antenna by means of tunnel and Schottky junctions properly placed at the appropriate location, typically where the current density reaches the largest value. These elements are considered generically as diodes. Another simpler transduction mechanism is based on the heating of a bolometric material due to Joule dissipation. In this case, the mechanism is dissipative and needs electronic biasing to sense variations in resistivity of the bolometric element. It happens that most of the metals used in the fabrication of optical antennas have a similar value of the parameter responsible for the change in resistance with temperature, the temperature coefficient of resistance (TCR). Some designs use this effect to make the whole resonant element act as a bolometric transducer, which can be termed a distributed bolometer. Using the change in temperature caused by thermal dissipation of currents, thermoelectric transducers based on the Seebeck effect have also been proposed and tested. In this section we present the basic principles of these transduction mechanisms.

6.1.1 Diodes

Since the beginning of the use of radioelectric waves, rectification has been realized in different forms and using a variety of materials. Galena mineral and cat-whisker connections made the very first rectifiers used during the first quarter of the 20^{th} century. They were at the core of crystal radios used to tune, with limited performance, the amplitude-modulated wave emitted by radio stations.

In the case of infrared antennas, one of the first transduction mechanisms practically used were metal-oxide-metal junctions that worked as rectifying elements. Back in the 1970s, these junctions were demonstrated to rectify currents generated at metallic antennas for frequencies up to the infrared domain [Wiesendanger & Kneubühl, 1977] [Sanchez *et al.*, 1978] and even in the visible [Faris *et al.*, 1973]. Figure 6.1 shows several realizations of diodes coupled to antennas using different writing technologies, antenna designs, and materials. In this figure we can see how the surface quality and minimum feature size improved when switching from photolithographic techniques to electron-beam lithography [Esfandiari *et al.*, 2005]. When used for infrared rectification, MOM diodes require a fast response. Actually, tunneling mechanisms are fast enough to allow rectification through the junction. Although

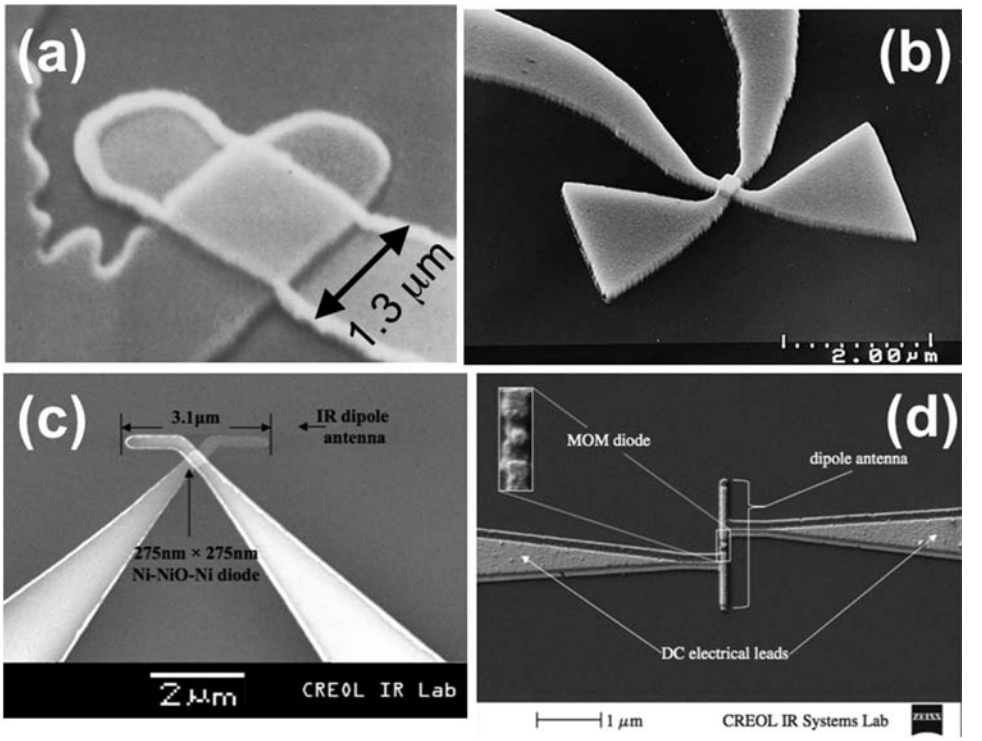

Figure 6.1 SEM micrographs of antenna-coupled MOM diodes. (a) A diode fabricated with photolithographic techniques and resonating at 337 μm having an area of around 1 μm^2 (adapted from [Wiesendanger & Kneubühl, 1977] and reproduced with permission of Springer). (b) A bow-tie antenna coupled to a Ni-NiO-Ni diode having a contact area of around 0.012 μm^2 and able to resonate at 10.6 μm (adapted from [Fumeaux *et al.*, 1998] and reproduced with permission of Elsevier). (c) A Ni-NiO-Ni diode coupled to a dipole antenna for 10.6 μm detection, and also connected to a slot antenna working at the millimeter-band region, 94 GHz (adapted from [Abdel-Rahman, 2004]). (d) An Al-AlO-Pt diode coupled to a dipole antenna (adapted from [Bean *et al.*, 2011] and reproduced with permission of IEEE).

definitive evaluation of the time constant for these MOM diodes is not straightforward, estimations supported by experimental results place this parameter in the range of 10^{-15} to 10^{-16} s, depending on the specific diode geometry [Fumeaux *et al.*, 1998].

Since the very beginning, some limitations were established relating to the cut-off frequency actually rectified by the junctions. Capacitance of the barrier was already considered as a critical parameter that, in the case of optical rectification, requires a very thin insulation layer, on the order of a few angstroms for a lateral size of a few hundreds of nanometers. When considering an equivalent circuit of the diode, this comprises a dissipative resistance, R, in series with a capacitance, C_d. In this case, the cut-off frequency is given as

$$\nu_{\text{cut-off}} = \frac{1}{2\pi R C_d}, \tag{6.1}$$

where C_d depends on the material and geometry properties of the junction as

$$C_d = \epsilon\epsilon_0 \frac{A}{d}, \tag{6.2}$$

where ϵ is the relative permittivity of the barrier, ϵ_0 is the electric permittivity of vacuum, and A are d are the transverse area and thickness of the junction, respectively. A higher cut-off frequency, $\nu_{\text{cut-off}}$, requires a very low capacitance. This low capacitance could be obtained by increasing the thickness of the insulating layer, but the currents would not be able to tunnel efficiently through the barrier and the device would become non-operational. Thus, thickness is mainly related to the tunnel junction characteristics and, for practical purposes, it should be limited to a very few tens of angstroms. Some proposals have been made to include a double insulator layer to increase responsivity and bandwidth [Rockwell *et al.*, 2007]. Therefore, once the insulator material is selected, fixing the value of ϵ, the only parameter left to reduce capacitance is the transverse area of the junction. Areas around 10^4 nm^2 corresponding to capacitances around 10^{-16} F are possible using e-beam lithographic techniques. From a practical point, an important advance was made when moving from lithography performed with optical masks [Wiesendanger & Kneubühl, 1977] to e-beam lithography [Wilke *et al.*, 1994] [Fumeaux *et al.*, 1998] [Rakos, 2006]. Besides the gain in minimum feature size and bandwidth, those metal depositions patterned with e-beam are smoother, and currents generated in the antenna dissipate less and reach the transducer better. In Fig. 6.1 we show some devices that include diodes as transducers. Metal-insulator-metal (MIM), metal-oxide-metal (MOM), or metal-barrier-metal (MBM) are names that have been used over time to refer to structures where tunneling of charge carriers is responsible for the rectified current. The successive advances in integration of MOM junctions

have made it possible to combine a collection of devices to form a working imaging element in the millimeter and far-infrared regions [Rutledge & Muha, 1982].

The direction of the current depends on the material characteristics of the metals of the junctions. For asymmetric MOM junctions, electrons flow from the metal having the highest Fermi level to the metal having the lowest. However, when the Fermi levels of the metals are equal on both sides of the junction, it is necessary to apply a bias voltage to select the direction of the current.

From a basic point of view, the MOM diode rectification mechanism can be understood by considering the energy diagram of two similar metallic electrodes separated by an oxide layer of thickness d, as shown in Fig. 6.2. At equilibrium, the two Fermi levels at each side of the barrier line up and there is a potential barrier of width d and constant height ϕ_0 above the Fermi level E_F. When a potential difference V_b is applied between the electrodes, the Fermi level of the positive-biased electrode moves down by qV_b, where q is the unit electronic charge. As a result, the potential barrier between the electrodes has a trapezoidal shape. The electrons above the Fermi level in electrode 1 have a higher probability of tunneling than the electrons from electrode 2. Therefore, the result of the application of the bias voltage is a net electron flow from electrode 1 to electrode 2.

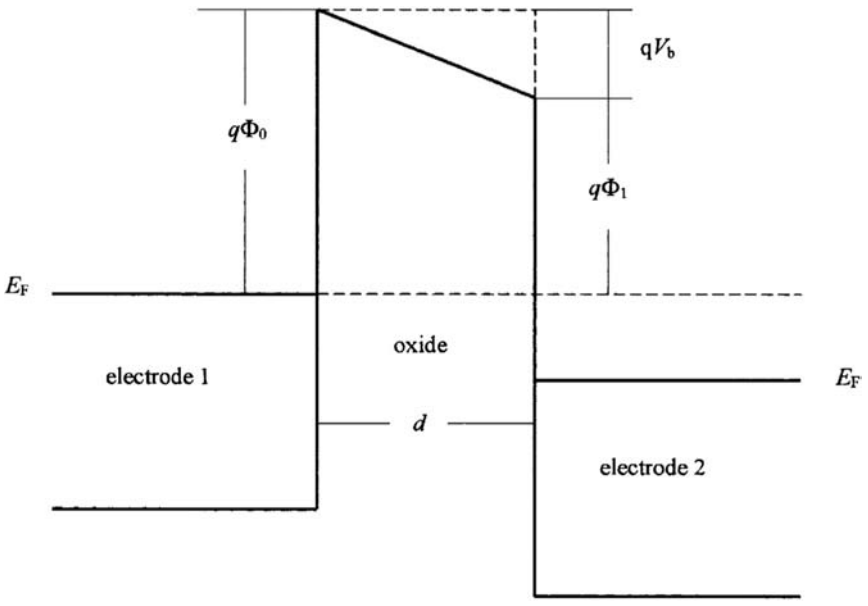

Figure 6.2 Energy band diagram at both sides of a MOM diode junction. The barrier has a width, *d*, corresponding to the insulator thickness (adapted from [Codreanu *et al.*, 2003] and reproduced with permission of Elsevier).

When the MOM diode is integrated with an antenna, the incident IR radiation induces a time-dependent "optical voltage" across the barrier, thus rapidly modulating the bias voltage. The total bias voltage across the barrier can be expressed as

$$V(t) = V_b + V_0 \cos(\omega t), \tag{6.3}$$

where V_0 is the amplitude of the induced voltage of angular frequency, ω, in the terahertz range.

When the induced voltage has the same polarity as the applied voltage, the separation between the Fermi levels is increased. As a result, the probability of an electron tunneling through the potential barrier increases, and the overall electrical current through the MOM structure increases. Following a similar reasoning, the overall electrical current passing through the diode decreases when the polarity of the induced voltage is opposite that of the applied voltage. Therefore, the MOM diode acts as a rectifier.

From an electrical point of view, MOM diodes are described by the characteristic I–V curve

$$I = \frac{AqV^2}{4\pi h\phi_0 d} \exp\left(- \frac{8d\sqrt{\pi q \phi_0^3}}{3V} \right), \tag{6.4}$$

where ϕ_0 is the height of the tunnel barrier, q is the charge of the electron, h is Planck's constant, and A and d are the transverse area and the thickness of the junction, respectively. To obtain a simpler relationship between the amplitude of the rectified current, I_r, and the amplitude of the induced optical voltage, V_0, a Taylor-series expansion of the total current, $I(t)$, with respect to the total bias voltage, $V(t)$, is performed. The magnitude of the rectified current is related to the amplitude of the induced voltage by the following equation:

$$I_r = \frac{1}{4} \left(\frac{d^2 I}{dV^2} \right)_{V_b} V_0^2. \tag{6.5}$$

The rectified current is proportional to the square of the induced voltage and therefore to the power of the incident radiation. Hence, the MOM diode acts as a square law detector. The proportionality constant is determined by the second derivative of the I–V characteristic curve of the diode, evaluated at V_b. The detector response is obtained by extracting the change in the bias voltage produced by the optical radiation with respect to the bias voltage set by the external biasing electronics. Then, the output signal is obtained by multiplying the rectified current by the electrical resistance of the detector,

$$V_{\text{out}} = RI_r, \tag{6.6}$$

where R is the electric resistance at the bias voltage, V_b. This resistance is equal to the inverse of the first derivative of the I–V curve at V_b. From this analysis we can conclude that

$$V_{\text{out}} \propto \frac{\left(\frac{d^2I}{dV^2}\right)_{V_b}}{\left(\frac{dI}{dV}\right)_{V_b}} = \frac{I''_{V_b}}{I'_{V_b}}. \tag{6.7}$$

This ratio between derivatives is also denoted as the sensitivity of the diode. The validity of this approach can be seen in Fig. 6.3.a. To have a more sensitive element, it is important to maximize the nonlinear response of the device (value of the second derivative) and minimize the DC resistance appearing at the bias voltage. When limiting the operational range to low biasing voltages, an estimation of the first derivative appearing in Eq. (6.7) can be given as the resistance when $V_{\text{bias}} = 0$ V. This resistance depends on the tunnel barrier, the resistivity of the metal, and the transverse area of the junction (larger transverse area gives lower resistance). Typical measurements of this resistance produce values between several tens of ohms and a few thousand [Fumeaux *et al.*, 1998] [Bean *et al.*, 2011].

This detection mechanism is fundamentally different from the bolometric effect considered in the next section. This can be seen in Fig. 6.3.b, where the I–V curves for two different devices are compared. Both elements are coupled to a dipole antenna having a length of 1.8 μm. One of the devices shows only a thermal detection mechanism (bolometric effect), and the other

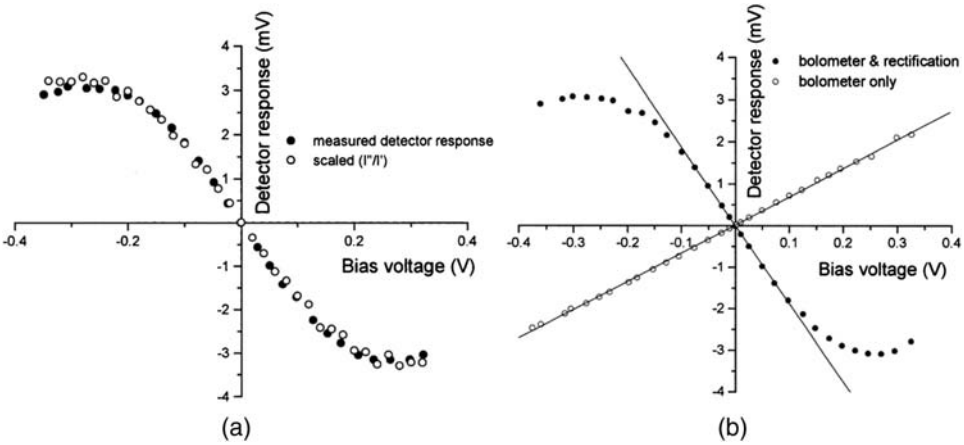

Figure 6.3 I–V curves for antenna-coupled devices. (a) Plot of the I–V characteristics comparing two detection mechanisms: MOM rectification + bolometric, and bolometric-only effect. Rectification produces a nonlinear behavior, while the bolometric effect has a simpler linear dependence. (b) Comparison between the actual response of a fabricated antenna-coupled device working as a MOM rectifier and the I''_{V_b}/I'_{V_b} ratio described in Eq. (6.7) (adapted from [Codreanu *et al.*, 2003] and reproduced with permission of Elsevier).

produces a response where the bolometric response is combined with rectification through a MOM junction. The I–V characteristic of bolometric devices is linear, while the I–V characteristic of the devices exhibiting both detection mechanisms has a cubic dependence on the bias voltage [Codreanu *et al.*, 2003].

An interesting option for current rectification without tunneling through a thin oxide layer appeared when considering the capability of charge carriers to move through barriers with geometries properly designed to work better in one direction than another [Büttiker, 1986]. This capability is called geometric rectification and has been proved and tested in geometric diodes and transistors made of semiconductors [Song *et al.*, 1999] [Song, 2002] [Song *et al.*, 2004] and metals [Choi *et al.*, 2010], and was also shown in ballistic or classical transport through junctions [Fleischmann & Geisel, 2002] [de Haan *et al.*, 2004] [Dragoman & Dragoman, 2013]. However, when moving to optical frequencies, the same limitations in cut-off frequency appear due to capacitive effects, and the same solution in geometries needs to be applied. To overcome these issues, some alternatives have been proposed and realized, which combine geometries and 2D materials such as graphene [Moddel *et al.*, 2012] or carbon nanotubes [Sharma *et al.*, 2015]. A review of this topic is presented in Chapter 10 of [Moddel & Grover, 2013]. Figure 6.4 shows several designs corresponding to semiconductors, metal and Si-polycrystalline tips, and graphene geometric diodes and devices.

6.1.2 Bolometers

Those first antennas working at infrared frequencies were mostly coupled to Nb microbolometers [Neikirk *et al.*, 1982] [Grossman *et al.*, 1991]. The reason for this choice is related to the easier fabrication of microbolometers compared to diode transducers. However, this physical mechanism is dissipative in nature and requires external biasing to produce a signal.

The bolometric effect accounts for the change in resistivity, $\Delta\rho$, of a material when exposed to a change in temperature, ΔT. When the change in temperature is small, the relation can be linearized and written as

$$\Delta\rho = \alpha\rho\Delta T, \tag{6.8}$$

where α is the temperature coefficient of resistance (TCR) of the material. This coefficient shows the relative change in resistivity per degree and is positive for metals and negative for semiconductors. Most metals have a value of around $\alpha = 0.004\ \mathrm{K}^{-1}$, nickel showing the largest value of $\alpha_{\mathrm{Ni}} = 0.006\ \mathrm{K}^{-1}$ [Palik, 1997]. This is the reason that Ni is often selected as the material to fabricate microbolometers at the feed point of antenna-coupled bolometric detectors. The temperature rise caused by the incident radiation induces a change in the electrical resistance of the bolometer. Therefore, a bolometer is a thermal detector, sensing a change in its overall temperature.

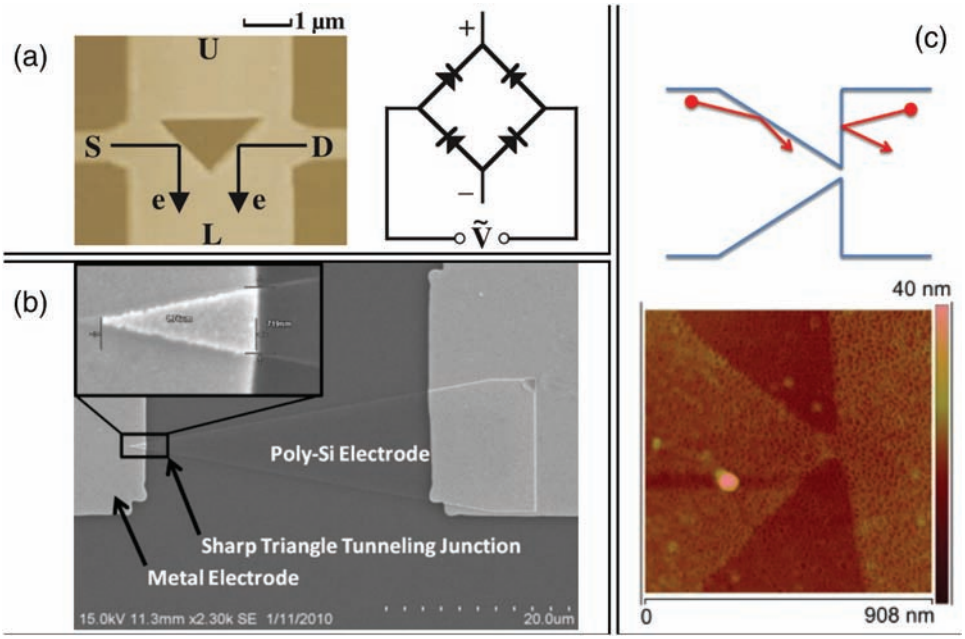

Figure 6.4 (a) A semiconductor structure that works as a full wave rectifier at gigahertz frequencies (adapted from [Song, 2002] and reproduced with permission of Springer). (b) An asymmetric tunnel diode where the geometry enhances the rectification for a MOM junction (adapted from [Choi *et al.*, 2010] and reproduced with permission of AVS). (c) The working principle and the practical realization of a geometric diode at optical frequencies made of graphene (adapted from [Moddel *et al.*, 2012] and reproduced with permission of Elsevier).

From a physical point of view, the process is simple: an electromagnetic wave builds up currents in a metallic resonant structure. Part of the energy carried by these currents dissipates as heat [see Eq. (2.11)]. This heat changes the temperature of the device, and this variation of temperature changes the resistivity and therefore the resistance of the element under analysis.

This simple picture needs a multiphysics perspective to implement numerical calculations. Electromagnetic, thermal, and electric circuit domains are necessary to properly model and understand the phenomena. From the electromagnetic basics presented in Chapter 2, we need only the Joule dissipation that will act as a heat source. The total power dissipated in a given volume, v, is

$$Q = \int_v q(x,y,z)dv = \int_v \sigma|\vec{E}(x,y,z)|^2 dv, \tag{6.9}$$

where σ is the electric conductivity. The thermal transport applicable to this case involves the heat transfer equation:

$$\frac{\partial T}{\partial t} C_p d = \nabla(\kappa \nabla T) + q, \tag{6.10}$$

where the material under analysis is characterized by its heat capacity, C_p, mass density, d, and thermal conductivity, κ. The connection to the electromagnetic domain is through q, which represents the power dissipated through Joule heating in Eq. (6.9). The result of computations will be a temperature map that accounts for the temperature distribution caused by the incident optical radiation [Cuadrado *et al.*, 2012a] [Cuadrado *et al.*, 2012b] [Cuadrado *et al.*, 2013a]. Some temperature maps obtained for bolometric devices are shown in Fig. 6.5. Some typical materials used to fabricate bolometers are Nb and VO_x, where vanadium oxide bolometers have a better response than niobium ones [González *et al.*, 2003].

Depending on the wiring and on-chip connection of the resonant element to the external circuit, we may find that the bias current needs to go through a given path with different materials and temperatures. To make this practical, it is a good strategy to describe the temperature profile along those paths where the biasing current flows. Then, the change in resistance is given as

$$\Delta R = \int_L \frac{\rho(l)\alpha(l)\Delta T(l)}{S(l)} dl, \tag{6.11}$$

where l denotes the location on line L along the biasing current path. Due to the multiphysics chain of phenomena, $\Delta T(l)$ will be a continuous function along L, and the dependence of $\alpha(l)$ and $\rho(l)$ on l denotes the possibility of having different materials along path L (see Fig. 6.5). By using this formalism, it is possible to model antenna devices coupled to nanobolometers, and to distributed bolometers, where the bolometric effect is produced along the

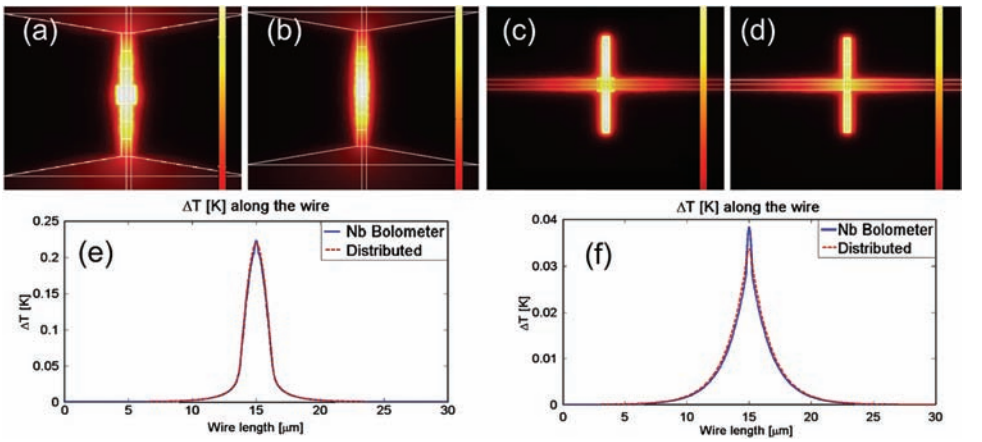

Figure 6.5 Temperature maps for a dipole antenna (a) and (c) coupled to a Nb nanobolometer, or (b) and (c) working as a distributed bolometer. In configurations (a) and (b), the antenna belongs to the lead line, and in configurations (c) and (d), it is orthogonal. (e) and (f) The temperature profiles that should be included in Eq. (6.11) for these geometries (adapted from [Cuadrado *et al.*, 2012a] and reproduced with permission of SPIE).

whole resonant structure. Also, an appropriate choice of the geometry, materials, and auxiliary elements can optimize the performance of these devices [Cuadrado *et al.*, 2013b] [Cuadrado *et al.*, 2013a] [Slovick *et al.*, 2010]. This distributed bolometric case is of interest because its fabrication does not require two steps of e-beam lithography involving strict alignment constrains. From the temperature maps in Fig. 6.5 we may verify that the temperature distribution is about the same for those devices using a microbolometer at the antenna feed-point as for the distributed bolometer case.

Bolometric transduction is thermal in nature, and this characteristic makes these devices slower than diodes. However, the longer response time of antenna-coupled bolometers with respect to the diode counterpart is much shorter than that of classical or macroscopic bolometers. An evaluation of this response provides a value of a few milliseconds, allowing modulations of some hundreds of hertz [Cuadrado, 2014].

6.1.3 Thermoelectric

Thermoelectric transduction is mainly based on the Seebeck effect, which transforms a temperature gradient into a voltage difference. The temperature difference is established between two material junctions. Because this effect is reversible, it has been widely used to control the temperature in active heating/cooling systems. When used for light detection, the detectors are known as thermopiles. Classical bolometers and thermopiles are relatively bulky and slow detectors. However, when optical antennas are used, a low thermal inertia is associated with the tiny volume, making a more favorable device performance compared to their macroscopic counterparts.

The basic principle is quite simple. An antenna structure is coupled at the location of a junction between two thermoelectric materials. This junction will be the hot junction of the thermopile (at temperature T_H). These materials are part of a thermoelectric circuit that contains another junction at a colder temperature T_C. The reading circuit will extract the Seebeck open-circuit voltage, V_{OC}, caused by the difference in temperature. This voltage is given as

$$V_{\mathrm{OC}} = (S_A - S_B)\Delta T, \tag{6.12}$$

where $\Delta T = T_H - T_C$, and S_A, S_B, are the Seebeck coefficients of the materials used in the thermocouple.

Significant interest has been shown for this type of detector because it provides a signal without requiring biasing elements. Since the first results were obtained in 1998 [Fu, 1998], some progress has been made in the analysis and realization of Seebeck nanoantennas [Krenz *et al.*, 2012] [Szakmany *et al.*, 2012] [Szakmany *et al.*, 2014a] [Szakmany *et al.*, 2014b] [Briones *et al.*, 2014b] [Briones *et al.*, 2014a]. By using this transduction mechanism and combining these structures, it seems possible to build optical-antenna arrays that provide

a signal directly related to the Stokes parameters of the incoming radiation [Cuadrado *et al.*, 2014a]. The idea is to place (at the two junctions of the thermocouple) two antennas that respond to orthogonal polarizations, for example, horizontal and vertical. In this case, when a given irradiance polarization state illuminates this antenna arrangement, it will differentially heat this antenna pair, producing a signal proportional to the difference in power associated with each of the selected polarization states (see Fig. 6.6).

A solution quite similar to the distributed bolometric case uses a single metal to generate both hot and cold junctions through geometry [Szakmany *et al.*, 2017]. This geometry-induced Seebeck effect is a very promising way of making thermoelectric transduction simpler for both fabrication and modeling (see Fig. 6.7).

6.2 Phased-array Antennas and Transmission Lines

Phased-array antenna configurations hold promise for synthesis of narrow-angle-of-arrival reception for infrared sensors. As with all phased-array antennas, the more antennas that can be combined in phase the narrower the angular response [Middlebrook *et al.*, 2008a] [Slovick *et al.*, 2011a]. The limitation for infrared antennas is the loss of the transmission lines used to

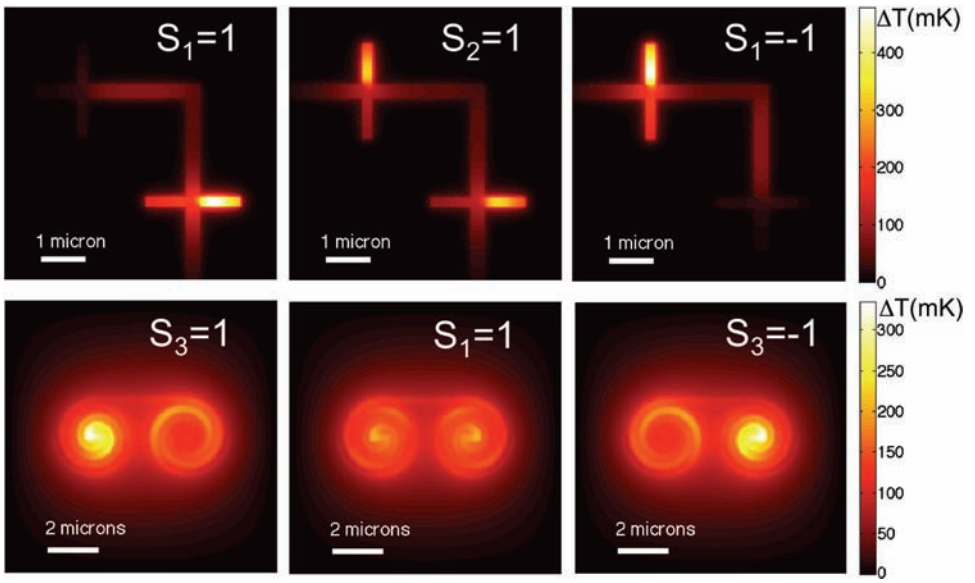

Figure 6.6 Map of temperature produced when incident light has a pure state of polarization given by several Stokes parameters. The dipole configuration (top) is strongly selective for horizontal ($S_1 = 1$) and vertical polarization ($S_1 = -1$). The bottom configuration is composed of counterrotating spiral antennas that are strongly selective to right-hand circular polarization, dextro ($S_3 = 1$), and left-hand circular polarization, levo ($S_3 = -1$) (adapted from [Cuadrado *et al.*, 2014a] and reproduced with permission of OSA).

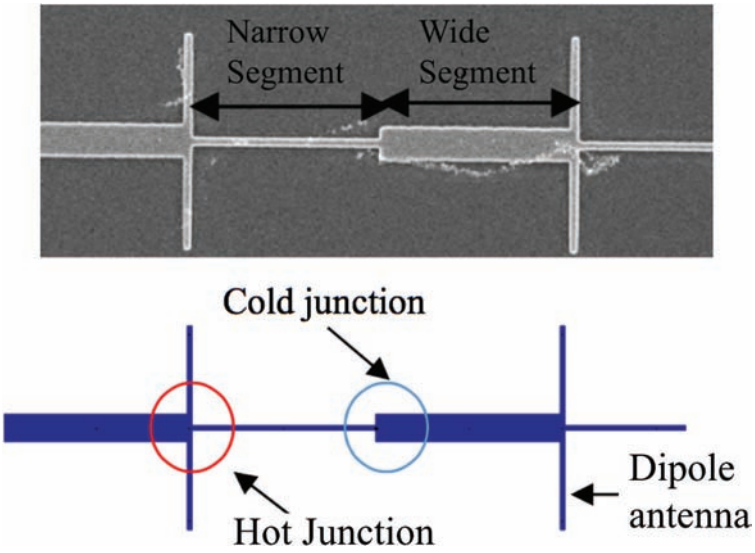

Figure 6.7 Schematics of a dipole antenna working as a thermoelectric transducer and fabricated using a single metal structure. The hot and cold spots are defined by a change in the geometry of the lead lines. The hot spot is coupled to a dipole antenna (adapted from [Szakmany *et al.*, 2017] and reproduced with permission of Elsevier).

combine the antenna signals [Mandviwala, 2006]. Wire transmission lines provide field confinement in much smaller volumes than do dielectric transmission lines, allowing compact on-chip routing for the infrared-frequency current waves. In the infrared, either co-planar strip lines [Mandviwala *et al.*, 2005] or microstrip lines [Mandviwala *et al.*, 2008] have characteristic impedances of a few hundred ohms and hence are a good match to planar antennas; however, at the present stage of development, their relatively high attenuation limits the number of antennas that can be usefully interconnected. In the development of phased-array antennas, it is important to distinguish between phase-incoherent and phase-coherent interconnections. A collection of antennas can be arranged close together and connected in series to make a larger sensitivity area, or a pixel of a focal plane array [González *et al.*, 2004a] [González *et al.*, 2005] [Mandviwala *et al.*, 2005] [Mandviwala *et al.*, 2006] [Silva-López *et al.*, 2013]. Figure 6.8 shows this situation for dipole and bow-tie antenna-coupled bolometers. In these cases, the signal from each bolometer is combined. This type of interconnection does not preserve the phase information from each antenna, since the current waves from each individual antenna are dissipated in the corresponding bolometric load.

In contrast to this situation, a phase-coherent combination of current waves is accomplished using the configuration seen in Fig. 6.9. In this case, the current waves from each antenna are propagated along the co-planar strip transmission lines and are combined with phase delay corresponding to their

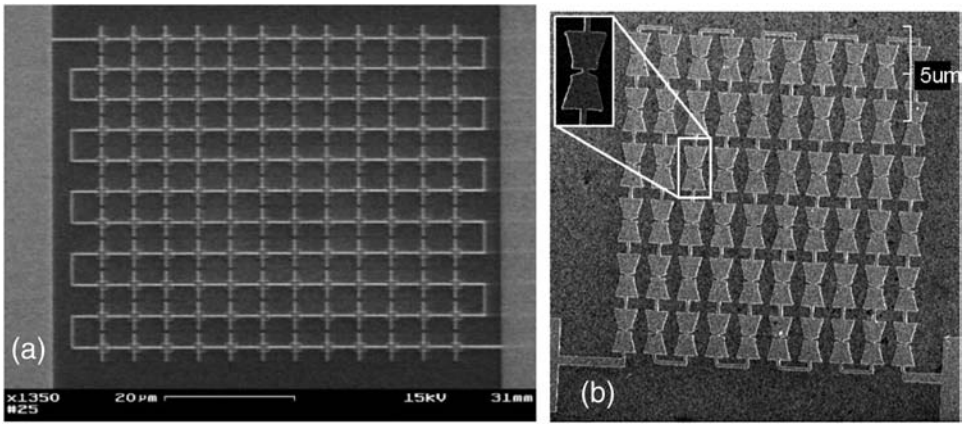

Figure 6.8 (a) An array of dipole antennas coupled to Nb microbolometers and (b) an array of aluminum bow-tie antennas working as a distributed bolometer combine their signals, losing the phase information between resonant elements (adapted from [González *et al.*, 2004a] and [Silva-López *et al.*, 2013], and reproduced with permission of Elsevier and OSA).

respective propagation length at the location of the single sensor (in this case, a MOM diode). The transmission line needs to be short enough to compensate the high loss in propagation [Krenz *et al.*, 2010a]. As seen in Fig. 6.9, going from one antenna to two, four, and six added in phase narrows the angular response in reception. However, a diminishing returns is noted in that the angular response of the six-element phased array is not significantly narrower than that of the four-element array because of the transmission-line attenuation.

The relative phase delay with which various contributions are added determines the look angle of the phased-array antenna. The simplest way to demonstrate this is to offset the sensor from the equal-phase position at which it will have maximum response at the broadside of the array. Figure 6.10 [Slovick *et al.*, 2011a] shows an off-broadside response for the situation where the sensor is located such that the current waves from opposite antennas do not add in-phase.

Given the development of low-loss infrared transmission lines with good field confinement properties, phased-array infrared antennas with many participating antenna elements should be able to synthesize a very narrow angular response. These may offer the prospect of lensless imaging, which would be of interest, especially on ultra-small platforms to give rudimentary vision capabilities in a compact form factor. If phase modulators of sufficient temporal bandwidth become available to support infrared-frequency phase shifting, it may be possible to integrate these directly into the transmission lines to achieve one-dimensional (1D) look-angle variation as the inter-element phase is changed. This would be an infrared analog of an electronically scanned array. An alternative configuration would be a set of non-tunable phased arrays on one chip, each with a slightly different look angle. A pair of

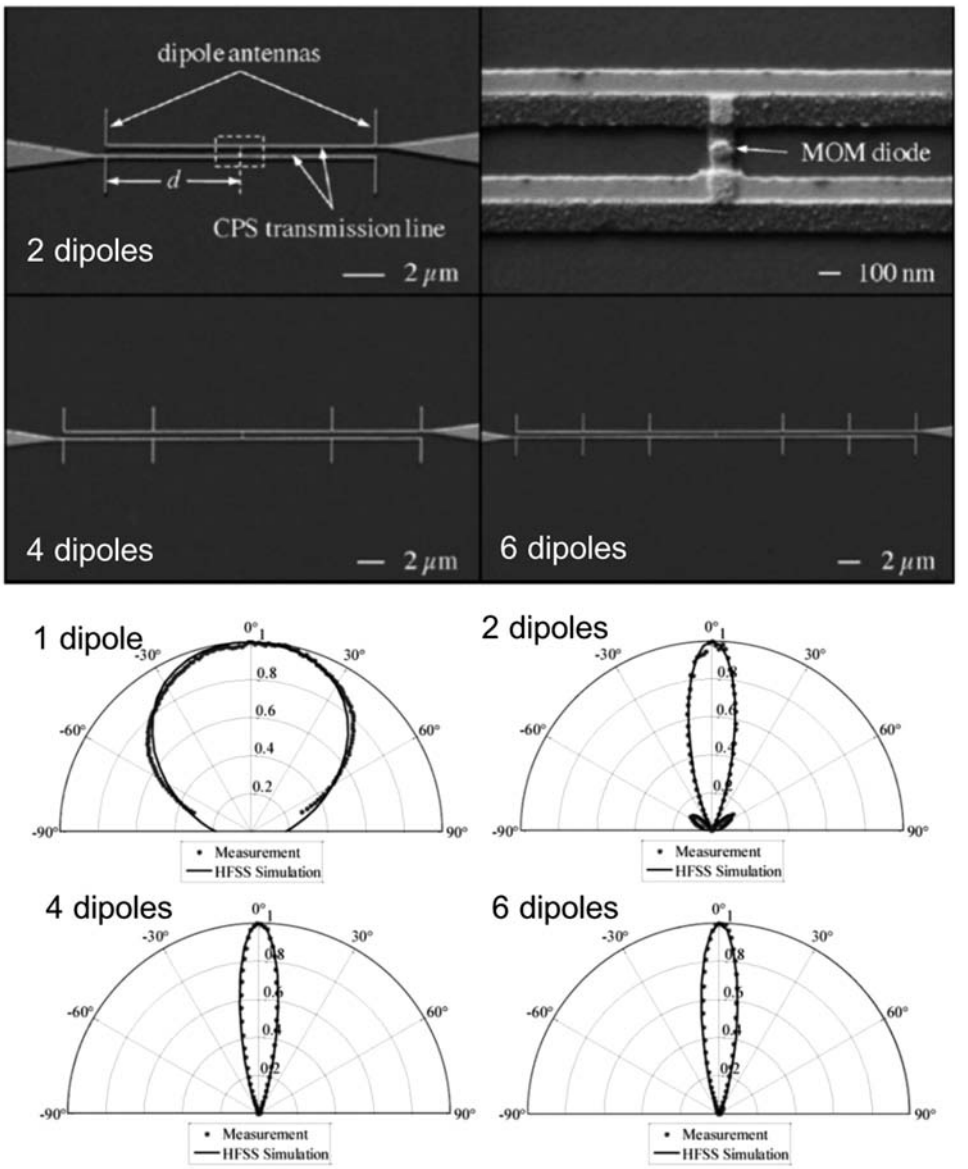

Figure 6.9 An array of several dipoles along the same coplanar strip (CPS) transmission line combine their signals onto a single transducer located at some point along the transmission line. The angular pattern narrows as the number of elements in the array is increased (adapted from [Slovick *et al.*, 2011a] and reproduced with permission of IEEE).

dipole antennas can be also used to combine radiation and is able to measure, in a manner similar to Michelson stellar interferometry, the coherence function of light sources [Middlebrook *et al.*, 2008b] and to perform wavefront sensing [Yang *et al.*, 2008].

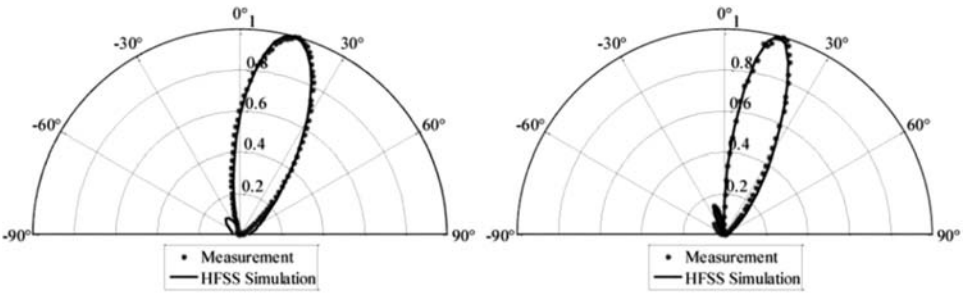

Figure 6.10 When the transducer location along the transmission line changes (see Fig. 6.9), the traveling signals combine in different positions, steering the direction of reception accordingly. This figure describes the angular response pattern for a two-element array and a 0.9 μm diode shift (left), and a four-element array with a 1.5 μm diode shift (right) (adapted from [Slovick *et al.*, 2011a] and reproduced with permission of IEEE).

6.3 Rectennas and Energy Harversters

Section 6.1 was devoted to the analysis of high-frequency diodes in the transduction of a signal for an infrared antenna. Rectification mechanisms have been typically supported by Schottky-type junctions across insulation layers between two metals [Fumeaux *et al.*, 1998] [Eliasson, 2001] [Bean *et al.*, 2011]. This type of transduction is actually forwarding charge carriers along a selected direction defined by an external biasing voltage, or by the difference in the work functions of two different metals across the junction of the diode. This makes possible the generation of an electric current from the high-frequency oscillations of the external electric field incident on the device. This property is also interesting from an energy-harvesting perspective and has been of interest for some time. Antennas coupled to rectifiers are denoted as optical rectennnas. Several studies and reports have emphasized the capabilities of rectennas in the collection and generation of electric energy from optical radiation [Berland, 2003] [Corkish *et al.*, 2002] [Kotter *et al.*, 2010] [Vandenbosch & Ma, 2012] [Abadal *et al.*, 2013] [Moddel & Grover, 2013] [Sarehraz, 2005]. From a simplified point of view, optical rectennas are the adaptation to the optical range of rectennas working in the radioelectric and microwave portion of the spectrum. However, as we have already seen, the presence of plasmon resonances and the special behavior of metals at optical frequencies require close attention to cope with the limitations given by materials and geometries.

Junction diodes are very well suited for the rectification of currents in the radioelectric and microwave regions. Back in the 19th century, Tesla envisioned the capability of electromagnetic waves to transmit energy between two locations. Some other attempts at this were made during the 20th century. These began to produce positive results when microwave radiation was used for energy transport [Brown, 1984] [Hagerty *et al.*, 2004].

In the past decade, the dense distribution of radioelectric sources in the environment has shifted attention to the scavanging of those bands, producing elements able to retrieve energy from the radioelectric environment [Kurs *et al.*, 2007]. These technologies are based on rectifying diodes fabricated in printed circuits and reaching efficiencies of around 85%. The capacitance of the diode at microwave frequencies does not need to be ultra-low, and the dimensions of the junctions (area and thickness) are feasible. However, at optical frequencies, working diodes are hard to fabricate and require deposition technologies with high lateral resolution to evaporate layers tens of angstroms in thickness. Moreover, the cut-off frequency [Eq. (6.1)] is strongly dependent on the diode capacitance, C_d, while the efficiency of the rectification also depends on the nonlinearity of the I–V curve [see Eq. (6.7)]. Therefore, by considering realistic values of these parameters, the efficiency of MIM diodes is around 10^{-6} (the efficiency is given as the ratio between DC rectified power and the AC optical power arriving to the device). This low efficiency combines with the losses arising from impedance mismatch between the antenna and the diode. This impedance mismatch is responsible for another multiplicative factor of around 10^{-3} [Briones *et al.*, 2013]. Some other analyses using photon-assisted tunneling models predict efficiencies well above the previous figures, reaching percentages larger 44% at the diode level [Moddel & Grover, 2013] for a polychromatic illumination on an ideal diode. The large discrepancy between these values is mainly due to the conditions used for each calculation. The most optimistic figures are mostly calculated for ideal conditions where impedance-matching problems are solved and rectification efficiency is not an issue. These efficiency figures may indicate a promising future for the practical use of rectennas in solar energy photovoltaics.

Other proposals for improving rectification efficiency have been made. One quite interesting device is based on the rectification being distributed along a waveguide that also acts as a diode. In this case (see Fig. 6.11), the wave traveling along a waveguide is progressively rectified when propagating [Grover *et al.*, 2010].

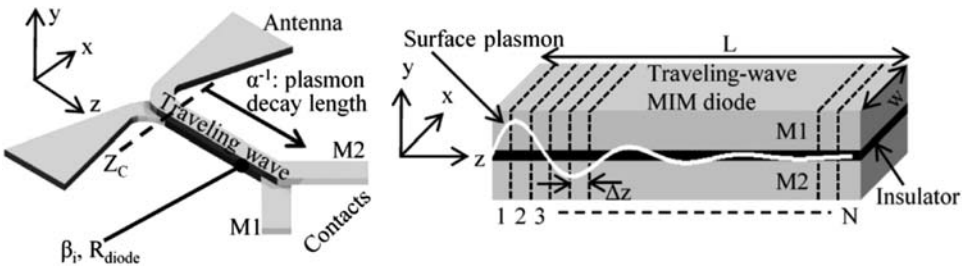

Figure 6.11 The MIM rectifying junction is distributed along a waveguide. By doing this, rectification is achieved over a longer distance with better efficiency (adapted from [Grover *et al.*, 2010] and reproduced with permission of IEEE).

Another very interesting option for an alternative rectification mechanism is the geometrical rectification that happens when ballistically moving charge carriers interact with a potential barrier linked to the geometry of the system [Fleischmann & Geisel, 2002] [de Haan *et al.*, 2004] [Song *et al.*, 2004]. This mechanism requires high mobility and a free-mean-path longer than the physical dimensions of the rectifier. Two-dimensional materials such as graphene have been proposed for this task [Zhu *et al.*, 2013]. Figures 6.4.a and 6.4.c show some elements working in the microwave and optical spectrum.

Chapter 7
Resonant Optics

The general class of devices called resonant optics is periodic or quasi-periodic and consists of metallic unit cells arranged in a 2D array on a dielectric substrate. We generally used 2D structures in our investigations, with multilayer structures used on occasion. Some embodiments used metallic ground planes and some did not, restricting or allowing their use in reflective or transmissive modes. In this chapter we describe three subclasses of device architectures: frequency-selective surfaces (FSSs), optical retarders, and reflectarrays.

7.1 Frequency-Selective Surfaces

Initial FSS designs were guided by general principles borrowed from circuit theory and electrical engineering concepts [Munk, 2000]. This approach treats FSS designs as RLC circuits, which is a useful perspective when starting a design. The metal structures are resistive; the straight and folded conductors are inductive; and the gaps between adjacent conductors give rise to capacitance. The resonant wavelength and spectral bandwidth of the FSS are controlled by the geometry of the periodic metallic structures [D'Archangel *et al.*, 2014a] [Puscasu, 2001] [Schaich *et al.*, 2003]. Computation and optimization of detailed designs were accomplished with periodic method of moments or finite-element techniques. Figure 7.1 shows how a variety of unit cells may be implemented.

Frequency-selective surfaces without a ground plane can be designed as band-transmit or band-reject filters, a diagram of which can be seen is Fig. 7.2.a. In general, an array of metallic elements will act as a band-reject filter, reflecting radiation in a narrow band of wavelengths, and transmitting radiation outside of that band. In addition, the choice of the metallic material changes the central frequency and bandwidth according to the material properties, especially conductivity. This is shown in Fig. 7.3 for a crossed FSS made with different metals [Ginn *et al.*, 2009]. Conversely, an array of slots in a metallic surface will act as a band-transmit filter, passing radiation as a narrow band of wavelengths and reflecting the rest of the incident radiation.

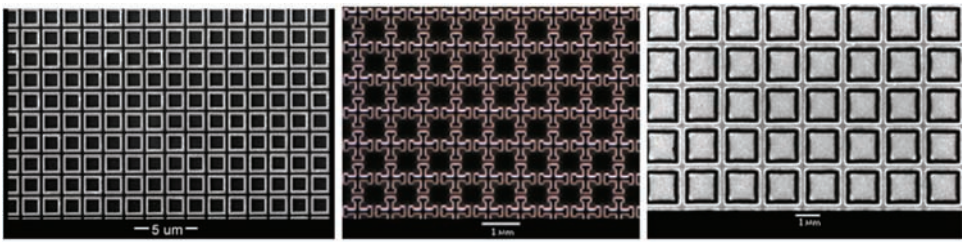

Figure 7.1 Three different geometries of squares (left), Jerusalem crosses (center), and slotted patches (right) are able to modify the spectral content of the reflected light (adapted from [Monacelli, 2005]).

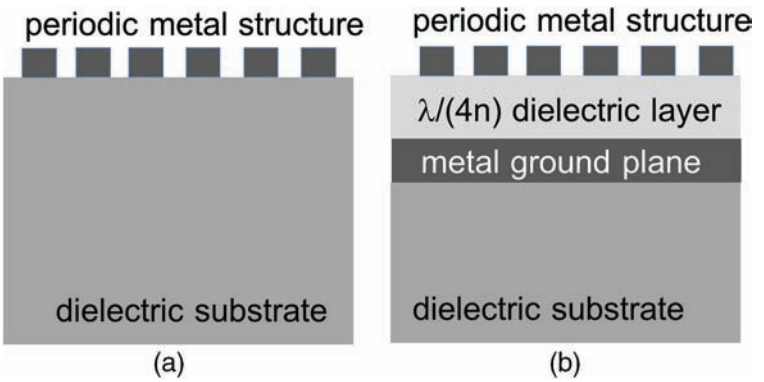

Figure 7.2 (a) An FSS is written on a dielectric substrate that could be transparent to make possible a transmissive FSS. (b) When using a ground plane, the FSS becomes reflective and as such is typically used to modify the emissivity of the supporting surface.

These two examples are shown in Fig. 7.4. There is necessarily some loss caused by absorption in the metallic structures that somewhat changes the resonance. The starting designs for these spectral filters are scaled versions of similar devices in the radiofrequency band. An initial estimate can be made of the resonance wavelength by evaluation of the primary resonance dimension of the unit cell (e.g., circumference for a loop, half wavelength for a dipole), taking into account the effect of the substrate's refractive index [Puscasu *et al.*, 2002] [Puscasu *et al.*, 2000b] [Puscasu *et al.*, 2001].

Usually, in the visible and near IR, such filtering functionality can be achieved with lower loss by using thin-film interference filters. However, in the far-infrared and terahertz bands, these films become quite thick, possibly resulting in adhesion problems. In these cases, a FSS band-pass or band-reject filter is a desirable solution [Monacelli, 2005] [Shelton *et al.*, 2008a].

With inclusion of a metallic ground plane and a quarter-wave stand-off layer (see Fig. 7.2), an IR FSS can be configured to produce a wavelength-selective absorber. The ground plane thickness should be sufficient to eliminate any

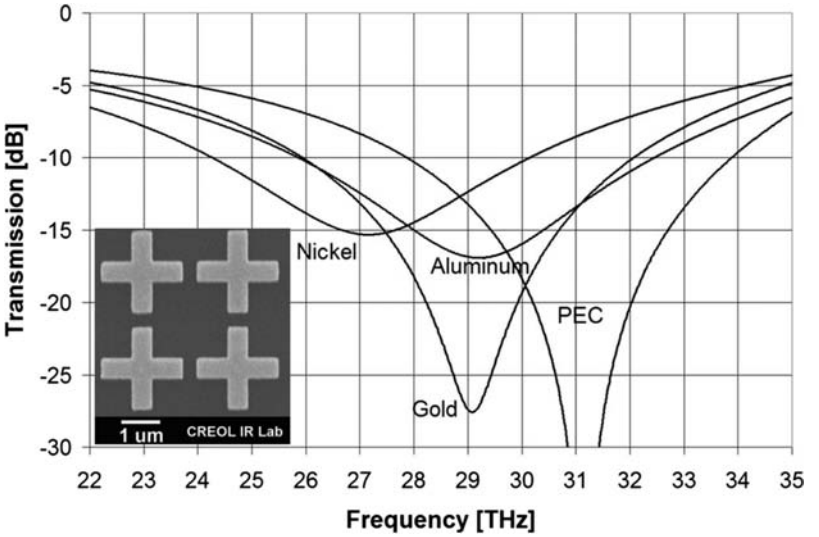

Figure 7.3 Modeled transmission of four cross metamaterial arrays made of three different metals and perfect electric conductor (PEC) material. The inset shows the fabricated crosses (adapted from [Ginn *et al.*, 2009] and reproduced with permission of AIP).

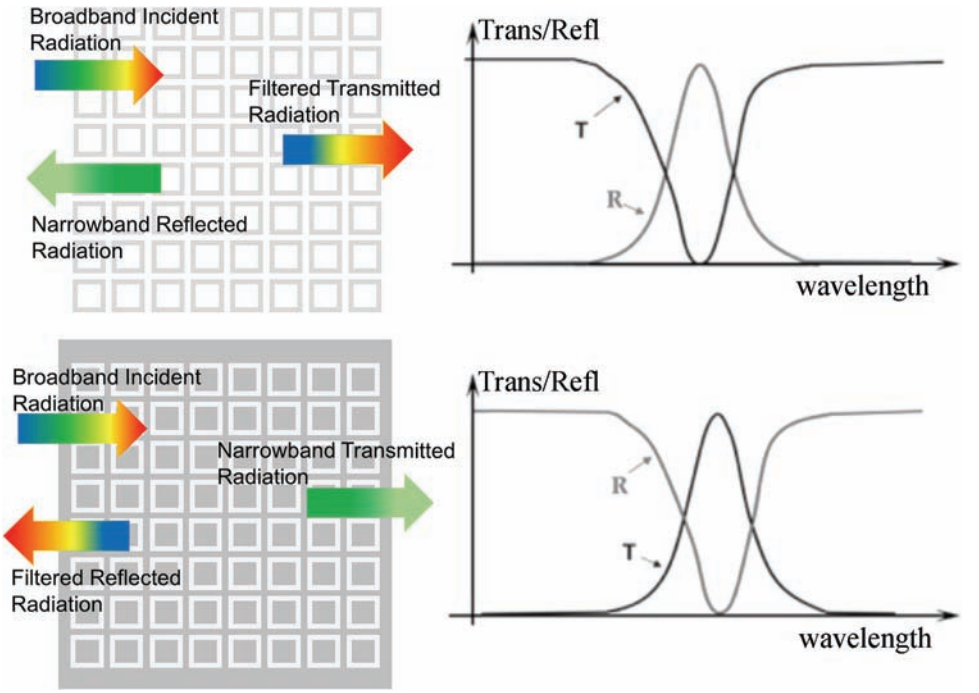

Figure 7.4 Two complementary geometries produce complementary spectral behavior for the reflection and transmission spectra (adapted from [Monacelli, 2005] and [D'Archangel, 2014]).

appreciable transmission (a few skin depths). Because of Kirchhoff's law, the ability to control the spectral absorption is equivalent to controlling the spectral emissivity. This allows emissivity to be set high or low in predetermined wavelength regions.

A single-layer selective-absorber FSS with a simple unit cell (single strong resonance) will have a simple RLC response with a given spectral location and width, so the spectral dependence cannot be controlled in arbitrary detail. Along with the unit cell spacing and geometry, the thickness and the refractive index of the stand-off layer are additional variables in the design. In Fig. 7.5 measured data show that the modulation of the emissivity is strong, ranging from 10% to over 95%. Additional complexity in the spectral response may be generated by additional FSS layers, the use of unit cells with multiple resonances, overcoat layers, or exploitation of absorption bands of constituent materials. It should be noted that any radiation that is not absorbed is reflected, and thus the selective-absorber FSS will have a metallic visual appearance unless overcoated.

As a demonstration of the potential of an IR FSS for emissivity control, Fig. 7.6 shows three different metallic unit cells (Jerusalem cross, square loop, patch) designed for high, medium, and low emissivity in the 8–12 μm band. The model, the emissivity spectrum, and the fabricated devices are shown in Fig. 7.6. Once the individual designs demonstrated their expected spectral behavior, these elements were arranged on a 3-inch Si wafer in a typical random pattern (see Fig. 7.7).

Fabrication of test FSS structures is generally performed with direct-write e-beam lithography to achieve the spatial resolution specified in the design

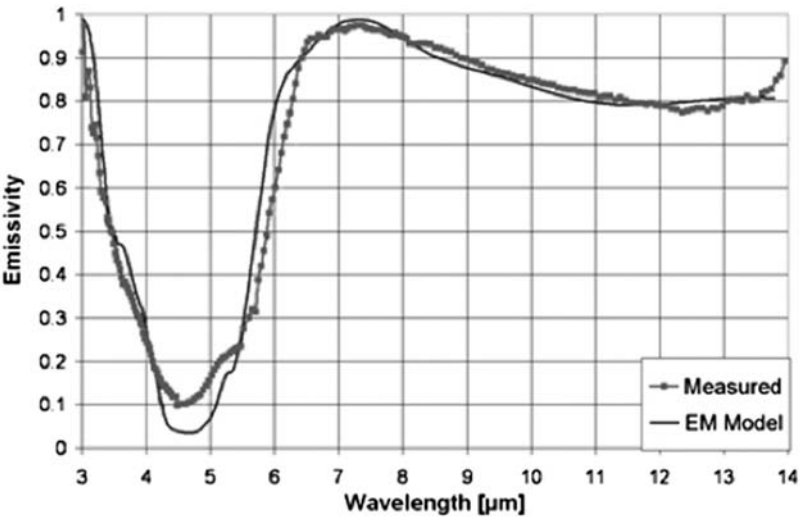

Figure 7.5 Spectral emissivity of an FSS having a simple unit cell (adapted from [Ginn, 2009]).

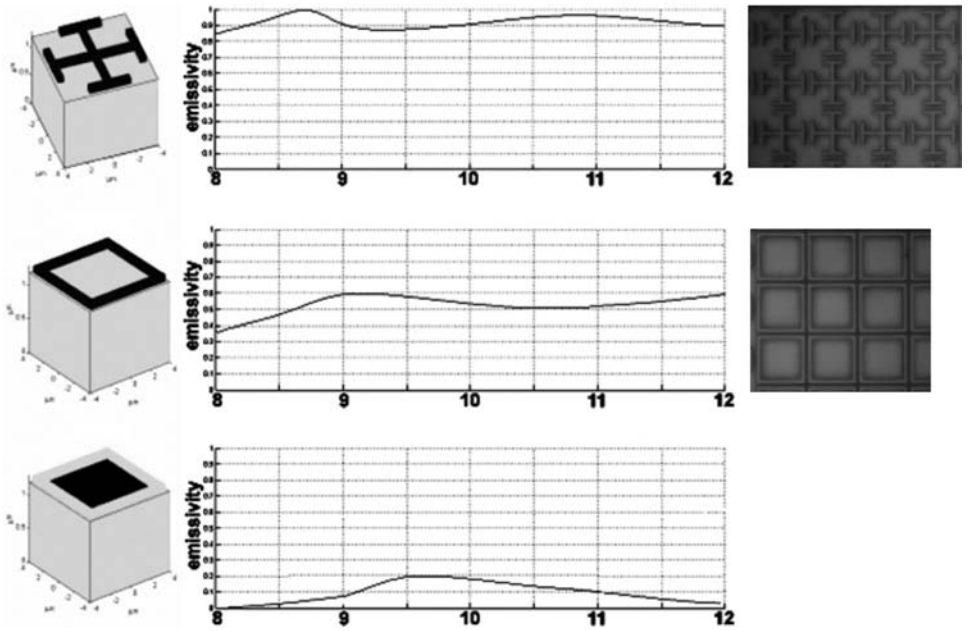

Figure 7.6 Three different FSSs fabricated to present high (Jerusalem cross), medium (square loop), and low (square patch) emissivities in the 8–12 μm wavelength band.

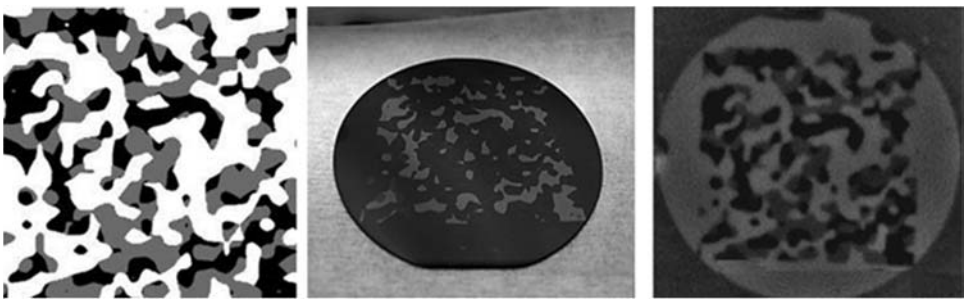

Figure 7.7 A random spatial pattern populated with three different types of FSSs showing distinguished spectral emissivities. The image of the fabricated device on a hot plate was acquired by a thermal camera in the 8–12 μm band.

[D'Archangel *et al.*, 2014b]. Owing to the serial nature of electron-beam lithography, even with a state-of-the-art system (Leica EBPG 5000 plus), a 4-inch wafer could take 24 hours to write. So it is of interest to have less-costly approaches for creating large-area FSSs. Imprint lithography is a candidate approach [Puscasu *et al.*, 2000a] requiring construction of a master tool for transferring the spatial information (see Fig. 7.8.a). Imprint lithography of IR FSSs on a roll-to-roll process holds promise for enabling meter-sized IR FSSs on flexible or rigid substrates (see Fig. 7.8.b). Some process challenges

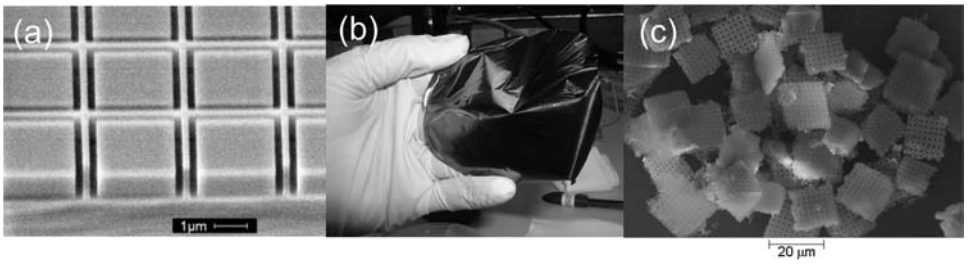

Figure 7.8 Large-scale fabrication of FSSs is most successful using imprint fabrication. In this case (a) a master is necessary that can be applied onto (b) a flexible substrate. (c) Flakes of FSSs have been proposed as an alternative lower-cost fabrication method (adapted from [Shelton *et al.*, 2007] and [D'Archangel, 2014] and reproduced with permission of AVS).

involve releasing the pattern-transfer material from within narrow high-aspect-ratio features on the imprint tooling.

Another way to use the lower-cost replication offered by optical lithography is to use IR FSS flakes that can be incorporated into a liquid carrier solution or into a paint formulation. Small arrays, typically 10×10 unit cells, are created on a carrier wafer and then released from the wafer and collected for later use [D'Archangel *et al.*, 2011]. An etch process is used to define the flake boundaries. Experimental and numerical studies indicate that the main spectral features of the IR FSS are well preserved in the flakes [D'Archangel *et al.*, 2015]. Of course, the fill factor of the flakes on a surface has to be accounted for, since the flakes will typically not completely cover the surface, and the spectral properties of the underlying surface will contribute to some degree. The spectral transmittance of the liquid in which the flakes are immersed will also play a role. In the fabrication process of the flakes, it should be noted that the flakes should be symmetric about their center (for instance, a ground plane) because the flakes can be oriented with either side up when delivered to the final surface to receive the FSS treatment (see Fig. 7.8.c).

In some FSS designs, not only is it possible to modify the reflected spectrum, but also, by using a leaky-wave design, one can tailor the far-field pattern of radiation to be steered towards a desired direction [Kinzel *et al.*, 2015].

7.1.1 Spectral response of frequency-selective surfaces

The characteristic parameter of FSSs is the change in the spectral composition of its reflected, transmitted, or absorbed radiation [Ginn *et al.*, 2010b] [D'Archangel *et al.*, 2015] [D'Archangel *et al.*, 2013], which, for some specific designs involving thermochromic materials, can be tuned within a given range [Shelton, 2010]. Also, by including active elements into the design, FSSs can work as detectors, combining infrared antennas and resonant structures [Kinzel *et al.*, 2013].

The relation among reflectivity, transmissivity, and absorption is easily derived from the energy conservation law:

$$R(\lambda) + T(\lambda) + A(\lambda) = 1, \tag{7.1}$$

where R, T, and A denote reflectivity, transmissivity, and absorptance, respectively. Absorptivity, α_λ, is defined as the ratio of the energy absorbed by the system to the incident energy. If the system is in thermal equilibrium, this energy has to be emitted by the system, obeying Kirchhoff's law of thermal equilibrium. In this situation, the relation between emissivity and absorptivity is

$$\epsilon_\lambda = \alpha_\lambda, \tag{7.2}$$

where emissivity, ϵ_λ, is defined as the energy emitted by the system with respect to the energy emitted if the system were a perfect blackbody. Because absorption is intrinsically related to emission through Kirchhoff's law, spectral emissivity is a typical figure of merit for these devices.

Measurements of IR emissivity in the 3–14 μm band were made using a spectro-radiometer incorporating a circular variable filter (CVF). The FSSs were thermally contacted to a hotplate and brought to a temperature of 200 °C. The emission spectrum was measured by the instrument and was compared with the emission spectrum of a blackbody at that temperature to obtain the emissivity as the ratio of these two values. Figure 7.9 shows the practical realization of a radiometer able to measure the desired spectral signature of the fabricated FSS.

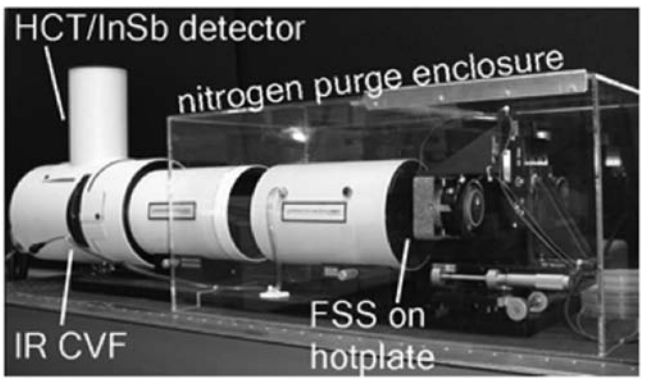

Figure 7.9 Practical realization of a radiometer to measure spectral emissivity of FSSs in the range of interest of 3–14 μm. The FSS is placed on a controlled hot plate in front of the radiometer. The system needs to be N_2 purged to avoid atmospheric absorption bands in this region (adapted from [Monacelli *et al.*, 2005] and reproduced with permission of IEEE).

7.2 Resonant Optical Retarders

Meander-line waveplates have been traditionally used in the radiofrequency portion of the spectrum to convert linearly polarized radiation into circularly polarized radiation. The meander-line structures seen in Fig. 7.10 act as a phase retarder for the two orthogonal wave components that are polarized along and perpendicular to the meander axis. The meander line acts primarily as an inductive element along the meander axis and as a capacitive element perpendicular to the meander axis, creating the relative phase delay for the orthogonal polarization components [Tharp, 2007] [Tharp *et al.*, 2006a] [Tharp *et al.*, 2006b] [Tharp *et al.*, 2007b] [Young *et al.*, 1973].

Use of electron-beam lithography has made fabrication of such structures feasible at higher frequencies. The ease of fabrication, low fabrication costs, and compact construction provide a potentially important alternative to birefringent crystals in the IR, terahertz, and millimeter-wave bands. An especially attractive characteristic of meander-line waveplates is the ability to define designs for specific frequencies and phase delays by simple changes in the lithography [Wadsworth *et al.*, 2011].

A meander line has significant bandwidth in both wavelength and angle of incidence compared to traditional birefringent crystal waveplates. Shown in Fig. 7.11.a are measured data on the phase delay of a meander-line waveplate over the 8–12 μm band. Over the range from 8.5 μm to 12 μm, the desired quarter-wave phase delay is achieved within about $0.05/\pi$ from the ideal of $0.5/\pi$. Figure 7.11.b plots the axial ratio of the polarization ellipse obtained from the device when the incident polarization state is linear and oriented in such a way that the two orthogonal components along the main directions of the meander are equal (at 45°). Shown in Fig. 7.11.c are measured data as a function of angle of incidence for the same structure, again showing very

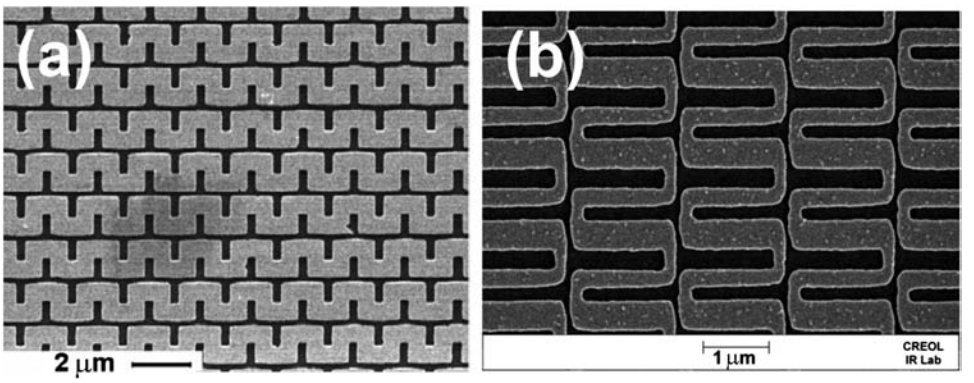

Figure 7.10 Meander-line structures for the infrared with (a) symmetric and (b) asymmetric meanders (adapted from [Tharp *et al.*, 2007a] and [Wadsworth & Boreman, 2011a] and reproduced with permission of IEEE and OSA).

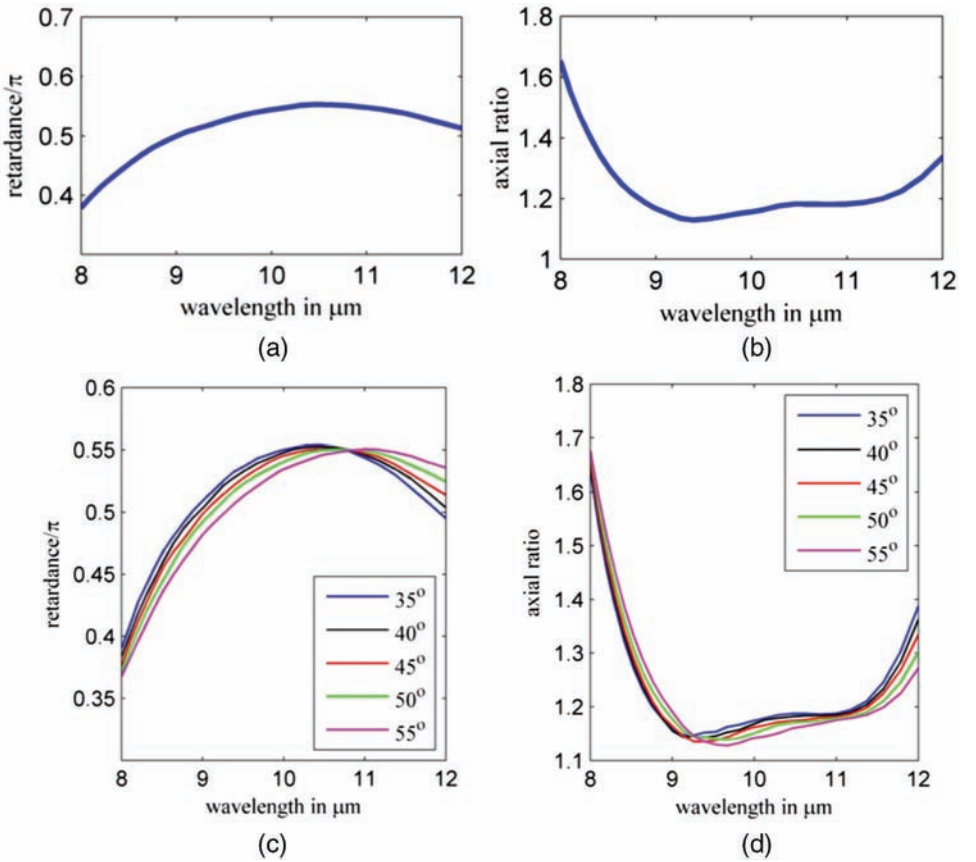

Figure 7.11 (a) and (c) Relative retardance and (b) and (d) axial ratio for a meander line designed to work at an angle of incidence of 45° for [(a) and (b)] this nominal angle and for [(c) and (d)] a collection of angles around this nominal value (adapted from [Wadsworth & Boreman, 2011a] and reproduced with permission of OSA).

stable behavior. The same good stability with respect to the angle of incidence appears in the axial ratio of the ellipse of polarization (see Fig. 7.11.d). This stability could be of significant benefit for polarization imaging systems, where broadband spectral response is required, and where fast $f/\#$ optics is often desirable. In particular, the angular bandwidth seen in Fig. 7.11 would allow meander-line structures to be placed in a converging beam. This is in contrast to birefringent waveplates, which typically must be placed in a collimated region of the optical system [Wadsworth & Boreman, 2010] [Wadsworth & Boreman, 2011a] [Wadsworth & Boreman, 2011b].

The power conversion efficiency of meander-line waveplates in terms of conversion of a linear polarization state into the desired output state (often circular polarization) is affected by two issues: loss in the metallic meanders and impedance mismatch between the meander line and the surrounding air.

For reflective waveplates, the peak measured conversion efficiency is 85% [Wadsworth & Boreman, 2011a]. For transmissive waveplates, the peak measured conversion efficiency for a two-layer design is 65%, with approximately 70–75% as the upper limit for an optimized three-layer design [Wadsworth & Boreman, 2010] [Wadsworth, 2011].

7.3 Resonant Phase Plates

A reflectarray is a quasi-periodic array of individual resonant elements on a dielectric layer located above a ground plane [Huang & Encinar, 2008]. The spacing of the unit cells is subwavelength in dimension. This structure provides a phase shift on reflection that depends on the local geometry of the unit cell. This is different from a standard phase kinoform element, in which the phase shift depends on the height of a dielectric layer. In a reflectarray, the dimension of the unit-cell antennas will typically vary across the array, producing a phase-delay variation across the surface. From an optics perspective, this is essentially a wavefront modification on reflection [Yang *et al.*, 2012] [Ginn *et al.*, 2007b]. These types of structures have been used for some time in the radiofrequency portion of the spectrum, but are not yet commonplace in the IR.

An initial demonstration in the IR uses a square-patch design populating alternating Fresnel zones with elements that successively shift the phase 180° [Ginn *et al.*, 2008]. In this case, only two designs of the unit-cell resonant element are necessary. However, by varying the dimensions of the patches, it is possible to generate smaller phase shifts between adjacent zones (see Fig. 7.12). Variable-patch reflectarrays achieve a phase shift modification

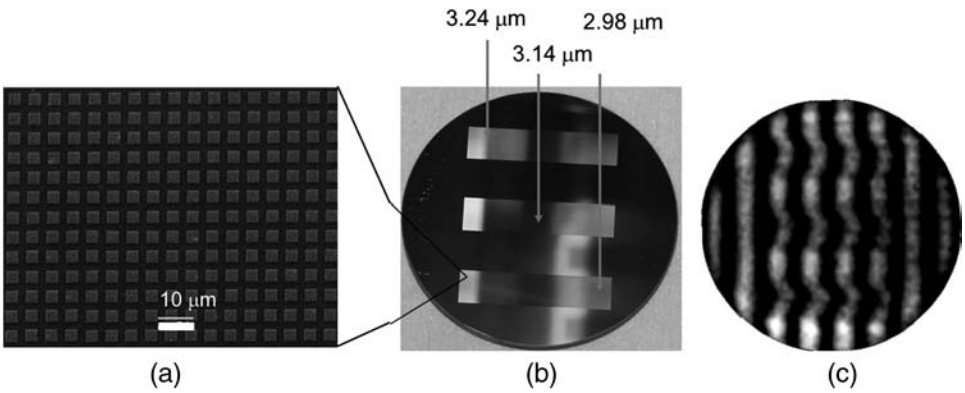

Figure 7.12 A proof of concept of the reflectarray performance fabricated by writing (a) three different cell units, producing (b) three phase variations on a optical flat substrate. They were tested using a Michelson interferometer that showed (c) fringe displacements at the location of the resonant structures (adapted from [Ginn *et al.*, 2007b] and reproduced with permission of IEEE).

upon reflection because the variation in element size changes the resonant frequency of the patch. A slight variation in the resonant frequency of the patch changes the phase of the standing wave formed between the patch and the ground plane, which in turn alters the phase of the re-radiated wave. Each row is made up of a different sized patch stood off above a ground plane by a 450 nm layer of ZrO_2. The substrate is a 50 mm Si wafer, and the ground plane and patches are Au to reduce absorption losses. The design is based on a scaled version of a RF reflectarray. Heuristic calculations based on a lossless transmission line model are useful in predicting the main features of the behavior of the structure, but finite-element modeling that accounted for the non-ideal nature of the metal is needed for accurate predictive capability. The phase response of each row is measured using an IR Twyman–Green interferometer at 10.6 μm, and it is seen that the reflected phase shift depends on patch dimension. This procedure is repeated with various patch sizes to produce the phase-shift versus patch-size plots in Fig. 7.12.

The increase in thickness of the stand-off layer detunes the Q of the resonant element, which allows for a slower phase transition versus patch size. The slower phase transition reduces the sensitivity of the design to fabrication tolerances while simultaneously providing less absorption loss (see Fig. 7.13).

A focusing element demonstration was undertaken using patch reflectarrays. A 25.4 mm diameter Fresnel zone plate reflectarray was constructed as an $f/6$ focusing element, with 100 discrete zones and 20 million patch elements. Only one discrete phase state of the binary reflectarray was populated with patch elements. The other phase state was simply a combination of the ground plane and the stand-off layer. The layer thickness was chosen to yield 180° of phase shift upon reflection, relative to the region without patches. Such surfaces

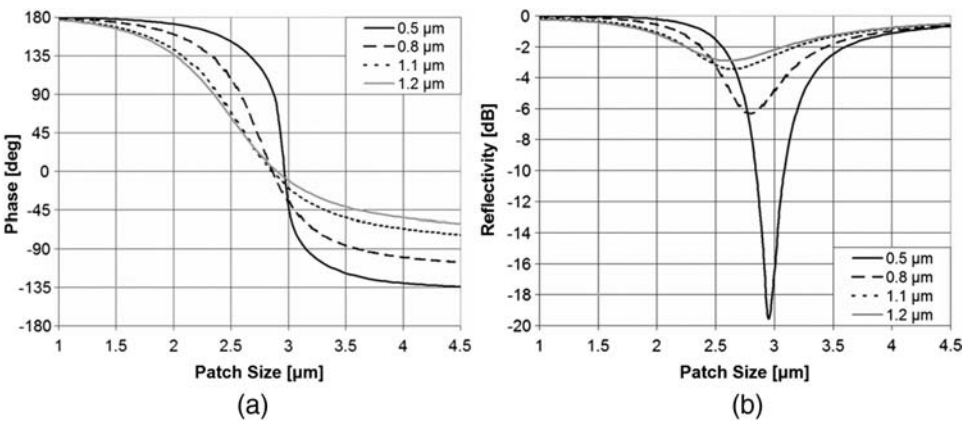

Figure 7.13 The thickness of the stand-off dielectric layer is of importance when tuning both (a) the phase change and (b) the amplitude in terms of the size of the patch. Operating wavelength is $\lambda = 10.6\,\mu m$ (adapted from [Ginn *et al.*, 2008] and reproduced with permission of OSA).

may also have applications in very low-cost lithographic IR optics, or in conformal optical surfaces.

Infrared reflectarrays are desirable for many of the reasons they are desirable for use at lower frequencies, such as reduced cost, weight, and volume for focusing surfaces [Ginn, 2009]. Reflectarrays facilitate direct stacking of multiple planar elements, (e.g., filters and polarizers) on the reflectarray for additional weight and volume reductions. It may also be that IR reflectarrays will be seen to provide additional degrees of freedom for aberration correction, since their dependence of magnitude and phase on angle of incidence distinctly differs from that for usual optical elements. Figure 7.14 shows the angular dependence of different square patches and slotted-square patches in terms of the magnitude and phase shift [Ginn *et al.*, 2010a]. When considering thermochromic materials, the reflectarray can be tuned within a specific spectral range [Shelton *et al.*, 2010b].

7.3.1 Aberrations and MTF in reflectarrays

Reflectarrays could be, at some point, considered as a variation of Fresnel zone plates. The local phase shift given by optical path differences in diffractive elements is produced here by properly suited and designed resonant structures. However, there are some characteristics that are intrinsic to the case of reflectarrays. One of them is the off-axis behavior of the reflected light departing the reflectarray element. When using multilevel phase reflectarrays, each individual type behaves differently. On the other hand, resonant elements can be defined to work selectively with polarization. Even when selecting geometries with square symmetry, the actual response of the reflectarray may differ under illumination with other polarization orientations. As an example, Fig. 7.14 shows the irradiance profiles along a fixed direction on the image plane for two orthogonal states of linearly polarized light. The elements of this reflectarray are squares, and the two linear polarization states are oriented along the sides of those squares. However, when considering polarization, the off-axis contributions are not equal for each polarization. These differences appear in the irradiance profiles as subtle discrepancies. These discrepancies are larger as the $f/\#$ decreases because at larger angles the off-axis contributions are increasingly different for the two states of polarization. These changes also reflect the modulation transfer function (MTF) behavior, which is also different for these two polarizations. This characteristic is only applicable to reflectarrays and should be considered as a kind of polarization-related aberration.

Besides off-axis and polarization dependence, reflectarrays show a remarkable chromatic dependence. This dependence is mainly caused by the Fresnel zone arrangement that is strongly selective with wavelength. Figure 7.16 shows this behavior for the same reflectarray considered in Fig. 7.15. The plot in Fig. 7.16.a represents the irradiance along the optical axis in terms of the distance from the reflectarray, z, and wavelength, λ.

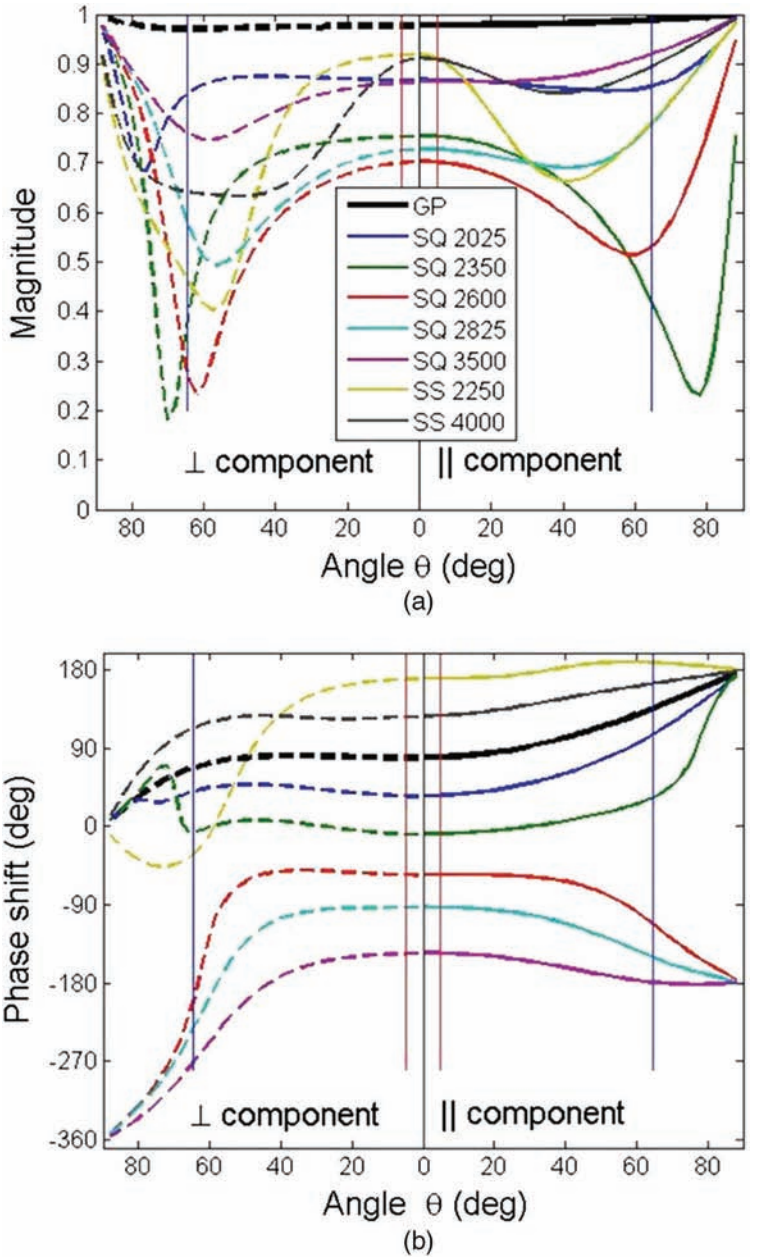

Figure 7.14 (a) Magnitude and (b) phase shift produced by the eight elements of the subzone reflectarray as a function of the angle and the polarization state (TE, perpendicular, and TM, parallel, components). The color coding is the same for both graphs. In the key, GP is ground plane, SQ (square patches) is followed by the size of the patch in nanometers, and SS (slotted-square patches) is by followed by the size of the slot in nanometers in a 4500 nm square patch. The wavelength of design is $\lambda = 10.6\,\mu$m (adapted from [Ginn *et al.*, 2010a] and reproduced with permission of OSA).

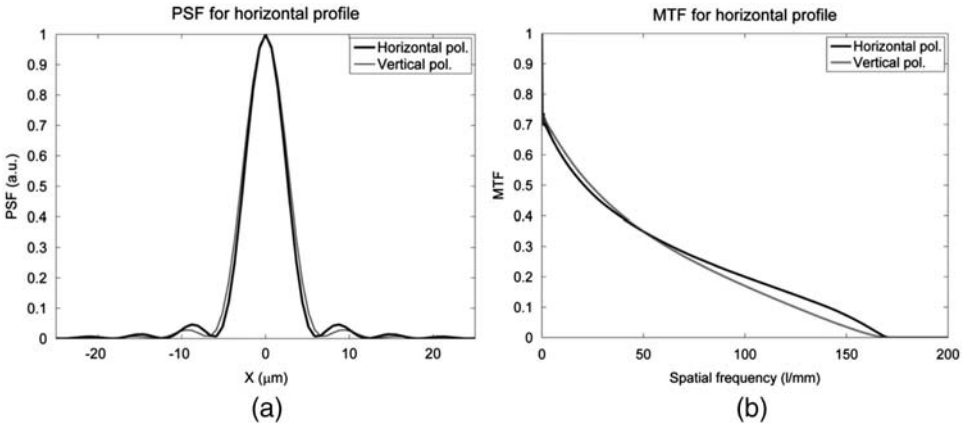

Figure 7.15 Profiles of (a) the point spread function (PSF) and (b) the modulation transfer function (MTF) for two orthogonal polarizations. The unit cell of this array has an square shape. The reflectarray consists of eight phase levels arranged as a multilevel Fresnel zone plate and has an aperture of $f/0.23$ (adapted from [Gómez-Pedrero *et al.*, 2011] and reproduced with permission of OSA).

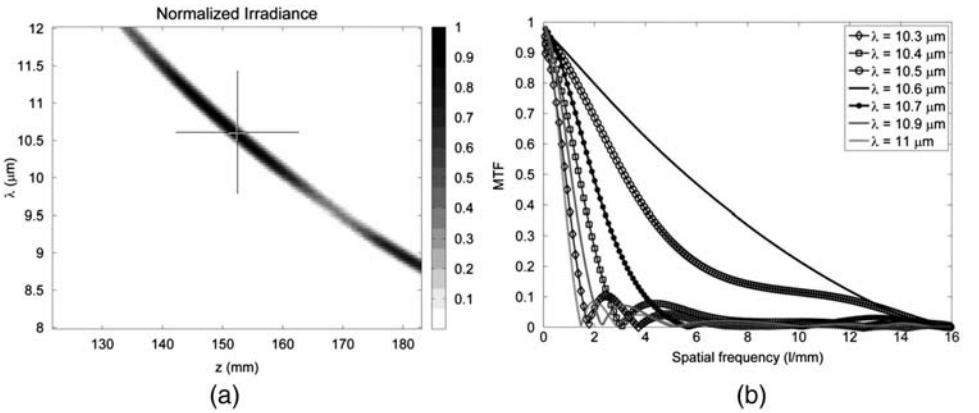

Figure 7.16 (a) The irradiance map plotted as a function of the axial coordinate along the optical axis, z, and the wavelength, λ. The cross corresponds to the wavelength of design, $\lambda_d = 10.6\,\mu$m. (b) The MTF drops abruptly when moving from the wavelenght of design, denoting a strong chromatic aberration of the device. The reflectarray consists of eight phase levels arranged as a multilevel Fresnel zone plate and has an aperture of $f/0.23$ (adapted from [Gómez-Pedrero *et al.*, 2011] and reproduced with permission of OSA).

This reflectarray was designed for a focal length and wavelength given by the cross in this figure. At the same time, when evaluating the MTF for different wavelengths around the wavelength of design, and maintaining the same image plane, this MTF drops abruptly, denoting a strong chromatic aberration.

Chapter 8
Conclusions and Open Issues

For quite a few years, optical antennas and resonant structures have been the focus of several well-established fields that nonetheless are pushing the boundaries of science and technology. Between the 19th century foundations of electromagnetism and the 21st century revolution of nanophotonics, these antenna-like elements have found their way into cutting-edge laboratories and institutions that are pursuing the latest advances and contributions to nanoscience and nanotechnology. The research in optical antennas effectively merges the robustness of a well-founded formalism and the challenge to adapt to the optical regime those concepts that have been successful at lower frequencies. This quest cannot be seen as an incremental advance with respect to the previously obtained results. An understanding of these tiny structures at a subwavelength scale in the visible and the infrared has required the adaptation of the nanoworld to the quantum level, where cavity life time, and absorption and emission time constants are at play to fully grasp and analyze those phenomena. Nonlinear, electrochromic, and thermochromic mechanisms, and their combinations with metal, semi-metals, and dielectric materials have expanded the capabilities of new devices and applications. These additions also require appropriate analysis and modeling to properly include them in the inventory of useful technologies.

Besides the overview that we have provided in this book, there are a variety of issues that remain as open research topics surrounding the technology of optical and IR antennas. Among these issues we include the following.

Coupling efficiency. The coupling efficiency from free space (having a wave impedance of 377 Ω) to the antenna-coupled sensor is a key aspect of the practical application of this technology, since coupling efficiency directly translates to signal-to-noise ratio. The overall efficiency depends on several aspects. The first step is the coupling from free space to the antenna itself; i.e., the optimum launching of current waves in the arms of the antenna is a must. It has been demonstrated [Lail *et al.*, 2009] that high-index immersion lenses (necessarily with anti-reflection coatings) are useful in this regard, ultimately gaining perhaps a factor of $\times 50$ in the sensor response. It is possible

to anti-reflection coat a planar metallic film [Macleod, 2010], but the antenna arms are obviously not spatially uniform planar films. However, there may yet be a way to exploit this general concept by attempting to match the free-space impedance to the wave impedance presented by the antenna by adjusting substrate and/or superstrate indices. It is important to realize that the desired condition is that propagating current waves are launched rather than the incoming radiation simply being absorbed in the metallic material, or reflected back towards the incoming direction. Perhaps a subwavelength grating structure on the antenna arms could be utilized toward that end.

Another issue surrounding coupling efficiency is the impedance matching at the frequencies of operation between the antenna (at the feedpoint) and the sensor load impedance. Quantum-mechanical or density-of-states issues are not yet able to be completely modeled with computational electromagnetic codes, but a starting point for many sensors would be a model that encompasses dimensions and materials, including the constitutive relations, also at the quantum level when necessary. Multiphysics models should be able to take this approach farther to include thermal and mechanical domains.

To begin with the impedance-matching conditions, measured DC current–voltage characteristics are generally a good indicator of the high-frequency behavior of diodes. The main concern is that most planar antennas have feedpoint impedances of hundreds of ohms, and diodes typically have impedances in the 10 kΩ to 100 kΩ range. Impedance-matching networks can be implemented with lumped elements, even at IR frequencies, but such drastic mismatches are difficult to overcome even over a restricted bandwidth. Broadband matching will be even more of a challenge.

Measurement of coupling efficiency is an important aspect of solving the technological challenges, since improvement of any figure of merit is necessarily dependent on being able to quantify how response changes with design variations. The most relevant coupling efficiency metric is power coupled into (or dissipated in) the sensor divided by the power incident within the collection aperture of the antenna. With a measurement of collection area as mentioned in section 5.1, the incoming power can be found from the incident irradiance (W/cm^2). The main measurement challenge is the assessment of local current and voltage levels at the sensor inputs. Especially given the small current levels, this is a very sensitive measurement and is easily affected by the impedance characteristics of the measurement apparatus and the noise level.

Transduction and rectification mechanisms. The practical deployment of optical antennas strongly depends on all of the figures of merit related to the quality of the retrieved signal: responsivity, signal-to-noise ratio, specific detectivity, D^*, time constant, etc. The rest of the advantages of the antenna approach are well recognized in the radioelectric spectrum and are related to the selectivity in polarization, customized far-field patterns, beam steering,

spectral resolution and tuning, etc. Most of the good characteristics of antennas have been successfully translated into the optical range. However, the quality of the signal is a real concern and deserves further attention to improve. In this book we have provided some reasons, mostly related to the behavior of materials at optical frequencies, for the limited strength of the signal. However, currents are truly built up along the geometries of resonant structures and directed towards tranducers and read-out electronics. The current transduction mechanisms are based on thermal effects generated by the absorbed radiation (thermoelectric and bolometric effects), or alternatively on the rectification of currents crossing a tunneling barrier between two metallic regions. When optical antennas are used in optical sensing and detection, the signal can be amplified and handled by dedicated electronics. In this case, thermal effects provide a transduction mechanism that allows simpler fabrication tools. Also, thermoelectric mechanisms, which do not display a dissipative effect, rely on the thermal properties of materials. However, energy harvesting and some other applications involving a fast response require nano-scale rectifiers to be coupled to the antenna. This idea has been successfully applied in the radioelectric regime, where large rectification efficiencies have been demonstrated [MacSpadden *et al.*, 1996] [Hagerty *et al.*, 2004]. MIM transducers have been refined over the past decades, but applications in the optical and IR range require very low capacitances that imply stringent fabrication constraints. In this sense, the concept of an optical rectenna has generated significant attention [Moddel & Grover, 2013] because of its important implication in a variety of fields ranging from energy harvesting to optical sensing. Some interesting results have been obtained by rectifying the charge carriers using geometry. This approach has shown promising initial results, and much effort is being made to improve its characteristics, especially the $I-V$ curve and the overall efficiency of the process [Briones *et al.*, 2013].

In this sense, a better understanding of the rectification process and the development of new strategies and methods for transducing the signal and for harvesting radiation towards external circuitry will enable the use of optical antennas in additional applications.

Low-loss transmission lines. For practical implementation of the phased-array antenna concept, it is necessary to develop transmission line configurations that have the field confinement advantage of metallic lines (such as coplanar strip lines) but without the excessively high attenuation of metallic structures at IR frequencies. Purely dielectric waveguides do not have the ability to confine and guide fields in subwavelength structures, making them poor candidates for antenna interconnection and on-chip signal routing. Alternative material choices, such as SiC or 2D materials, should be examined for their ability to confine and guide IR radiation with low loss. Achieving this would allow many more antennas to be co-phased compared to current

demonstrations with metallic lines, facilitating synthesis of very narrow beamwidths and participation of large surface areas in sensing functions.

Tunable antennas. One of the appeals of IR antenna technology from its inception has been the potential for real-time electronic control of the antenna reception characteristics—wavelength, polarization, and look angle. The realization of these tuning potentials in high-sensitivity IR sensors would enable focal-plane-array-based imaging spectrometers, imaging polarimeters, and gimbal-less field-of-view scanning. That potential has thus far not been realized in practice because of the lack of low-loss ways to control current waves in the antenna arms. Control techniques common in the RF range often do not have the required response times for operation with current oscillations at 30 terahertz and above. MIM diodes have the potential for these response times, but the nonlinearity of their current–voltage characteristic is still not abrupt enough for effective current control, especially at small bias voltages. They also typically have high impedance, making direct integration into antenna arms difficult without causing excessive dissipative loss. Other types of diodes and junctions may be integrated into the vicinity of the antenna arms without being in the current path. These affect the current flow by capacitive coupling [Gritz *et al.*, 2005]. Micro-electrical-mechanical systems (MEMS) also hold promise for placing adjustment structures in the vicinity of the antenna arms [Agustí *et al.*, 2013]. It may also be possible to integrate tunable materials (e.g, thermochromics [Shelton *et al.*, 2010b]) into the antenna structure or its immediate environment. Materials with photo-switchable response, for instance using photocarrier generation, may also find application in this regard.

2D materials. The capabilities of bidimensional materials and membranes, such as graphene, have also attracted a lot of attention because of the low resistivity and the large free-mean-path of the charge carriers injected in these structures. Graphene has been proposed and used for the fabrication of geometrical rectifiers in rectenna devices [Moddel *et al.*, 2012] [Dragoman & Dragoman, 2013] [Tamagnone *et al.*, 2013] [Zhu *et al.*, 2013]. It is expected that research in this area will produce a better understanding of the capabilities of graphene and other bidimensional materials for the generation of resonant elements and improved transduction mechanisms.

3D antenna structures. The basic idea of conical horn concentrators is appealing, as has been shown in the literature [Kim *et al.*, 2004]. This class of structures has the potential to achieve subwavelength concentration unavailable with lenslet arrays, reasonably low loss, good packing fraction in an array, and good collection efficiency. However, presently, the three-dimensional (3D)

nature of antenna fabrication and metallization is challenging in itself, and practical integration issues with IR sensors in array format have not been solved. The fabrication of an array of IR horn antennas presently appears to be at the limit of current two-photon lithographic techniques in terms of spatial resolution and field of view [Aumann *et al.*, 2014]. Some other highly directive devices, such as Yagi–Uda antennas, have been demonstrated [Li *et al.*, 2007] [Taminiau *et al.*, 2008], and very interesting results have been realized using planar designs [Kosako *et al.*, 2010]. Also, some actual 3D structures have been fabricated and demonstrated in the optical regime [Dregely *et al.*, 2011]. Fabrication of 3D structures is itself a real challenge. Some sculpturing techniques, such as focused ion beam (FIB), have been able to shape antenna dipoles and cantilevers for near-field excitation and measurements. Additive techniques, such as multiphoton lithography, are reaching sufficient accuracy and reliability to play an important role in the fabrication of 3D optical resonant elements working at optical frequencies [Gansel *et al.*, 2009].

Large-area frequency-selective surfaces. Most practical applications of IR frequency-selective surfaces require substantial areas to be covered. Direct-write electron-beam lithography is an untenable solution to those requirements because of the excessive write time and consequent expense. Some potential solutions exist in developmental stages. Released flakes of metamaterial incorporated into paints is an interesting alternative, but still requires cost-efficient lithographic generation of large quantities of material. Imprint lithography takes an electron-beam-generated master and replicates similar structures using mechanical pressure. This process has the requisite spatial resolution for operation in the IR. Roll-to-roll processes are an extension of this concept to continuous sheets of material. These processes are well-developed, for instance, in the replication of CDs and could be applied to IR 2D metamaterials, assuming sufficient capitalization for development of manufacturing apparatus and robust fabrication processes. Very recently, an ultraviolet microsphere lithographic technique [Bonakdar *et al.*, 2015] was proposed and successfully adapted for the fabrication of metasurfaces containing resonant elements with a wide variety of shapes and forms [Qu & Kinzel, 2016]. The combination and merging of these techniques should lead to the ability to generate affordable surface coverage of IR 2D metamaterials.

In summary, optical antennas and resonant structures require a merging of the concepts of well-recognized physics (concepts that are at the core of the electronic and nanotechnology revolution) with new ideas and strategies based on the special behavior of light and matter at the nanoscale, including quantum physics. Basic science and applied technology must combine in every problem related to optical antennas. Modeling in this domain requires multiple points of view (material science, quantum mechanics, photonics,

etc.). Accurate simulations should incorporate computational packages able to deal with this multiphysics environment. The available fabrication techniques are pushed to the limits to obtain higher spatial resolution and enhance aspect ratio in the realization of the proposed structures. At the same time, innovative and advanced tools for testing and characterization are necessary to obtain those figures of merit related to the performance of the devices (directivity, D^*, spectral response, etc.). Also, near-field and far-field measurements rely on the implementation of experimental setups able to handle these subwavelength structures with the desired spatial and angular resolution.

Research on optical antennas and resonant structures is exciting by itself and is paving the way for some future advances in this technology. This is why we encourage readers of this book to keep studying and analyzing these devices, and to envision new applications and uses yet to come.

References

[Abadal *et al*., 2013] Abadal, G., Alda, J., & Agustí, J. 2013. *ICT- Energy - Concepts towards Zero-Power Information and Communication Technology*. Nanoscale Energy Management Concepts Towards Zero-Power Information and Communication. Intech. Chap. Electromagnetic radiation energy harvesting. The rectenna based approach, pages 79–106.

[Abdel-Rahman, 2004] Abdel-Rahman, M. 2004. *Dual-band millimeter-wave and infrared antenna-coupled detectors and focal plane arrays*. Ph.D. thesis, University of Central Florida.

[Abdel-Rahman *et al*., 2005a] Abdel-Rahman, M., Monacelli, B., Weeks, A., Zummo, G., & Boreman, G. 2005. Design, fabrication and characterization of antenna-coupled MOM diodes for dual-band detection. *Optical Engineering*, **44**(6), 066401.

[Abdel-Rahman *et al*., 2005b] Abdel-Rahman, M., Lail, B., & Boreman, G. 2005. Dual-band millimeter-wave and infrared focal-plane arrays. *Microwave and Optical Technology Letters*, **46**(1), 78–80.

[Abdel-Rahman *et al*., 2004] Abdel-Rahman, M. R., González, F. J., & Boreman, G. D. 2004. Antenna-coupled metal-oxide-metal diodes for dual-band detection at 92.5 GHz and 28 THz. *Electronics Letters*, **40**(2), 116–118.

[Agio & Alù, 2013] Agio, M., & Alù, A. (eds). 2013. *Optical Antennas*. Cambridge University Press.

[Agustí *et al*., 2013] Agustí, J., Cuadrado, A., López-Suárez, M., Alda, J., & Abadal, G. 2013. The opto-thermo-mechanical conversion mechanism in a MEMS with integrated nanoantennas for energy harvesting from infrared radiation. *Nanoenergy Letters*, **6**, 45–46.

[Alda, 2003] Alda, J. 2003. *Laser and Gaussian Beam Propagation and Transformation. Encyclopedia of Optical Engineering*. Marcel Dekker. Chap. Laser and Gaussian beam propagation and transformation, pages 999–1013.

[Alda & Boreman, 2008] Alda, J., & Boreman, G. 2008. Optimization of polygonal Fresnel zone plates. *Microwave and Optical Technology Letters*, **50**(2), 536–541.

[Alda & González, 2009a] Alda, J., & González, F. J. 2009. Fresnel zone antenna for dual-band detection at millimeter and infrared wavelengths. *Optics Letters*, **34**(6), 809–811.

[Alda & González, 2009b] Alda, J., & González, F. J. 2009. Polygonal Fresnel zone plates. *Journal of Optics A: Pure and Applied Optics*, **11**(8), 085707.

[Alda *et al.*, 1997] Alda, J., Alonso, J., & Bernabeu, E. 1997. Characterization of aberrated laser beams. *Journal of the Optical Society of America A*, **14**(10), 2737–2747.

[Alda *et al.*, 1999] Alda, J., Fumeaux, C., Codreanu, I., Schaefer, J., & Boreman, G. 1999. Deconvolution method for two-dimensional spatial-response mapping of lithographic infrared antennas. *Applied Optics*, **38**(19), 3993–4000.

[Alda *et al.*, 2000] Alda, J., Fumeaux, C., Gritz, M., Spencer, D., & Boreman, G. 2000. Responsivity of infrared antenna-coupled microbolometers for air-side and substrate-side illumination. *Infrared Physics & Technology*, **41**(1), 1–9.

[Alda *et al.*, 2004] Alda, J., López-Alonso, J. M., Rico-Garcia, J. M., Zoido, J., & Boreman, G. 2004. Spatial characterization of light detectors with nanometric resolution. *Pages 226–235 of: Proc. SPIE*, vol. **5407**.

[Alda *et al.*, 2005] Alda, J., Rico-Garcia, J. M., López-Alonso, J. M., & Boreman, G. 2005. Optical antennas for nano-photonic applications. *Nanotechnology*, **16**(5), S230–S234.

[Alda *et al.*, 2006a] Alda, J., Rico-Garcia, J. M., López-Alonso, J. M., Lail, B., & Boreman, G. 2006. Design of Fresnel lenses and binary-staircase kinoforms of low value of the aperture number. *Optics Communications*, **260**(2), 454–461.

[Alda *et al.*, 2006b] Alda, J., López-Alonso, J. M., & Rico-García, J. M. 2006. Nano-antennas for opto-electronics and nano-photonics. *SPIE Newsroom*.

[Alù & Engheta, 2008] Alù, A., & Engheta, N. 2008. Input impedance, nanocircuit loading, and radiation tuning of optical nanoantennas. *Physical Review Letters*, **101**, 043901.

[Alù & Engheta, 2013] Alù, A., & Engheta, N. 2013. Theory, modeling and features of optical nanoantennas. *IEEE Transactions on Antennas and Propagation*, **61**(4), 1508–1517.

[Aristotle, 4th century BC] Aristotle. 4th century BC. *De animalibus*. Translated by T. Gaza.

[Aumann *et al.*, 2014] Aumann, A., Ksouri, S., Guo, Q., Sure, C., Gurevich, E., & Ostendorf, A. 2014. Resolution and aspect ratio in two-photon lithography of positive photoresist. *Journal of Laser Applications*, **26**(2), 022002.

[Balanis, 2005] Balanis, C. 2005. *Antenna Theory. Analysis and Design*. 3rd edn. Wiley-Interscience.

[Barnard *et al.*, 2011] Barnard, E., Pala, R., & Brongersma, M. 2011. Photocurrent mapping of near-field optical antenna resonances. *Nature Nanotechnology*, **6**(9), 588–593.

[Bean *et al.*, 2010] Bean, J., Slovick, B., & Boreman, G. 2010. Influence of substrate configuration on the angular response pattern of infrared antennas. *Optics Express*, **18**(21), 21705–21713.

[Bean *et al.*, 2011] Bean, J., Weeks, A., & Boreman, G. 2011. Performance optimization of antenna-coupled Al/AlO_x/Pt tunnel diode infrared detectors. *IEEE Journal of Quantum Electronics*, **47**(1), 126–135.

[Berkovitch *et al.*, 2012] Berkovitch, N., Ginzburg, P., & Orenstein, M. 2012. Nano-plasmonic antennas in the near infrared regime. *Journal of Physics: Condensed Matter*, **24**(7), 073202.

[Berland, 2003] Berland, B. 2003. *Photovoltaic Technologies Beyond the Horizon: Optical Rectenna Solar Cell*. Tech. rept. National Renewable Energy Laboratory.

[Bharadwaj *et al.*, 2009] Bharadwaj, P., Deutsch, B., & Novotny, L. 2009. Optical antennas. *Advances in Optics and Photonics*, **1**(3), 438–483.

[Bonakdar *et al.*, 2015] Bonakdar, A., Rezaei, M., Brown, R., Fathipour, V., Dexheimer, E., Jang, S. J., & Mohseni, H. 2015. Deep-UV microsphere projection lithography. *Optics Letters*, **40**(11), 2537–2540.

[Boreman, 1996] Boreman, G. 1996. Divide and conquer. *OE Magazine, SPIE Newsroom*, 47–48.

[Boreman, 2008] Boreman, G. 2008. Infrared Antennas. *Page FThV1 of: Frontiers in Optics 2008. Laser Science XXIV/Plasmonics and Metamaterials/ Optical Fabrication and Testing*. Optical Society of America.

[Boreman *et al.*, 1996] Boreman, G., Dogariu, A., Christodoulou, C., & Kotter, D. 1996. Dipole-on-dielectric model for infrared lithographic spiral antennas. *Optics Letters*, **21**(5), 309–311.

[Boreman *et al.*, 1998] Boreman, G., Fumeaux, C., Herrmann, W., Kneubühl, F. K., & Rothuizen, H. 1998. Tunable polarization response of a planar asymmetric-spiral infrared antenna. *Optics Letters*, **23**(24), 1912–1914.

[Boreman *et al.*, 2006] Boreman, G., González, F. J., & Porter, J. 2006. Multispectral multipolarization antenna-coupled infrared focal plane array. *US Patent 7,095,027*.

[Born & Wolf, 1980] Born, M., & Wolf, E. 1980. *Principles of Optics*. 6th edn. Pergamon Press.

[Brewitt-Taylor *et al.*, 1981] Brewitt-Taylor, C., Gunton, D., & Rees, H. 1981. Planar antennas on a dielectric surface. *Electronics Letters*, **17**(20), 729–731.

[Briones *et al.*, 2013] Briones, E., González, F. J., & Alda, J. 2013. Conversion efficiency of broad-band rectennas for solar energy harvesting applications. *Optics Express*, **21**(S3), A412–A418.

[Briones *et al.*, 2014a] Briones, E., Cuadrado, A., Briones, J., de León, R. Díaz, Martínez-Antón, J. C., MacMurtry, S., Hehn, M., Montaigne, F.,

Alda, J., & González, F. J. 2014. Seebeck nanoantenas for the detection and characterization of infrared radiation. *Optics Express*, **22**(106), A1538–A1546.

[Briones *et al.*, 2014b] Briones, E., Briones, J., Cuadrado, A., Martínez-Antón, J. C., MacMurtry, S., Hehn, M., Montaigne, F., Alda, J., & González, F. J. 2014. Seebeck nanoantennas for solar energy harvesting. *Applied Physics Letters*, **105**(9), 093108.

[Brown, 1984] Brown, W. C. 1984. The history of power transmission by radio waves. *IEEE Transactions on Microwave Theory and Techniques*, **32**(9), 1230–1242.

[Büttiker, 1986] Büttiker, M. 1986. Four-terminal phase-coherent conductance. *Physical Review Letters*, **57**, 1761–1764.

[Chambers, 1990] Chambers, R. G. 1990. *Electrons in Metals and Semiconductors*. Chapman and Hall.

[Chen *et al.*, 2016] Chen, P.-Y., Hajizadegan, M., Sakhdari, M., & Alù, A. 2016. Giant photoresponsivity of midinfrared hyperbolic metamaterials in the photon-assisted-tunneling regime. *Physical Review Applied*, **5**, 041001.

[Choi *et al.*, 2010] Choi, K., Ryu, G., Yesilkoy, F., Chryssis, A., Goldsman, N., Dagenais, M., & Peckerar, M. 2010. Geometry enhanced asymmetric rectifying tunneling diodes. *Journal of Vacuum Science & Technology B*, **28**(6), C6O50–C6O55.

[Codreanu & Boreman, 2001] Codreanu, I., & Boreman, G. 2001. Infrared microstrip dipole antennas—FDTD predictions versus experiment. *Microwave and Optical Technology Letters*, **29**(6), 381–383.

[Codreanu & Boreman, 2002a] Codreanu, I., & Boreman, G. 2002. Influence of dielectric substrate on the responsivity of microstrip dipole-antenna-coupled infrared microbolometers. *Applied Optics*, **41**(10), 1835–1840.

[Codreanu & Boreman, 2002b] Codreanu, I., & Boreman, G. 2002. Integration of microbolometers with infrared microstrip antennas. *Infrared Physics & Technology*, **43**(6), 335–344.

[Codreanu *et al.*, 1999] Codreanu, I., Fumeaux, C., Spencer, D., & Boreman, G. 1999. Microstrip antenna-coupled infrared detector. *Electronics Letters*, **35**(25), 2166–2167.

[Codreanu *et al.*, 2003] Codreanu, I., González, F. J., & Boreman, G. 2003. Detection mechanisms in microstrip dipole antenna-coupled infrared detectors. *Infrared Physics & Technology*, **44**(3), 155–163.

[Codreanu, 2001] Codreanu, Iulian. 2001. *Wavelength tunable IR antennas*. Ph.D. thesis, University of Central Florida.

[Corkish *et al.*, 2002] Corkish, R., Green, M., & Puzzer, T. 2002. Solar energy conversion by antennas. *Solar Energy*, **73**(6), 395–401.

[Crozier *et al.*, 2003] Crozier, K., Sundaramurthy, A., Kino, G., & Quate, C. 2003. Optical antennas: Resonators for local field enhancement. *Journal of Applied Physics*, **94**(7), 4632–4642.

[Cuadrado, 2014] Cuadrado, A. 2014. *Resonant structures for nanophotonics*. Ph.D. thesis, Univesity Complutense of Madrid (in Spanish).

[Cuadrado *et al*., 2012a] Cuadrado, A., Alda, J., & González, F. J. 2012. Distributed bolometric effect in optical antennas and resonant structures. *Journal of Nanophotonics*, **6**(1), 063512.

[Cuadrado *et al*., 2012b] Cuadrado, A., González, F. J., Agustí, J., & Alda, J. 2012. Material dependence of the distributed bolometric effect in resonant metallic nanostructures. *845724 of: Proc. SPIE*, vol. **8457**.

[Cuadrado *et al*., 2013a] Cuadrado, A., Alda, J., & González, F. J. 2013. Multiphysics simulation for the optimization of optical nanoantennas working as distributed bolometers in the infrared. *Journal of Nanophotonics*, **7**(1), 07093.

[Cuadrado *et al*., 2013b] Cuadrado, A., Silva-López, M., González, F. J., & Alda, J. 2013. Optimization of distributed bolometers coupled to optical antennas in the infrared. *87856W of: Proc. SPIE*, vol. **8785**.

[Cuadrado *et al*., 2013c] Cuadrado, A., Silva-López, M., González, F. J., & Alda, J. 2013. Robustness of antenna-coupled distributed bolometers. *Optics Letters*, **38**(19), 3784–3787.

[Cuadrado *et al*., 2014a] Cuadrado, A., Briones, E., González, F. J., & Alda, J. 2014. Polarimetric pixel using Seebeck nanoantennas. *Optics Express*, **22**(11), 13835–13845.

[Cuadrado *et al*., 2014b] Cuadrado, A., González, Francisco J., & Alda, J. 2014. Steerable optical antennas by selective heating. *Optics Letters*, **39**(7), 1957–1960.

[Cuadrado *et al*., 2015a] Cuadrado, A., Silva-López, M., López-Alonso, J. M., Martínez-Antón, J. C., Ezquerro, J. M., González, F. J., & Alda, J. 2015. Analysis of the spectral response of fractal antennas related with its geometry and current paths. *954736 of: Proc. SPIE*, vol. **9547**.

[Cuadrado *et al*., 2015b] Cuadrado, A., Silva-López, M., López-Alonso, J. M., Martínez-Antón, J. C., Ezquerro, J. M., González, F. J., & Alda, J. 2015. Detectivity comparison of bolometric optical antennas. *954735 of: Proc. SPIE*, vol. **9547**.

[Cuadrado *et al*., 2015c] Cuadrado, A., Silva-López, M., López-Alonso, J. M., Martínez-Antón, J. C., Ezquerroa, J. M., González, F. J., & Alda, J. 2015. Resonant elements contactless coupled to bolometric micro-stripes. *95471Z of: Proc. SPIE*, vol. **9547**.

[Cuadrado *et al*., 2016] Cuadrado, A., Toudert, J., García-Cámara, B., Vergaz, R., González, F. J., Alda, J., & Serna, R. 2016. Optical tuning of nanospheres through phase transition: an optical nanocircuit analysis. *IEEE Photonics Technology Letters*, **28**(24), 2878–2881.

[Cuadrado *et al*., 2017] Cuadrado, A., López-Alonso, J. M., González, F. J., & Alda, J. 2017. Spectral response of metallic optical antennas driven by temperature. *Plasmonics*, **12**, 553–561.

[Cubukcu & Capasso, 2009] Cubukcu, E., & Capasso, F. 2009. Optical nanorod antennas as dispersive one-dimensional Fabry–Pérot resonators for surface plasmons. *Applied Physics Letters*, **95**(20), 201101.

[Cubukcu *et al.*, 2006] Cubukcu, E., Kort, E., Crozier, K., & Capasso, F. 2006. Plasmonic laser antenna. *Applied Physics Letters*, **89**(9), 093120.

[D'Archangel *et al.*, 2011] D'Archangel, J., Boreman, G., Shelton, D., Sinclair, M., & Brener, I. 2011. Releasable infrared metamaterials. *Journal of Vacuum Science & Technology B*, **29**, 051806.

[D'Archangel *et al.*, 2013] D'Archangel, J., Tucker, E., Kinzel, E., Muller, E., Bechtel, H., Martin, M., Raschke, M., & Boreman, G. 2013. Near- and far-field spectroscopic imaging investigation of resonant square-loop infrared metasurfaces. *Optics Express*, **21**(14), 17150–17160.

[D'Archangel *et al.*, 2014a] D'Archangel, J., Tucker, E., Raschke, M., & Boreman, G. 2014. Array truncation effects in infrared frequency selective surfaces. *Optics Express*, **22**(13), 16645–16659.

[D'Archangel *et al.*, 2014b] D'Archangel, J., Shelton, D., Hudgins, R., Poutous, M., & Boreman, G. 2014. Large area infrared frequency selective surface with dimensions reproducible by optical lithography. *Journal of Vacuum Science & Technology B*, **32**, 051807.

[D'Archangel *et al.*, 2015] D'Archangel, J., Tucker, E., & Boreman, G. 2015. Spectral modification of array truncation effects in infrared frequency selective surfaces. *Infrared Physics & Technology*, **71**(7), 285–288.

[D'Archangel, 2014] D'Archangel, Jeff. 2014. *Large area conformal infrared frequency selective surfaces*. Ph.D. thesis, University of Central Florida.

[de Haan *et al.*, 2004] de Haan, S., Lorke, A., Kotthaus, J., Wegscheider, W., & Bichler, M. 2004. Rectification in mesoscopic systems with broken symmetry: quasiclassical ballistic versus classical transport. *Physical Review Letters*, **92**, 056806.

[Dereniak & Boreman, 1996] Dereniak, E., & Boreman, G. 1996. *Infrared Detectors and Systems*. John Wiley and Sons.

[Deslise, 2014] Deslise, J.-J. 2014. Know the differences between EM-simulation numerical methods. Microwaves & RF website: *mwrf.com*, 45–48.

[Dragoman & Dragoman, 2013] Dragoman, D., & Dragoman, M. 2013. Geometrically induced rectification in two-dimensional ballistic nanodevices. *Journal of Physics D*, **46**(5), 055306.

[Dregely *et al.*, 2011] Dregely, D., Taubert, R., Dorfmüller, J., Vogelgesang, R., Kern, K., & Giessen, H. 2011. 3D optical Yagi–Uda nanoantenna array. *Nature Communications*, **2**, 267.

[Eliasson, 2001] Eliasson, B. 2001. *Metal-insulator-metal diodes for solar energy conversion*. Ph.D. thesis, University of Colorado.

[Engheta, 2007] Engheta, N. 2007. Circuits with light at nanoscales: optical nanocircuits inspired by metamaterials. *Science*, **317**(5845), 1698–1702.

[Engheta *et al.*, 2005] Engheta, N., Salandrino, A., & Alù, A. 2005. Circuit elements at optical frequencies: nanoinductors, nanocapacitors, and nanoresistors. *Physical Review Letters*, **95**, 095504.

[Esfandiari *et al.*, 2005] Esfandiari, P., Bernstein, G., Fay, P., Porod, W., Rakos, B., Zarandy, A., Berland, B., Boloni, L., Boreman, G., Lail, B., Monacelli, B., & Weeks, A. 2005. Tunable antenna-coupled metal-oxide-metal (MOM) uncooled IR detector. *Pages 470–482 of: Proc. SPIE*, vol. **5783**.

[Faris *et al.*, 1973] Faris, S., Gustafson, T., & Wiesner, J. 1973. Detection of optical and infrared radiation with DC-biased electron-tunneling metal-barrier-metal diodes. *IEEE Journal of Quantum Electronics*, **9**(7), 737–745.

[Fleischmann & Geisel, 2002] Fleischmann, R., & Geisel, T. 2002. Mesoscopic rectifiers based on ballistic transport. *Physical Review Letters*, **89**, 016804.

[Florence *et al.*, 2011] Florence, L., Slovick, B., Kinzel, E., Bean, J., & Boreman, G. 2011. Infrared linear tapered slot antenna. *IEEE Antennas and Wireless Propagation Letters*, **10**, 1299–1301.

[Florence *et al.*, 2012] Florence, L., Kinzel, E., Olmon, R., Ginn, J., Raschke, M., & Boreman, G. 2012. Phase resolved near-field imaging of propagating waves in infrared tapered slot antennas. *Infrared Physics & Technology*, **55**(6), 449–453.

[Florence, 2012] Florence, Louis. 2012. *Infrared taperd slot antennas*. Ph.D. thesis, University of Central Florida.

[Folks *et al.*, 2008] Folks, W. R., Ginn, J., Shelton, D., Tharp, J., & Boreman, G. 2008. Spectroscopic ellipsometry of materials for infrared micro-device fabrication. *Physica Status Solidi C*, **5**(5), 1113–1116.

[Fox, 2010] Fox, M. 2010. *Optical Properties of Solids*. Oxford Master Series in Physics. Oxford University Press.

[Fu, 1998] Fu, Chi. 1998. *Antenna-coupled nanothermopile*. M. Phil. thesis, University of Central Florida.

[Fumeaux *et al.*, 1997] Fumeaux, C., Boreman, G., Herrmann, W., Rothuizen, H., & Kneubühl, F. K. 1997. Polarization response of asymmetric-spiral infrared antennas. *Applied Optics*, **36**(25), 6485–6490.

[Fumeaux *et al.*, 1998] Fumeaux, C., Herrmann, W., Kneubühl, F. K., & Rothuizen, H. 1998. Nanometer thin-film Ni–NiO–Ni diodes for detection and mixing of 30 THz radiation. *Infrared Physics & Technology*, **39**(3), 123–183.

[Fumeaux *et al.*, 1999a] Fumeaux, C., Alda, J., & Boreman, G. D. 1999. Lithographic antennas at visible frequencies. *Optics Letters*, **24**(22), 1629–1631.

[Fumeaux *et al.*, 1999b] Fumeaux, C., Boreman, G., Herrmann, W., Kneubühl, F. Kurt, & Rothuizen, H. 1999. Spatial impulse response of lithographic infrared antennas. *Applied Optics*, **38**(1), 37–46.

[Fumeaux *et al.*, 2000] Fumeaux, C., Gritz, M., Codreanu, I., Schaich, W., González, F. J., & Boreman, G. 2000. Measurement of the resonant lengths of infrared dipole antennas. *Infrared Physics & Technology*, **41**(5), 271–281.

[Gansel *et al.*, 2009] Gansel, J., Thiel, M., Rill, M., Decker, M., Bade, K., Saile, V., von Freymann, G., Linden, S., & Wegener, M. 2009. Gold helix photonic metamaterial as broadband circular polarizer. *Science*, **325**(5947), 1513–1515.

[Ginn, 2009] Ginn, J. 2009. *Phase shaping in the infrared by planar quasi-periodic surfaces comprised of sub-wavelength elements*. Ph.D. thesis, University of Central Florida.

[Ginn *et al.*, 2007a] Ginn, J., Lail, B., Shelton, D., Tharp, J., Folks, W., & Boreman, G. 2007. Characterizing infrared frequency selective surfaces on dispersive media. *Applied Computational Electromagnetics Society Journal*, **22**(1), 184–188.

[Ginn *et al.*, 2008] Ginn, J., Lail, B., Alda, J., & Boreman, G. 2008. Planar infrared binary phase reflectarray. *Optics Letters*, **33**(8), 779–781.

[Ginn *et al.*, 2009] Ginn, J., Shelton, D., Krenz, P., Lail, B., & Boreman, G. 2009. Altering infrared metamaterial performance through metal resonance damping. *Journal of Applied Physics*, **105**(7), 074304.

[Ginn *et al.*, 2010a] Ginn, J., Alda, J., Gómez-Pedrero, J. A., & Boreman, G. 2010. Monochromatic aberrations in resonant optical elements applied to a focusing multilevel reflectarray. *Optics Express*, **18**(11), 10931–10940.

[Ginn *et al.*, 2010b] Ginn, J., Shelton, D., Krenz, P., Lail, B., & Boreman, G. 2010. Polarized infrared emission using frequency selective surfaces. *Optics Express*, **18**(5), 4557–4563.

[Ginn *et al.*, 2007b] Ginn, J. C., Lail, B. A., & Boreman, G. D. 2007. Phase characterization of reflectarray elements at infrared. *IEEE Transactions on Antennas and Propagation*, **55**(11), 2989–2993.

[Gómez-Pedrero *et al.*, 2011] Gómez-Pedrero, J. A., Ginn, J., Alda, J., & Boreman, G. 2011. Modulation transfer function for infrared reflectarrays. *Applied Optics*, **50**(27), 5344–5350.

[González, 2003] González, F. J. 2003. *Infrared focal plane arrays*. Ph.D. thesis, University of Central Florida.

[González & Alda, 2010a] González, F. J., & Alda, J. 2010. Optical antennas as nano-probes in photonic crystals and dielectric waveguide structures. *Page 3 pp of: Proc. EUCAP. 4th European Conference on Antennas and Propagation*.

[González & Alda, 2010b] González, F. J., & Alda, J. 2010. Optical nanoantennas coupled to photonic crystal cavities and waveguides for

near-field sensing. *IEEE Journal of Selected Topics in Quantum Electronics*, **16**(2), 446–449.

[González & Boreman, 2005] González, F. J., & Boreman, G. 2005. Comparison of dipole, bowtie, spiral and log-periodic IR antennas. *Infrared Physics & Technology*, **46**(5), 418–428.

[González *et al*., 2000] González, F. J., Fumeaux, C., Alda, J., & Boreman, G. 2000. Thermal impedance model of electrostatic discharge effects on microbolometers. *Microwave and Optical Technology Letters*, **26**(5), 291–293.

[González *et al*., 2002] González, F. J., Gritz, M., Fumeaux, C., & Boreman, G. 2002. Two dimensional array of antenna-coupled microbolometers. *International Journal of Infrared and Millimeter Waves*, **23**(5), 785–797.

[González *et al*., 2003] González, F. J., Abdel-Rahman, M., & Boreman, G. 2003. Antenna-coupled VO_x thin-film microbolometer array. *Microwave and Optical Technology Letters*, **38**(3), 235–237.

[González *et al*., 2004a] González, F. J., Ashley, C., Clem, P., & Boreman, G. 2004. Antenna-coupled microbolometer arrays with aerogel thermal isolation. *Infrared Physics & Technology*, **45**(1), 47–51.

[González *et al*., 2005] González, F. J., Ilic, B., Alda, J., & Boreman, G. 2005. Antenna-coupled infrared detectors for imaging applications. *IEEE Journal of Selected Topics in Quantum Electronics*, **11**(1), 117–120.

[González *et al*., 2005] González, F. J., Ilic, B., & Boreman, G. D. 2005. Antenna-coupled microbolometers on a silicon-nitride membrane. *Microwave and Optical Technology Letters*, **47**(6), 546–548.

[González *et al*., 2006] González, F. J., Porter, J., & Boreman, G. 2006. Antenna-coupled infrared focal plane array. *Microwave and Optical Technology Letters*, **48**(1), 165–166.

[González & Alda, 2011] González, J., & Alda, J. 2011. Spectral response and far-field pattern of a dipole nano-antenna on metamaterial substrates having near-zero and negative indices of refraction. *Optics Communications*, **284**(5), 1429–1434.

[González *et al*., 2004b] González, J., Alda, J., Ilic, B., & Boreman, G. 2004. Infrared antennas coupled to lithographic Fresnel zone plate lenses. *Applied Optics*, **43**(33), 6067–73.

[González *et al*., 2009] González, J., Alda, J., Simon, Jorge, Ginn, J., & Boreman, G. 2009. The effect of metal dispersion on the resonance of antennas at infrared frequencies. *Infrared Physics & Technology*, **52**(1), 48–51.

[Gottheim *et al*., 2015] Gottheim, S., Zhang, H., Govorov, A., & Halas, N. 2015. Fractal nanoparticle plasmonics: the Cayley tree. *ACS Nano*, **9**(3), 3284–3292.

[Greffet *et al.*, 2010] Greffet, J.-J., Laroche, M., & Marquier, F. 2010. Impedance of a nanoantenna and a single quantum emitter. *Physical Review Letters*, **105**, 117701.

[Gritz *et al.*, 2003a] Gritz, M., Metzler, M., Moser, J., Spencer, D., & Boreman, G. 2003. Fabrication of air bridges using electron beam lithography. *Journal of Vacuum Science & Technology B*, **21**(1), 332–334.

[Gritz *et al.*, 2003b] Gritz, M., González, F. J., & Boreman, G. 2003. Fabrication of infrared antennas using electron-beam lithography. *Pages 100–110 of: Proc. SPIE*, vol. **4984**.

[Gritz *et al.*, 2004] Gritz, M., Metzler, M., Malocha, D., Abdel-Rahman, M., Monacelli, B., Zummo, G., & Boreman, G. 2004. Wavelength tuning of an antenna-coupled infrared microbolometer. *Journal of Vacuum Science & Technology B*, **22**(6), 3133–3136.

[Gritz *et al.*, 2005] Gritz, M., Metzler, M., Abdel-Rahman, M., Monacelli, B., Zummo, G., Malocha, D., & Boreman, G. 2005. Characterization of a wavelength-tunable antenna-coupled infrared microbolometer. *Optical Engineering*, **44**(3), 036402.

[Gritz, 2003] Gritz, Michael. 2003. *Tunable IR antennas*. Ph.D. thesis, University of Central Florida.

[Grossman *et al.*, 1991] Grossman, E., Sauvageau, J., & McDonald, D. 1991. Lithographic spiral antennas at short wavelengths. *Applied Physics Letters*, **59**(25), 3225–3227.

[Grover *et al.*, 2010] Grover, S., Dmitriyeva, O., Estes, M. J., & Moddel, G. 2010. Traveling-wave metal/insulator/metal diodes for improved infrared bandwidth and efficiency of antenna-coupled rectifiers. *IEEE Transactions on Nanotechnology*, **9**(6), 716–722.

[Gureyev & Nugent, 1996] Gureyev, T., & Nugent, K. 1996. Phase retrieval with the transport-of-intensity equation. II. Orthogonal series solution for nonuniform illumination. *Journal of the Optical Society of America A*, **13**(8), 1670–1682.

[Hafner, 1999] Hafner, C. 1999. *Post-modern Electromagnetics*. John Wiley & Sons, Inc.

[Hagerty *et al.*, 2004] Hagerty, J., Helmbrecht, F., McCalpin, W., Zane, R., & Popovic, Z. 2004. Recycling ambient microwave energy with broad-band rectenna arrays. *IEEE Transactions on Microwave Theory and Techniques*, **52**(3), 1014–1024.

[Hallen, 1956] Hallen, E. 1956. Exact treatment of antenna current wave reflection at the end of a tube-shaped cylindrical antenna. *IRE Transactions on Antennas and Propagation*, **4**(3), 479–491.

[Harrington, 1967] Harrington, R. 1967. Matrix methods for field problems. *Proc. of the IEEE*, **55**(2), 136–149.

[Hoefer, 1985] Hoefer, W. 1985. The transmission-line matrix method - Theory and applications. *IEEE Transactions on Microwave Theory and Techniques*, **33**(10), 882–893.

[Huang & Encinar, 2008] Huang, J., & Encinar, J. A. 2008. *Reflectarray Antennas*. John Wiley and Sons.

[Huang *et al*., 2009] Huang, J.-S., Feichtner, T., Biagioni, P., & Hecht, B. 2009. Impedance matching and emission properties of nanoantennas in an optical nanocircuit. *Nano Letters*, **9**(5), 1897–1902.

[Izquierdo-Lorenzo *et al*., 2012] Izquierdo-Lorenzo, I., Alda, I., Sánchez-Cortes, S., & García-Ramos, J. V. 2012. Adsorption and detection of sport doping drugs on metallic plasmonic nanoparticles of different morphology. *Langmuir*, **28**(24), 8891–8901.

[Jackson, 1998] Jackson, J. D. 1998. *Classical Electromagnetism*. 3rd. edn. Wiley.

[Jin, 2014] Jin, J.-M. 2014. *The Finite Element Method in Electromagnetics*. IEEE Press.

[Johns & Beurle, 1971] Johns, P., & Beurle, R. 1971. Numerical solution of 2-dimensional scattering problems using a transmission-line matrix. *Electrical Engineers, Proc. of the Institution of*, **118**(9), 1203–1208.

[Kazemi *et al*., 2005] Kazemi, H., Zimmerman, J., Brown, E., Gossard, A., Boreman, G., Hacker, J., Lail, B., & Middleton, C. 2005. First mmW characterization of ErAs/InAlGaAs/InP semimetal-semiconductor-Schottky diode (S*) detectors for passive millimeter-wave and infrared imaging. *Pages 80–83 of: Proc. SPIE*, vol. **5789**.

[Kazemi *et al*., 2007a] Kazemi, H., Shinohara, K., Nagy, G., Ha, W., Lail, B., Grossman, E., Zummo, G., Folks, W., Alda, J., & Boreman, G. 2007. First THz and IR characterization of nanometer-scaled antenna-coupled InGaAs/InP Schottky-diode detectors for room temperature infrared imaging. *65421J of: Proc. SPIE*, vol. **6542**.

[Kazemi *et al*., 2007b] Kazemi, H., Nagy, G., Tran, L., Grossman, E., Brown, E., Gossard, A., Boreman, G., Lail, B., Young, A., & Zimmerman, J. 2007. Ultra sensitive ErAs/InAlGaAs direct detectors for millimeter wave and THz imaging applications. *Pages 1367–1370 of: 2007 IEEE/MTT-S International Microwave Symposium*.

[Kim *et al*., 2004] Kim, K., Han, Y.-H., Moon, S., Park, J.-H., & Shin, H.-J. 2004. Fabrication and characterization of a three-dimensional feed-horn infrared antenna for an infrared detector. *Applied Optics*, **43**(30), 5594–5599.

[Kinzel *et al*., 2012] Kinzel, E., Ginn, J., Olmon, R., Shelton, D., Lail, B., Brener, I., Sinclair, M., Raschke, M., & Boreman, G. 2012. Phase resolved near-field mode imaging for the design of frequency-selective surfaces. *Optics Express*, **20**(11), 11986–11993.

[Kinzel *et al*., 2013] Kinzel, E., Brown, R., Ginn, J., Lail, B., Slovick, B., & Boreman, G. 2013. Design of an MOM diode-coupled frequency-selective surface. *Microwave and Optical Technology Letters*, **55**(3), 489–493.

[Kinzel *et al*., 2015] Kinzel, E., Ginn, J., Florence, L., Lail, B., & Boreman, G. 2015. Directional thermal emission from a leaky-wave frequency selective surface. *Journal of Nanophotonics*, **9**(1), 093040.

[Knight *et al*., 2011] Knight, M., Sobhani, H., Nordlander, P., & Halas, N. 2011. Photodetection with active optical antennas. *Science*, **332**(6030), 702–704.

[Kosako *et al*., 2010] Kosako, T., Kadoya, Y., & Hofmann, H. F. 2010. Directional control of light by a nano-optical Yagi-Uda antenna. *Nature Photonics*, **4**(5), 312–315.

[Kotter *et al*., 2010] Kotter, D., Novak, S., Slafer, W., & Pinhero, P. 2010. Theory and manufacturing processes of solar nanoantenna electromagnetic collectors. *Journal of Solar Energy Engineering*, **132**, 011014.

[Krenz *et al*., 2008] Krenz, P., Alda, J., & Boreman, G. 2008. Orthogonal infrared dipole antenna. *Infrared Physics & Technology*, **51**(4), 340–343.

[Krenz *et al*., 2010a] Krenz, P., Olmon, R., Lail, B., Raschke, M., & Boreman, G. 2010. Near-field measurement of infrared coplanar strip transmission line attenuation and propagation constants. *Optics Express*, **18**(21), 21678–21686.

[Krenz *et al*., 2011] Krenz, P., Lail, B., & Boreman, G. 2011. Calibration of lead-line response contribution in measured radiation patterns of IR dipole arrays. *IEEE Journal of Selected Topics in Quantum Electronics*, **17**(1), 218–221.

[Krenz *et al*., 2012] Krenz, P., Tiwari, B., Szakmany, G., Orlov, A., González, F. J., Boreman, G., & Porod, W. 2012. Response increase of IR antenna-coupled thermocouple using impedance matching. *IEEE Journal of Quantum Electronics*, **48**(5), 659–664.

[Krenz *et al*., 2010b] Krenz, P. M., Slovick, B., Bean, J., & Boreman, G. 2010. Alignment procedure for radiation pattern measurements of antenna-coupled infrared detectors. *Optical Engineering*, **49**(3), 033607.

[Krenz, 2010] Krenz, Peter. 2010. *Response-calibration techniques for antenna-coupled infrared sensors*. Ph.D. thesis, University of Central Florida.

[Kurs *et al*., 2007] Kurs, A., Karalis, A., Moffatt, R., Joannopoulos, J., Fisher, P., & Soljačić, M. 2007. Wireless power transfer via strongly coupled magnetic resonances. *Science*, **317**(5834), 83–86.

[Lail *et al*., 2009] Lail, B., Middlebrook, C., Krenz, P., & Boreman, G. 2009. Infrared dipole-coupled bolometer response on a hemispherical silicon immersion lens. *Infrared Physics & Technology*, **52**(2–3), 89–96.

[Li *et al.*, 2007] Li, J., Salandrino, A., & Engheta, N. 2007. Shaping light beams in the nanometer scale: A Yagi-Uda nanoantenna in the optical domain. *Physical Review B*, **76**, 245403.

[Lide, 1995] Lide, D. R. 1995. *Handbook of Chemistry and Physics*. 74th edn. CRC Press.

[López-Alonso & Boreman, 2005] López-Alonso, J. M., Alda, J., & Boreman, G. 2005. Alignment characterization in micro and nano technologies. *59870K of: Proc. SPIE.*, vol. **5987**.

[López-Alonso & Alda, 2006] López-Alonso, J. M., & Alda, J. 2006. Characterizing the shape of infrared beams. *SPIE Newsroom*, March.

[López-Alonso *et al.*, 2004] López-Alonso, J. M., Rico-García, J. M., & Alda, J. 2004. Photonic crystal characterization by FDTD and principal component analysis. *Optics Express*, **12**(10), 2176–2186.

[López-Alonso *et al.*, 2005] López-Alonso, J. M., Mandviwala, T., Alda, J., Lail, B., & Boreman, G. 2005. Infrared antenna metrology. *59870L of: Proc. SPIE*, vol. **5987**.

[López-Alonso *et al.*, 2005a] López-Alonso, J. M., Monacelli, B., Alda, J., & Boreman, G. 2005. Infrared laser beam temporal fluctuations: characterization and filtering. *Optical Engineering*, **44**(5), 054203.

[López-Alonso *et al.*, 2005b] López-Alonso, J. M., Monacelli, B., Alda, J., & Boreman, G. 2005. Uncertainty analysis in the measurement of the spatial responsivity of infrared antennas. *Applied Optics*, **44**(21), 4557–4568.

[Lucy, 1974] Lucy, L. B. 1974. An iterative technique for the rectification of observed distributions. *Astronomical Journal*, **79**(6), 745–754.

[Macleod, 2010] Macleod, H. 2010. *Thin-Film Optical Filters*. 4th edn. CRC Press.

[MacSpadden *et al.*, 1996] MacSpadden, J., Little, F., Duke, M., & Ignatiev, A. 1996. An in-space wireless energy transmission Experiment. *Pages 468–473 of: IECED Energy Conversion Engineering Conference*, vol. **1**.

[Maier *et al.*, 2003] Maier, S., Brongersma, M., Kik, P., Meltzer, S., Requicha, A. A. G., Koel, B., & Atwater, H. 2003. Plasmonics—A route to nanoscale optical devices. *Advanced Materials*, **15**(7-8), 562–562.

[Mandel & Wolf, 1995] Mandel, L., & Wolf, E. 1995. *Optical Coherence and Quantum Optics*. Cambridge University Press.

[Mandviwala *et al.*, 2005] Mandviwala, T., Lail, B. A., & Boreman, G. 2005. Infrared-frequency coplanar striplines: design, fabrication and measurements. *Microwave and Optical Technology Letters*, **47**(1), 17–20.

[Mandviwala *et al.*, 2006] Mandviwala, T., Lail, B., & Boreman, G. 2006. Vertical-via interconnection for infrared antennas. *Journal of Vacuum Science & Technology B*, **24**, 2612–2615.

[Mandviwala *et al.*, 2008] Mandviwala, T., Lail, B., & Boreman, G. 2008. Characterization of microstrip transmission lines at IR frequencies—Modeling, fabrication and measurements. *Microwave and Optical Technology Letters*, **50**(5), 1232–1237.

[Mandviwala, 2006] Mandviwala, Tasneem. 2006. *Transmssion lines for IR signal routing*. Ph.D. thesis, University of Central Florida.

[Martin & Piller, 1998] Martin, O. J. F., & Piller, N. 1998. Electromagnetic scattering in polarizable backgrounds. *Physical Review E*, **58**, 3909–3915.

[Martin *et al.*, 1995] Martin, O. J. F., Girard, C., & Dereux, A. 1995. Generalized field propagator for electromagnetic scattering and light confinement. *Physical Review Letters*, **74**, 526–529.

[Mendoza-Yero & Alda, 2007] Mendoza-Yero, O., & Alda, J. 2007. Irradiance map of an apertured Gaussian beam affected by coma. *Optics Communications*, **271**(2), 517–523.

[Middlebrook *et al.*, 2006] Middlebrook, C., Zummo, G., & Boreman, G. 2006. Direct-write electron-beam lithography of an IR antenna-coupled microbolometer onto the surface of a hemispherical lens. *Journal of Vacuum Science & Technology B*, **24**(6), 2566–2569.

[Middlebrook *et al.*, 2008a] Middlebrook, C., Krenz, P., Lail, B., & Boreman, G. 2008. Infrared phased-array antenna. *Microwave and Optical Technology Letters*, **50**(3), 719–723.

[Middlebrook *et al.*, 2008b] Middlebrook, C., Roggemann, M., Boreman, G., Subotic, N., Cooper, K., Buller, W., Yang, W., & Alda, J. 2008. Measurement of the mutual coherence function of an incoherent infrared field with a gold nano-wire dipole antenna array. *International Journal of Infrared and Millimeter Waves*, **29**(2), 179–187.

[Middleton & Boreman, 2006] Middleton, C., & Boreman, G. 2006. Technique for thermal isolation of antenna-coupled infrared microbolometers. *Journal of Vacuum Science & Technology B*, **24**(5), 2356–2359.

[Mittra, 2014] Mittra, R. (ed). 2014. *Computational Electromanetics. Recent Advances and Engineering Applications*. Springer.

[Moddel & Grover, 2013] Moddel, G., & Grover, S. 2013. *Rectenna Solar Cells*. Springer.

[Moddel *et al.*, 2012] Moddel, G., Zhu, Z., Grover, S., & Joshi, S. 2012. Ultrahigh speed graphene diode with reversible polarity. *Solid State Communications*, **152**(19), 1842–1845.

[Momida *et al.*, 2007] Momida, H., Hamada, T., & Ohno, T. 2007. First-principles study of dielectric properties of amorphous high-k materials. *Japanese Journal of Applied Physics*, **46**(5S), 3255–3260.

[Monacelli, 2005] Monacelli, B. 2005. *Spectral signature modification by applicaton of infrared frequency-selective surfaces*. Ph.D. thesis, University of Central Florida.

[Monacelli *et al.*, 2005] Monacelli, B., Pryor, J., Munk, B., Kotter, D., & Boreman, G. 2005. Infrared frequency selective surface based on circuit-analog square loop design. *IEEE Transactions on Antennas and Propagation*, **53**(2), 745–752.

[Moreno *et al.*, 2017] Moreno, C., Alda, J., Kinzel, E., & Boreman, G. 2017. Phase imaging and detection in pseudo-heterodyne scattering scanning near-field optical microscopy measurements. *Applied Optics*, **56**(8), 1037–1045.

[Moreno *et al.*, 2002] Moreno, E., Erni, D., Hafner, C., & Vahldieck, R. 2002. Multiple multipole method with automatic multipole setting applied to the simulation of surface plasmons in metallic nanostructures. *Journal of the Optical Society of America A*, **19**(1), 101–111.

[Muhlschelegel *et al.*, 2005] Muhlschelegel, P., Eisler, H.-J., Martin, O. J. F., Hecht, B., & Pohl, D. W. 2005. Resonant optical antennas. *Science*, **308**(5728), 1607–1609.

[Munk, 2000] Munk, B. 2000. *Frequency Selective Surfaces: Theory and Design*. Wiley-Interscience.

[Neikirk *et al.*, 1982] Neikirk, D., Tong, P., Rutledge, D., Park, H., & Young, P. 1982. Imaging antenna array at 119 μm. *Applied Physics Letters*, **41**(4), 329–331.

[Novotny, 2007] Novotny, L. 2007. Effective wavelength scaling for optical antennas. *Physical Review Letters*, **98**, 266802.

[Novotny & Hecht, 2012] Novotny, L., & Hecht, B. 2012. *Principles of Nano-Optics*. 2nd edn. Cambridge University Press.

[Novotny & van Hulst, 2011] Novotny, L., & van Hulst, N. 2011. Antennas for light. *Nature Photonics*, **5**(2), 83–90.

[Ocelic *et al.*, 2006] Ocelic, N., Huber, A., & Hillenbrand, R. 2006. Pseudoheterodyne detection for background-free near-field spectroscopy. *Applied Physics Letters*, **89**(10), 101124.

[Olmon & Raschke, 2012] Olmon, R., & Raschke, M. 2012. Antenna–load interactions at optical frequencies: impedance matching to quantum systems. *Nanotechnology*, **23**(44), 444001.

[Olmon *et al.*, 2010] Olmon, R., Rang, M., Krenz, P., Lail, B., Saraf, L., Boreman, G., & Raschke, M. 2010. Determination of electric-field, magnetic-field, and electric-current distributions of infrared optical antennas: A near-field optical vector network analyzer. *Physical Review Letters*, **105**, 167403.

[Palik, 1997] Palik, E. D. 1997. *Handbook of Optical Constants of Solids*. Vol. III. Elsevier.

[Puente-Baliarda *et al.*, 1998] Puente-Baliarda, C., Romeu, J., Pous, R., & Cardama, A. 1998. On the behavior of the Sierpinski multiband fractal antenna. *IEEE Transactions on Antennas and Propagation*, **46**(4), 517–524.

[Puscasu *et al.*, 2000a] Puscasu, I., Boreman, G., Tiberio, R., Spencer, D., & Krchnavek, R. 2000. Comparison of infrared frequency selective surfaces fabricated by direct-write electron-beam and bilayer nanoimprint lithographies. *Journal of Vacuum Science & Technology B*, **18**(6), 3578–3581.

[Puscasu *et al.*, 2000b] Puscasu, I., Spencer, D., & Boreman, G. 2000. Refractive-index and element-spacing effects on the spectral behavior of infrared frequency-selective surfaces. *Applied Optics*, **39**(10), 1570–1574.

[Puscasu *et al.*, 2001] Puscasu, I., Schaich, W., & Boreman, G. 2001. Modeling parameters for the spectral behavior of infrared frequency-selective surfaces. *Applied Optics*, **40**(1), 118–124.

[Puscasu *et al.*, 2002] Puscasu, I., Schaich, W., & Boreman, G. 2002. Resonant enhancement of emission and absorption using frequency selective surfaces in the infrared. *Infrared Physics & Technology*, **43**(2), 101–107.

[Puscasu, 2001] Puscasu, Irina. 2001. *Infrared frequency selective surfaces.* Ph.D. thesis, CREOL. University of Central Florida.

[Qu & Kinzel, 2016] Qu, C., & Kinzel, E. 2016. Polycrystalline metasurface perfect absorbers fabricated using microsphere photolithography. *Optics Letters*, **41**(15), 3399–3402.

[Quabis *et al.*, 2001] Quabis, S., Dorn, R., Eberler, M., Glöckl, O., & Leuchs, G. 2001. The focus of light – theoretical calculation and experimental tomographic reconstruction. *Applied Physics B*, **72**(1), 109–113.

[Rajab *et al.*, 2008] Rajab, K., Naftaly, M., Linfield, E., Nino, J., Arenas, D., Tanner, D., Mittra, R., & Lanagan, M. 2008. Broadband dielectric characterization of aluminum oxide (Al_2O_3). *Journal of Microelectronics and Electronic Packaging*, **5**, 101–106.

[Rakos, 2006] Rakos, Balazs. 2006. *Investigation of metal-oxide-metal structures for optical sensor applications.* Ph.D. thesis, University of Notre Dame.

[Ravichandran *et al.*, 2013] Ravichandran, A., Kinzel, E., Ginn, J., D'Archangel, J., Tucker, E., Lail, B., Raschke, M., & Boreman, G. 2013. Numerical modeling of scattering type scanning near-field optical microscopy. *Proc. SPIE*, **8815**, 88150S.

[Richardson, 1972] Richardson, W. 1972. Bayesian-based iterative method of image restoration. *Journal of the Optical Society of America*, **62**(1), 55–59.

[Rico-Garcia *et al.*, 2004] Rico-Garcia, J. M., López-Alonso, J. M., Lail, B., Boreman, G., & Alda, J. 2004. Finite-difference time-domain simulation of low-F# Fresnel zone plates coupled to IR antennas. *Pages 216–226 of: Proc. SPIE.*, vol. **5612**.

[Rico-García *et al.*, 2005] Rico-García, J. M., López-Alonso, J. M., & Alda, J. 2005. Characterization of photonic crystal microcavities with manufacture imperfections. *Optics Express*, **13**(10), 3802–3815.

[Rico-Garcia *et al.*, 2005] Rico-Garcia, J. M., López-Alonso, J. M., & Alda, J. 2005. FDTD analysis of nano-antenna structures with dispersive materials at optical frequencies. *Pages 137–144 of: Proc. SPIE.*, vol. **5838**.

[Rico-Garcia *et al.*, 2008] Rico-Garcia, J. M., Sáanchez-Brea, L. M., & Alda, J. 2008. Application of tomographic techniques to the spatial-response mapping of antenna-coupled detectors in the visible. *Applied Optics*, **47**(6), 768–775.

[Rico-García, 2003] Rico-García, J. M. 2003. *Application of the FDTD method in the optical range for its use in the design and analysis of optical antennas*. M.Phil. thesis, Faculty of Physics. University Complutense of Madrid.

[Rico-García, 2007] Rico-García, J. M. 2007. *Tools for the analysis and design of optical antennas*. Ph.D. thesis, Faculty of Physics. University Complutense of Madrid.

[Rockwell *et al*., 2007] Rockwell, S., Lim, D., Bosco, B., Baker, J., Eliasson, B., Forsyth, K., & Cromar, M. 2007. Characterization and modeling of metal/double-insulator/metal diodes for millimeter wave wireless receiver applications. *Pages 171–174 of: IEEE Radio Frequency Integrated Circuits (RFIC) Symposium*.

[Russer & Russer, 2012] Russer, P., & Russer, J. A. 2012. Application of the transmission line matrix (TLM) method to EMC problems. *Pages 141–144 of: Asia-Pacific Symposium on Electromagnetic Compatibility*.

[Rutledge & Muha, 1982] Rutledge, D., & Muha, M. 1982. Imaging antenna arrays. *IEEE Transactions on Antennas and Propagation*, **30**(4), 535–540.

[Sanchez *et al*., 1978] Sanchez, A., Davis, C., Liu, K., & Javan, A. 1978. The MOM tunneling diode: Theoretical estimate of its performance at microwave and infrared frequencies. *Journal of Applied Physics*, **49**(10), 5270–5277.

[Sarehraz, 2005] Sarehraz, Mohammad. 2005. *Novel rectenna for collection of infrared and visible radiation*. Ph.D. thesis, University of South Florida.

[Schaefer, 1999] Schaefer, Jason. 1999. *Characterization of infrared micro-antennas*. M.Phil. thesis, University of Central Florida.

[Schaich *et al*., 2003] Schaich, W., Schider, G., Krenn, J., Leitner, A., Aussenegg, F., Puscasu, I., Monacelli, B., & Boreman, G. 2003. Optical resonances in periodic surface arrays of metallic patches. *Applied Optics*, **42**(28), 5714–5721.

[Schneider & Webb, 1981] Schneider, M., & Webb, W. 1981. Measurement of submicron laser beam radii. *Applied Optics*, **20**(8), 1382–1388.

[Sharma *et al*., 2015] Sharma, A., Singh, V., Bougher, T., & Cola, B. 2015. A carbon nanotube optical rectenna. *Nature Nanotechnology*, **10**(12), 1027–1032.

[Shelton, 2010] Shelton, D. 2010. *Tunable infrared metamaterials*. Ph.D. thesis, University of Central Florida.

[Shelton *et al*., 2007] Shelton, D., Tharp, J., Zummo, G., Folks, W., & Boreman, G. 2007. Fabrication of periodic microstructures on flexible polyimide membranes. *Journal of Vacuum Science & Technology B*, **25**, 1827–1831.

[Shelton *et al*., 2008a] Shelton, D., Cleary, J., Ginn, J., Wadsworth, S., Peale, R., Kotter, D., & Boreman, G. 2008. Gangbuster frequency selective surface metamaterials in terahertz band. *Electronics Letters*, **44**(22), 1288–1289.

[Shelton *et al.*, 2008b] Shelton, D., Sun, T., Ginn, J., Coffey, K., & Boreman, G. 2008. Relaxation time effects on dynamic conductivity of alloyed metallic thin films in the infrared band. *Journal of Applied Physics*, **104**(10), 103514.

[Shelton *et al.*, 2010a] Shelton, D., Peters, D., Sinclair, M., Brener, I., Warne, L., Basilio, L., Coffey, K., & Boreman, G. 2010. Effect of thin oxide layers on field-enhanced split-ring resonator infrared metamaterials. *Optics Express*, **18**(2), 1085–1090.

[Shelton *et al.*, 2010b] Shelton, D., Coffey, K., & Boreman, G. 2010. Experimental demonstration of tunable phase in a thermochromic infrared-reflectarray metamaterial. *Optics Express*, **18**(2), 1330–1335.

[Shelton *et al.*, 2011] Shelton, D., Brener, I., Ginn, J., Sinclair, M., Peters, D., Coffey, K., & Boreman, G. 2011. Strong coupling between nanoscale metamaterials and phonons. *Nano Letters*, **11**(5), 2104–2108.

[Silva-López *et al.*, 2012] Silva-López, M., Rico-García, J. M., & Alda, J. 2012. Measurement limitations in knife-edge tomographic phase retrieval of focused IR laser beams. *Optics Express*, **20**(21), 23875–23886.

[Silva-López *et al.*, 2013] Silva-López, M., Cuadrado, A., Llombart, N., & Alda, J. 2013. Antenna array connections for efficient performance of distributed microbolometers in the IR. *Optics Express*, **21**(9), 10867–10877.

[Simon & González, 2011] Simon, J, & González, F. J. 2011. Nanoantennas for polarisation division multiplexing. *Electronics Letters*, **47**(2), 120–121.

[Slovick, 2011] Slovick, B. 2011. *Infrared phased-array antenna-coupled diodes*. Ph.D. thesis, University of Central Florida.

[Slovick *et al.*, 2010] Slovick, B., Krenz, P., Zummo, G., & Boreman, G. 2010. Evaporation of uniform anti-reflective coatings on hemispherical lenses to enhance infrared antenna gain. *Infrared Physics & Technology*, **53**(2), 89–93.

[Slovick *et al.*, 2011a] Slovick, B., Bean, J., & Boreman, G. 2011. Angular resolution improvement of infrared phased-array antennas. *IEEE Antennas and Wireless Propagation Letters*, **10**, 119–122.

[Slovick *et al.*, 2011b] Slovick, B., Bean, J., Florence, L., Zummo, G., & Boreman, G. 2011. Infrared antenna measurement of the spatial coherence function. *Optics Express*, **19**(7), 5924–5929.

[Sondheimer, 1952] Sondheimer, E. 1952. The mean free path of electrons in metals. *Advances in Physics*, **1**(1), 1–42.

[Song, 2002] Song, A. 2002. Electron ratchet effect in semiconductor devices and artificial materials with broken centrosymmetry. *Applied Physics A*, **75**(2), 229–235.

[Song *et al.*, 1999] Song, A., Manus, S., Streibl, M., Lorke, A., Kotthaus, J., Wegscheider, W., & Bichler, M. 1999. A nonlinear transport device with no intrinsic threshold. *Superlattices and Microstructures*, **25**(1/2), 269–272.

[Song *et al.*, 2004] Song, A., Maximov, I., Missous, M., & Seifert, W. 2004. Diode-like characteristics of nanometer-scale semiconductor channels

with a broken symmetry. *Physica E: Low-dimensional Systems and Nanostructures*, **21**(2–4), 1116–1120.

[Szakmany *et al*., 2012] Szakmany, G., Krenz, P., Orlov, A., Bernstein, G., & Porod, W. 2012. Antenna-coupled nanowire thermocouples for infrared detection. *Pages 1–4 of: 12th IEEE Conference on Nanotechnology*.

[Szakmany *et al*., 2014a] Szakmany, G., Orlov, A., Bernstein, G., & Porod, W. 2014. Nanoantenna integrated infrared thermoelectric converter. *Pages 571–573 of: 14th IEEE International Conference on Nanotechnology*.

[Szakmany *et al*., 2014b] Szakmany, G., Orlov, A., Bernstein, G., & Porod, W. 2014. Single-metal nanoscale thermocouples. *IEEE Transactions on Nanotechnology*, **13**(6), 1234–1239.

[Szakmany *et al*., 2017] Szakmany, G., Orlov, A., Bernstein, G., & Porod, W. 2017. Nanoantenna arrays for infrared detection with single-metal nanothermocouples. *Infrared Physics & Technology*, **82**(5), 44–49.

[Taflove & Hagness, 2005] Taflove, A., & Hagness, S. 2005. *Computational Electrodynamics: The Finite-Difference Time-Domain Method*. 3rd edn. Artech House.

[Taflove *et al*., 2013] Taflove, A., Johnson, S. G., & Oskooi, A. 2013. *Advances in FDTD Computational Electrodynamics*. Artech House.

[Tamagnone *et al*., 2013] Tamagnone, M., Diaz, J. S. G., Mosig, J., & Perruisseau-Carrier, J. 2013. Hybrid graphene-metal reconfigurable terahertz antenna. *Pages 1–3 of: IEEE MTT-S International Microwave Symposium Digest (MTT)*.

[Taminiau *et al*., 2008] Taminiau, T., Stefani, F., & van Hulst, N. 2008. Enhanced directional excitation and emission of single emitters by a nano-optical Yagi-Uda antenna. *Optics Express*, **16**(14), 10858–10866.

[Tang *et al*., 2008] Tang, L., Kocabas, S., Latif, S., Okyay, A., Ly-Gagnon, D.-S., Saraswat, K., & Miller, D. A. B. 2008. Nanometre-scale germanium photodetector enhanced by a near-infrared dipole antenna. *Nature Photonics*, **2**(4), 226–229.

[Teague, 1983] Teague, M. 1983. Deterministic phase retrieval: a Green's function solution. *Journal of the Optical Society of America*, **73**(11), 1434–1441.

[Tharp *et al*., 2006a] Tharp, J., López-Alonso, J. M., Ginn, J., Lail, B., Munk, B., & Boreman, G. 2006. Demonstration of a single layer meander line phase retarder at IR. *Pages 829–832 of: 2006 IEEE Antennas and Propagation Society International Symposium*.

[Tharp *et al*., 2006b] Tharp, J., López-Alonso, J. M., Ginn, J., Middleton, C., Lail, B., Munk, B., & Boreman, G. 2006. Demonstration of a single-layer meanderline phase retarder at infrared. *Optics Letters*, **31**(18), 2687–2689.

[Tharp *et al.*, 2007a] Tharp, J., Lail, B., Munk, B., & Boreman, G. 2007. Design and demonstration of an infrared meanderline phase retarder. *IEEE Transactions on Antennas and Propagation*, **55**(11), 2983–2988.

[Tharp *et al.*, 2007b] Tharp, J., Alda, J., & Boreman, G. 2007. Off-axis behavior of an infrared meander-line waveplate. *Optics Letters*, **32**(19), 2852–2854.

[Tharp *et al.*, 2008] Tharp, J., Shelton, D., Wadsworth, S., & Boreman, G. 2008. Electron-beam lithography of multiple-layer submicrometer periodic arrays on a barium fluoride substrate. *Journal of Vacuum Science & Technology B*, **26**, 1821–1823.

[Tharp, 2007] Tharp, Jeffrey. 2007. *Design and demonstration of meanderline retarders at infrared frequencies*. Ph.D. thesis, CREOL. University of Central Florida.

[Tucker *et al.*, 2013] Tucker, E., D'Archangel, J., Raschke, M., Briones, E., González, F. J., & Boreman, G. 2013. Near-field mapping of dipole nano-antenna-coupled bolometers. *Journal of Applied Physics*, **114**(3), 033109.

[Tucker *et al.*, 2014] Tucker, E., D'Archangel, J., Raschke, M., & Boreman, G. 2014. Near- and far-field measurements of phase-ramped frequency selective surfaces at infrared wavelengths. *Journal of Applied Physics*, **116**(4).

[Tucker *et al.*, 2015] Tucker, E., D'Archangel, J., Raschke, M., & Boreman, G. 2015. Near-field investigation of the effect of the array edge on the resonance of loop frequency selective surface elements at mid-infrared wavelengths. *Optics Express*, **23**(9), 10974–10985.

[Vandenbosch & Ma, 2012] Vandenbosch, G. A. E., & Ma, Z. 2012. Upper bound for the solar enegy harvesting efficiency of nano-antennas. *Nano Energy*, **1**, 494–502.

[Volakis *et al.*, 1998] Volakis, J., Chatterjee, A., & Kempel, L. 1998. *Finite Element Method for Electromagnetics. Antennas, Microwave Circuit and Scattering Applications*. Wiley-Interscience.

[Volpe *et al.*, 2011] Volpe, G., Volpe, G., & Quidant, R. 2011. Fractal plasmonics: subdiffraction focusing and broadband spectral response by a Sierpinski nanocarpet. *Optics Express*, **19**(4), 3612–3618.

[Wadsworth & Boreman, 2010] Wadsworth, S., & Boreman, G. 2010. Analysis of throughput for multilayer infrared meanderline waveplates. *Optics Express*, **18**(13), 13345–13360.

[Wadsworth & Boreman, 2011a] Wadsworth, S., & Boreman, G. 2011. Broadband infrared meanderline reflective quarter-wave plate. *Optics Express*, **19**(11), 10604–10612.

[Wadsworth & Boreman, 2011b] Wadsworth, S., & Boreman, G. 2011. Comparison of quarter-wave retarders over finite spectral and angular bandwidths for infrared polarimetric-imaging applications. *Applied Optics*, **50**(36), 6682–6688.

[Wadsworth *et al.*, 2011] Wadsworth, S., Clem, P., Branson, E., & Boreman, G. 2011. Broadband circularly-polarized infrared emission from multilayer metamaterials. *Optical Materials Express*, **1**(3), 466–479.

[Wadsworth, 2011] Wadsworth, Sam. 2011. *Generating and detecting circularly polarized thermal infrared radiation*. Ph.D. thesis, University of Central Florida.

[Wiesendanger & Kneubuhl, 1977] Wiesendanger, E., & Kneubühl, F. 1977. Thin-film MOM-diodes for infrared detection. *Applied Physics*, **13**(4), 343–349.

[Wilke *et al.*, 1994] Wilke, I., Herrmann, W., & Kneubühl, F. K. 1994. Integrated nanostrip dipole antennas for coherent 30 THz infrared radiation. *Applied Physics B*, **58**(2), 87–95.

[Xu *et al.*, 2016] Xu, Y., Tucker, E., Boreman, G., Raschke, M., & Lail, B. 2016. Optical nanoantenna input impedance. *ACS Photonics*, **3**, 881–885.

[Yang *et al.*, 2012] Yang, F., Nayeri, P., Elsherbeni, A., Ginn, J., Shelton, D., Boreman, G., & Rahmat-Samii, Y. 2012. Reflectarray design at infrared frequencies: effects and models of material loss. *IEEE Transactions on Antennas and Propagation*, **60**(9), 4202–4209.

[Yang *et al.*, 2015] Yang, H. U., D'Archangel, J., Sundheimer, M., Tucker, E., Boreman, G., & Raschke, M. 2015. Optical dielectric function of silver. *Physical Review B*, **91**, 235137.

[Yang *et al.*, 2008] Yang, W., Roggemann, M., Cooper, K., Buller, W., Subotic, N., Middlebrook, C., & Boreman, G. 2008. The IR antenna pair coupled sensor element and its potential application in wavefront sensing. *Infrared Physics & Technology*, **51**(6), 495–504.

[Yee, 1966] Yee, K. 1966. Numerical solution of initial boundary value problems involving Maxwell's equations in isotropic media. *IEEE Transactions on Antennas and Propagation*, **14**(3), 302–307.

[Young *et al.*, 1973] Young, L., Robinson, L., & Hacking, C. 1973. Meander-line polarizer. *IEEE Transactions on Antennas and Propagation*, **21**(3), 376–378.

[Yu & Capasso, 2014] Yu, N., & Capasso, F. 2014. Flat optics with designer metasurfaces. *Nature Materials*, **13**(2), 139–150.

[Yu *et al.*, 2013] Yu, N., Genevet, P., Aieta, F., Kats, M., Blanchard, R., Aoust, G., Tetienne, J., Gaburro, Z., & Capasso, F. 2013. Flat optics: controlling wavefronts with optical antenna metasurfaces. *IEEE Journal of Selected Topics in Quantum Electronics*, **19**(3), 4700423.

[Zhao *et al.*, 2014] Zhao, Y., Liu, X.-X., & Alù, A. 2014. Recent advances on optical metasurfaces. *Journal of Optics*, **16**(12), 123001.

[Zhu *et al.*, 2013] Zhu, Z., Joshi, S., Grover, S., & Moddel, G. 2013. Graphene geometric diodes for terahertz rectennas. *Journal of Physics D*, **46**(18), 185101.

Index

Javier Alda is Professor of Applied Optics at the Universidad Complutense de Madrid (Spain), where he has served as Dean of the Faculty of Optics and Optometry and as Director of the Optics Department. He received a Licenciado en Ciencias degree from the University of Zaragoza (Spain) in 1985 and obtained a Ph.D. in Physics from the Complutense University of Madrid in 1988. He has been a Visiting Researcher at the University of Central Florida, Stanford University, Universidad Autónoma de San Luis Potosí (Mexico), and the University of North Carolina at Charlotte. He has coauthored more than 120 technical articles primarily devoted to laser beam characterization, matrix optics, signal-processing multivariate techniques, and optical antennas and resonant optics characterization. He is a member of the Spanish Optical Society and OSA, and is a Fellow of SPIE.

Glenn D. Boreman serves as the 2017 President of SPIE and is Chair of the Department of Physics & Optical Science and Director of the Center for Optoelectronics & Optical Communications at the University of North Carolina at Charlotte. He is a co-founder and Chairman of the Board of Plasmonics, Inc. located in Orlando, Florida. From 1984 to 2011 he was on the faculty of the University of Central Florida, where he supervised 25 Ph.D. students to completion. He has held visiting research positions at IT&T (Roanoke, Virginia), U.S. Army Night Vision Lab (Ft. Belvoir, Virginia), McDonnell Douglas Astronautics Co. (Titusville, Florida), Imperial College (London), Universidad Complutense de Madrid (Spain), Swiss Federal Institute of Technology (Zürich), Swedish Defense Research Agency (Linköping), and University of New Mexico (Albuquerque). He received the B.S. in Optics from the University of Rochester and the Ph.D. in Optics from the University of Arizona. Prof. Boreman served as Editor-in-Chief of *Applied Optics* from 2000 to 2005 and as Deputy Editor of *Optics Express*. He is coauthor of the graduate textbook *Infrared Detectors and Systems* and author of *Modulation Transfer Function in Optical and Electro-Optical Systems* (SPIE Press 2001) and *Basic Electro-Optics for Electrical Engineers* (SPIE Press 1998). He has published more than 180 journal articles in the areas of infrared sensors and materials, optics of random media, and image-quality assessment. He is a Fellow of SPIE, OSA, and Military Sensing Symposia (MSS).